

Isolation of Lead-Amino Acid and Mercury-Amino Acid Complexes with
Characterization in the Solid State, the Solution State, and the Gas Phase

by

Cheryl D.L. Saunders

Submitted in partial fulfillment of the requirements
for the degree of Doctor of Philosophy

at

Dalhousie University
Halifax, Nova Scotia
August 2009

DALHOUSIE UNIVERSITY

DATE: August 11, 2009

AUTHOR: Cheryl D.L. Saunders

TITLE: Isolation of Lead-Amino Acid and Mercury-Amino Acid Complexes with
Characterization in the Solid State, the Solution State, and the Gas Phase

DEPARTMENT OR SCHOOL: Department of Chemistry

DEGREE: PhD CONVOCATION: October YEAR: 2009

Permission is herewith granted to Dalhousie University to circulate and to have copied for non-commercial purposes, at its discretion, the above title upon the request of individuals or institutions.

Signature of Author

The author reserves other publication rights, and neither the thesis nor extensive extracts from it may be printed or otherwise reproduced without the author's written permission.

The author attests that permission has been obtained for the use of any copyrighted material appearing in the thesis (other than the brief excerpts requiring only proper acknowledgement in scholarly writing), and that all such use is clearly acknowledged.

For my family and friends

TABLE OF CONTENTS

LIST OF TABLES	xii
LIST OF FIGURES	xii
ABSTRACT.....	xvi
LIST OF ABBREVIATIONS USED	xvii
ACKNOWLEDGEMENTS.....	xx
CHAPTER 1 INTRODUCTION	1
1.1 METALS IN THE ENVIRONMENT.....	1
1.2 METALS IN BIOLOGICAL SYSTEMS	3
1.3 BIOLOGICAL MOLECULES	6
1.4 CHEMISTRY OF MERCURY AND LEAD	10
1.4.1 Relativistic Effects.....	10
1.4.2 Hard-Soft Acid-Base Theory and Donor-Acceptor Strength	13
1.4.3 Donor-Acceptor Complexes	15
1.4.4 Solid State Coordination Geometries of Lead(II).....	16
1.4.5 Solid State Coordination Geometries of Mercury	21
1.4.6 Solution Chemistry of Metal Ions.....	25
1.4.7 Gas Phase Metal-Ligand Complexes.....	29
1.5 CHARACTERIZATION TECHNIQUES	31
1.5.1 X-Ray Crystallography	32
1.5.2 Nuclear Magnetic Resonance Spectroscopy.....	34
1.5.3 Electrospray Ionization Mass Spectrometry	40
1.5.4 Other Characterization Techniques	44

1.6 SUMMARY	45
CHAPTER 2 LEAD-AMINO ACID COMPLEXES	47
2.1 INTRODUCTION.....	47
2.2 RESULTS AND DISCUSSION: SOLID STATE CHARACTERIZATION.....	48
2.2.1 Single Crystal X-Ray Diffraction: Lead-L-Valine	48
2.2.2 Single Crystal X-Ray Diffraction: Lead-L-Isoleucine.....	51
2.2.3 Single Crystal X-Ray Diffraction: Lead-L-Valine-L-Isoleucine.....	54
2.2.4 Single Crystal X-Ray Diffraction: Lead-L-Phenylalanine Complexes	57
2.2.5 Single Crystal X-Ray Diffraction: Lead-L-Arginine.....	61
2.2.6 Lead Coordination Environment: Hemidirected versus Holodirected Geometries	65
2.2.7 Lead-207 Solid State NMR Spectroscopy	67
2.2.8 Carbon-13 Solid State NMR Spectroscopy	69
2.3 RESULTS AND DISCUSSION: SOLUTION STATE CHARACTERIZATION	75
2.3.1 Solution Characterization and Determination of Solution pD.....	76
2.3.2 Lead-207 Solution NMR Spectroscopy.....	76
2.3.3 Carbon-13 Solution NMR Spectroscopy	80
2.3.4 Hydrogen-1 Solution NMR Spectroscopy.....	83
2.3.5 Solution Characterization Ionic Strength Effect.....	84
2.4 RESULTS AND DISCUSSION: GAS PHASE CHARACTERIZATION	85
2.4.1 ESI-MS	85
2.6 CONCLUSIONS	88
CHAPTER 3 MERCURY-ALANINE COMPLEXES.....	89
3.1 INTRODUCTION.....	89

3.2 RESULTS AND DISCUSSION: SOLID STATE CHARACTERIZATION.....	90
3.2.1 Single Crystal X-Ray Diffraction	90
3.2.2 Solid State NMR Spectroscopy	96
3.2.3 IR Spectroscopy and Raman Spectroscopy	97
3.3 RESULTS AND DISCUSSION: SOLUTION STATE CHARACTERIZATION	98
3.3.1 Solution Characterization.....	98
3.3.2 Hydrogen-1 Solution NMR Spectroscopy.....	99
3.3.3 Carbon-13 Solution NMR Spectroscopy	104
3.4 RESULTS AND DISCUSSION: GAS PHASE CHARACTERIZATION	105
3.4.1 ESI-MS	105
3.5 CONCLUSION.....	108
CHAPTER 4 MERCURY-SECONDARY AMINO ACID COMPLEXES.....	109
4.1 INTRODUCTION.....	109
4.2 RESULTS AND DISCUSSION: SOLID STATE CHARACTERIZATION.....	110
4.2.1 Single Crystal X-Ray Diffraction: Mercury-L-Proline.....	110
4.2.2 Single Crystal X-Ray Diffraction: Mercury-N-Methyl-L-Alanine.....	112
4.2.3 Vibrational Spectroscopy.....	114
4.3 RESULTS AND DISCUSSION: SOLUTION STATE CHARACTERIZATION	115
4.3.1 Solution NMR Characterization	115
4.3.2 Hydrogen-1 NMR Spectroscopy	115
4.3.3 Carbon-13 NMR Spectroscopy.....	118
4.4 RESULTS AND DISCUSSION: GAS PHASE CHARACTERIZATION	119
4.4.1 ESI-MS	119
4.5 CONCLUSIONS	120

CHAPTER 5 CONCLUSION	121
5.1 SUMMARY	121
5.1.1 Lead-Amino Acid Complexes	122
5.1.2 Mercury-Amino Acid Complexes	122
5.1.3 Characterization Techniques.....	123
5.2 FUTURE WORK.....	124
5.2.1 Lead-Amino Acid Complexes	124
5.2.2 Mercury-Amino Acid Complexes	125
5.2.3 Metal-Biological Molecule Complexes	126
APPENDIX A EXPERIMENTAL PROCEDURES	127
A.1 SAFETY	127
A.2 GENERAL.....	127
A.3 METAL-AMINO ACID COMPLEX PREPARATION AND ISOLATION	127
A.4 X-RAY CRYSTALLOGRAPHY	136
A.5 VIBRATIONAL SPECTROSCOPY	142
A.6 SOLID STATE NMR SPECTROSCOPY	142
A.6.1 Carbon-13 ssNMR Analyses.....	142
A.6.2 Lead-207 ssNMR Analyses	143
A.7 pH MEASUREMENTS AND PROBE CALIBRATION FOR pD.....	144
A.8 SOLUTION STATE NMR SPECTROSCOPY	145
A.8.1 Room Temperature Solutions	145
A.8.2 Heated Solutions	146
A.8.3 Chemical Shift and pD Study for Lead-Valine, L-Valine, and Lead Nitrate Solutions	146

A.8.4 Lead-207 Chemical Shift and Lead to Amino Acid Ratio Study for Lead-Valine and Lead Nitrate Solutions.....	146
A.8.5 Chemical Shift and Ionic Strength Study for Lead-Valine, L-Valine, and Lead Nitrate Solutions	147
A.9 ELECTROSPRAY IONIZATION MASS SPECTROSCOPY	147
REFERENCE LIST	148

LIST OF TABLES

Table 1.1: Worldwide and Domestic (US) Metal Resources.....	2
Table 1.2: Relative mammalian toxicity of elemental lead and mercury	4
Table 1.3: Ionization energies of four metals.	13
Table 1.4: Known coordination numbers and van der Waals radii for mercury and lead	15
Table 1.5: Bond lengths and bond angles of known mercury(I)-carboxylate complexes	22
Table 1.6: Bond lengths and bond angles of the three methylmercury-amino acid complexes found in Figure 1.14.	25
Table 1.7: Mercury-amino acid and lead-amino acid complexes detected in the gas phase	30
Table 1.8: Properties of mercury and lead.	32
Table 1.9: Properties of five spin ½ nuclei of interest.....	35
Table 2.1: Solid state lead-207 NMR data for the five lead-amino acid complexes	67
Table 2.2: Lead-207 chemical shifts of lead nitrate and lead-amino reaction mixtures or dissolved crystals.	78
Table 2.3: Amino acid methine and carboxyl carbon-13 chemical shifts of amino acid solutions and lead-amino acid solutions.....	82
Table 2.4: ESI-MS peak assignments of the dissolved crystals and reaction mixtures of lead-amino acid solutions	86
Table 3.1: Interatomic distance ranges in $[\text{Hg}_{12}(\text{Ala})_8(\text{NO}_3)_8] \cdot 2\text{H}_2\text{O}$	92
Table 3.2: Solid state carbon-13 NMR chemical shifts (ppm) for crystals of Hg-LAla, Hg-DAla, and L-alanine. ⁴⁴	96
Table 3.3: Carboxyl and methine carbon-13 NMR signals of LAla, $\text{Hg}^{\text{I}}+\text{LAla}$, $\text{Hg}^{\text{I}}-\text{LAla}$, $\text{Hg}^{\text{I}}-\text{DAla}$, and $\text{Hg}^{\text{II}}+\text{LAla}$	104
Table 3.4: ESI-MS data for the reaction mixtures and dissolved crystals of Hg-Ala.....	107
Table 4.1: Interatomic distances and ranges in Hg-Pro, Hg-NAla, Hg-Ala.	114

Table 4.2: Carboxyl and Methine carbon-13 chemical shifts of mercury(I) with secondary amino acid solutions	118
Table 4.3: ESI-MS data for the reaction mixtures of Hg + Pro, Hg + NAla, Hg-Pro, and Hg-NAla.	119
Table A.1: Infrared and Raman frequencies and peak assignments for Hg-LAla, Hg-DAla, and MeHg(LAla).....	132
Table A.2: Crystallographic data for lead-amino acid complexes discussed in Chapter 2	138
Table A.3: Crystallographic data for mercury-alanine complexes discussed in Chapter 3	140
Table A.4: Crystallographic data for mercury-secondary amino acid complexes discussed in Chapter 4.....	141

LIST OF FIGURES

Figure 1.1 Dose-response curves for essential and trace metals.....	3
Figure 1.2: The amino acid L-alanine (where R=CH ₃) a) Fischer projection, and b) perspective diagram.....	6
Figure 1.3: The twenty most common amino acids found in biological systems.....	8
Figure 1.4: pH equilibria of an amino acid.....	9
Figure 1.5: Qualitative diagram of heavy element atomic orbitals when relativistic effects are taken into account.....	11
Figure 1.6: Latimer diagram for mercury in acidic solutions.....	12
Figure 1.7: Idealized frontier orbital diagram of a) a hard acid-hard base interaction, and b) a soft acid-soft base interaction.....	14
Figure 1.8: Coordination spheres of a metal cation in the solid state.....	16
Figure 1.9: Holodirected and hemidirected coordination of lead(II).....	17
Figure 1.10: Bonding interaction diagrams ranging from the hemidirected geometry and holodirected geometry extremes.....	18
Figure 1.11: Diagrams showing the coordination geometry of a) Pb(AspH)(NO ₃), b) Pb(Val) ₂ (H ₂ O) ₂ (NO ₃) ₂ , c) [Pb(Phe) ₂] _n , d) [Pb(Pro) ₂ (H ₂ O)] _n , e) Pb(DPen), f) Pb(DNTyr)(H ₂ O) _{0.5}	20
Figure 1.12: Mercury(I)-oxygen interactions in complexes containing mercury(I) and a carboxylate group.....	21
Figure 1.13: Diagram of diamminemercury(II) dication.....	23
Figure 1.14: Diagram of methylmercury-amino acid coordination in a) [HgCH ₃ (DLPen)]•H ₂ O, b) [(CH ₃ Hg) ₂ (DLPen)], and c) CH ₃ Hg(DLAla).....	24
Figure 1.15: Idealized diagram of polar solvent coordination spheres about a metal cation	26
Figure 1.16: Formation equilibria of a) mercury oxide and b) lead oxide. ⁶⁵	27
Figure 1.17: Protonation and metallation equilibria for amino acids.....	28
Figure 1.18: Diagram of glutathione.....	29

Figure 1.19: Exchange equilibrium between mercury(I) and mercury(II).	39
Figure 1.20: Schematic of the mass spectrometric process.	40
Figure 1.21: Electrospray ionization (ESI) source of the Finnigan LCQDUO ion trap	41
Figure 1.22: Diagram of the ion trap mass analyser.	43
Figure 2.1: Amino acids of interest in Chapter 2.....	47
Figure 2.2: Perspective view of the asymmetric unit of Pb-Val	49
Figure 2.3: Illustration of crystal packing of Pb-Val	50
Figure 2.4: Perspective view of the asymmetric unit of Pb-Ile.....	52
Figure 2.5: Illustration of crystal packing of Pb-Ile.....	53
Figure 2.6: Perspective view of the asymmetric unit of Pb-Val-Ile	55
Figure 2.7: Illustration of crystal packing of Pb-Val-Ile, showing the vertical R-group planes..	56
Figure 2.8: Perspective views of the asymmetric units of the lead-L-phenylalanine hydrates a) Pb-Phe.2H ₂ O and b) Pb-Phe.3H ₂ O	58
Figure 2.9: Illustration of crystal packing of a) Pb-Phe.2H ₂ O, and b) Pb-Phe.3H ₂ O, showing the vertical R-group planes.	60
Figure 2.10: Perspective view of the asymmetric unit of Pb-HArg.....	63
Figure 2.11: Illustration of crystal packing of Pb-HArg, showing the vertical R-group planes.	64
Figure 2.12: Coordination spheres about the lead centre in the six presented lead-amino acid crystal structures.	66
Figure 2.13: Lead-207 solid state NMR spectra of ground crystals of a) Pb-Val, b) Pb-Val- Ile, and c) Pb-Ile crystals	68
Figure 2.14: Carbon-13 ssNMR spectra of Val, Pb-Val, Pb-Val-Ile, Pb-Ile and Ile	70
Figure 2.15: Carbon-13 ssNMR spectra of Pb-Phe.2H ₂ O, Pb-Phe.3H ₂ O and Phe.....	71
Figure 2.16: Carbon-13 ssNMR spectra of Pb-HArg and Arg.	72
Figure 2.17: Water molecule environments within the crystal structures of a) Pb-Phe.2H ₂ O and the b) Pb-Phe.3H ₂ O	74

Figure 2.18: Competition equilibria between protons and lead for Lewis donating atoms on an amino acid.....	75
Figure 2.19: Change in lead-207 chemical shift with increasing pD values (and increasing solution ionic strength) Pb + Val and Pb(NO ₃) ₂ solutions.	77
Figure 2.20: Change in lead-207 chemical shift with decreasing lead to valine ratios to the valine saturation point.....	79
Figure 2.21: Carbon-13 chemical shifts of the carboxyl carbon and the methine carbon of L-valine and Pb + Val.....	81
Figure 2.22: Hydrogen-1 chemical shifts of the methine proton of L-valine and Pb + Val solutions at varying pD values.....	83
Figure 2.23: Effect of ionic strength on carbon-13 chemical shifts of the carboxyl and methine carbons of Val in five lead with Val solutions	84
Figure 3.1: Amino acids of interest in Chapter 3.....	89
Figure 3.2: Asymmetric unit of Hg-LAla.	93
Figure 3.3: Hydrogen bonding of one water molecule between two Hg-Ala asymmetric units... ..	94
Figure 3.4: Extended views of the Hg-LAla asymmetric unit.....	95
Figure 3.5: Carbon-13 ssNMR signals for a) Hg-LAla, b) Hg-DAla, and c) L-alanine crystals.	97
Figure 3.6: Competition equilibria between protons, mercury(I) and mercury(II) for alanine.....	99
Figure 3.7: Hydrogen-1 NMR of a) Hg-LAla b) Hg-DAla) and c) D-alanine	100
Figure 3.8: Solution state hydrogen-1 NMR spectra of the Hg ^I +DALa reaction mixtures at various concentrations. Inset: Comparison of methine signal for the reaction mixture and dissolved crystals.....	101
Figure 3.9: Hydrogen-1 chemical shift for the methine hydrogen atom for deuterium oxide solutions of a) Hg ^{II} + LAla, b) Hg ^I +LAla, c) LAla, and d) Hg ^I +NALa.....	103
Figure 3.10: a) Positive ion ESI mass spectrum of a Hg ^I +LAla. b) Tandem mass spectrum of <i>m/z</i> 308.....	106
Figure 4.1: Amino acids of interest in Chapter 4.....	109
Figure 4.2: Perspective view of the contents of the asymmetric unit of Hg-Pro.....	111

Figure 4.3: Extended structure of Hg-Pro.....	112
Figure 4.4: Perspective view of the asymmetric unit of Hg-NAla	113
Figure 4.5: Extended structure of Hg-NAla.....	113
Figure 4.6: Hydrogen-1 chemical shifts of Pro, Hg ^I + Pro and Hg-Pro	116
Figure 4.7: Hydrogen-1 signals of NAla, Hg ^I + NAla and Hg ^I -NAla	117

ABSTRACT

Although some physiological effects of toxic metal poisoning have been known for centuries, the specific chemical interactions between biological molecules and mercury(I), mercury(II) or lead(II) are not well understood. To date, only thirteen crystal structures of inorganic mercury-amino acid complexes and six crystal structures of lead-amino acid complexes have been reported with varying degrees of characterization. In order to improve our understanding of the coordination chemistry of mercury and lead in biological environments, a systematic method for the isolation of inorganic metal-amino acid complexes from acidic aqueous solutions has been developed. With this method we have prepared five new lead-amino acid complexes (with L-valine, L-isoleucine, L-phenylalanine, and L-arginine) and four new mercury-amino acid complexes (with L-alanine, D-alanine, L-proline, and *N*-methyl-L-alanine). These metal-amino acid complexes have been comprehensively characterized in the solid state, solution state and gas phase. The development of this isolation technique in conjunction with the exploration of a number of characterization techniques for studying metal-amino acid interactions greatly enhances the known methods by which metal-biological molecule systems are studied.

LIST OF ABBREVIATIONS USED

AC	Alternating current	DSS	2,2-Dimethyl-2-silapentane-5-sulfonic acid (3-Trimethylsilylpropane-1-sulfonic acid) or sodium salt
AC _{aux}	Auxilliary alternating current		
Ala	L-Alanine		
Arg	L-Arginine	e	Elementary charge (relativistic effects)
Asn	L-Asparagine	e ⁻	Electron (ESI-MS)
Asp	L-Aspartic acid	EA	Elemental analysis
AspH	Protonated L-aspartate	ESI	Electrospray Ionization
B0	External magnetic field	F _{calc}	Calculated structure factor (X-ray crystallography)
B1	Applied magnetic field	F _{obs}	Observed structure factor (X-ray crystallography)
b.p.	Boiling point	FT	Fourier Transform
c	Concentration (ionic strength)	FW	Formula weight
c	Speed of light (relativistic effects)	GI	Gastrointestinal
cf.	Compared to	Gln	L-Glutamine
CNS	Central nervous system	Glu	L-Glutamic acid
CP	Cross polarization	Gly	L-Glycine
Cys	L-Cysteine	GOF	Goodness of fit
DAla	D-alanine	h	Plank's constant
DC	Direct current	HA-HB	Hard acid-hard base orbital interaction
DLAla	DL-alanine	HArg	Cationic L-arginine
DLAla	Racemic mixture of LAla and DAla	HCys	L-Homocysteine
DLPen	DL-penicillamine	Hg + NAla	Mercury(I) nitrate with NAla reaction mixture
DNA	Deoxyribonucleic acid	Hg + Pro	Mercury(I) nitrate with Pro reaction mixture
DNTyr	3,5-dinitrotyrosine	Hg-Ala	Both Hg-LAla and Hg-DAla crystals
DPen	D-penicillamine		

Hg-DAla	[Hg ₁₂ (DAla) ₈ (NO ₃) ₈] •2H ₂ O	m.p.	Melting point
Hg ^I	Mercury(I)	MS	mass spectrometry
Hg ^{II}	Mercury(II)	MS/MS	Tandem mass spectrometry
Hg-LAla	[Hg ₁₂ (LAla) ₈ (NO ₃) ₈] •2H ₂ O	M ^{x+}	Metal cation
Hg-NAla	[Hg ₂ (NAla) ₂ (NO ₃) ₂] •2H ₂ O	NAla	N-methyl-L-alanine
Hg-Pro	[Hg ₂ (Pro) ₂ (NO ₃) ₂]	NMR	Nuclear magnetic resonance
His	L-Histidine	Pb-HArg	[Pb ₂ (OH ₂)(HArg) ₃ (NO ₃) ₇] •3H ₂ O
HOMO	Highest occupied molecular orbital	Pb ^{II}	Lead(II)
I	Reflection intensity (X-ray crystallography)	Pb-Ile	[Pb(OH ₂)(Ile) ₂][NO ₃] ₂ •H ₂ O
I	Nuclear spin quantum number	Pb-Phe.2H ₂ O	[Pb(OH ₂) ₂ (Phe) ₂ (NO ₃)][NO ₃]
I.S.	Isotropic shift (ppm)	Pb-Phe.3H ₂ O	[Pb(OH ₂)(Phe) ₂][NO ₃] ₂ •2H ₂ O
IE	Ionization energy	Pb-Val	[Pb(OH ₂) ₂ (Val) ₂ (NO ₃)][NO ₃]
Ile	L-Isoleucine	Pb-Val-Ile	[Pb(OH ₂) ₂ (Val)(Ile)(NO ₃)][NO ₃]
ip	Intraperitoneal		
IR	Infrared		
iv	Intravenous	Phe	L-Phenylalanine
LAla	L-Alanine	Pro	L-Proline
LD ₅₀	Dose at which 50% of the exposed population die	R ₁	R-factor
Leu	L-Leucine	RF	Radio frequency
LUMO	Lowest unoccupied molecular orbital	R _{int}	The residual for symmetry-equivalent reflections used to calculate the average intensity
Lys	L-Lysine		
m	Mass of electrons (relativistic effects)	RNA	Ribonucleic acid
<i>m/z</i>	Mass to charge ratio	S	Mercury satellite peaks
MAS	Magic angle spinning	SA-SB	Soft acid-soft base orbital interaction
Met	L-Methionine	Ser	L-Serine
m ₀	Mass of electron at rest		

s.g.	Specific gravity	${}^xJ_{AB}$	X number of bond(s) coupling between nucleus A and nucleus B (Hz)
SOF	Site occupancy factor		
solnNMR	Solution state NMR	Z	Ion charge (ionic strength)
SPE	Single Pulse Excitation	Z	Atomic number (relativistic effects)
ssNMR	Solid state NMR		
		γ	Magnetogyric ratio (or gyromagnetic ratio)
TD ₅₀	Dose at which 50% of the exposed population suffer toxic effects	δ	Chemical shift (ppm)
		δ_{DSS}	Chemical shift with DSS as an internal standard
Thr	L-Threonine		
TMS	Tetramethylsilane	$\Delta\delta$	Change in chemical shift with no internal standard
TPPM	Two Pulse Phase Modulation	$\Delta\delta_{DSS}$	Change in chemical shift with DSS as an internal standard
Trp	L-Tryptophan		
Tyr	L-Tyrosine	θ	Incident angle (X-ray crystallography)
v	Velocity (relativistic effects)	μ	Absorption coefficient (X- ray crystallography)
Val	L-Valine		
vdW	van der Waals	ρ_{calcd}	Calculated density (X-ray crystallography)
wR ₂	Weighted R-factor		
XAS	X-ray absorption spectroscopy	ΣvdW	Sum of the van der Waals radii

ACKNOWLEDGEMENTS

I would like to thank my friends and family for supporting me as I complete this Ph.D. in Bioinorganic Chemistry; past and present Burford Research Group members and Stradiotto Research Group members; especially Dr. Neil Burford for giving me the opportunity to learn about both bioinorganic and fundamental chemistry under his supervision; my Ph.D. committee members Dr. Alan Doucette, Dr. Laura Turculet, Dr. Kevin Grundy, and Dr. Jim Pincock; my Ph.D. defence external examiner Dr. Scott Bohle; the faculty and staff of the Department of Chemistry at Dalhousie University, especially Xiao Feng and the Maritime Mass Spectrometry Laboratories, and Dr. Ulli Werner-Zwanziger, Dr. Banghou (Howard) Chen and Dr. Mike Lumsden and the ARMRC; Dr. Bob McDonald and Dr. Mike Ferguson at the X-Ray Crystallography Laboratory at the University of Alberta and, the organizations that fund our research: Natural Sciences and Engineering Research Council of Canada, Killam Program of the Canada Council for the Arts, Canada Research Chairs program, Canada Foundation for Innovation, Canada Research Chairs, and Nova Scotia Research and Innovation Trust Fund.

CHAPTER 1 INTRODUCTION

Bioinorganic chemistry or inorganic biochemistry is the study of metals in biological systems. This can include the fundamental chemistry of metal-biomolecule interactions, the roles or effects of the metals in biochemical pathways, or, more generally, the effects of elevated or decreased amounts of metals on populations.

Toxic, trace metals can have very damaging effects on biological processes. By studying the chemistry of and the role of trace metals in these processes, information will be elucidated on the biochemical consequences of metal introduction to biosystems. Understanding the fundamental metal-biomolecule interactions and metal biochemistry will allow for the development of better treatments for metal poisoning.

The general, focus of this work was the study of the fundamental bioinorganic coordination chemistry of lead(II), mercury(I) and mercury(II) and the interactions of these metals with amino acids (simple biological molecules). Currently, there are relatively few lead-amino acid and mercury-amino acid solid state structures that have been reported in the literature. The characterization of these complexes is often specific to an isolated crystal and may or may not be relevant to the solution behaviour of the compound. In this project, five new lead(II)-amino acid complexes have been isolated and characterized in the solid state, the solution state and the gas phase. An analogous study of one mercury(I)mercury(II)-amino acid complex and two mercury(I)-amino acid complexes is also described. The results of these studies increase the known information about metal-biological molecule interactions and gives a comprehensive chemical assessment for each metal-amino acid system.

1.1 METALS IN THE ENVIRONMENT

Metals can be found in the earth's crust, the atmosphere, and the hydrosphere. In geological terms, trace metals constitute less than one percent of the earth's crust.¹ Although trace metals, such as mercury and lead, are ubiquitous in the environment, the environmental presence of these metals is mainly due to metal introduction through

anthropogenic sources, such as fossil fuel combustion, agricultural uses, metallurgical industries, electronics, batteries, pigments and paints, mining, medicinal uses and waste disposal, Table 1.1.¹⁻⁴ As the human population increases, the concurrent need for energy and natural resources increases. This means that, in the future, the prevalence of toxic, trace metals in the environment will continue to grow. Unlike organic molecules, which degrade in the environment, trace metals will persist and accumulate in plants and animals.⁵ The bioavailability of these metals, especially in terms of aquatic organisms, results from the physical and chemical properties of each metal (such as, oxidation state, radius, concentration, degree of hydration, coordination with oxygen, pH and system redox status), and the availability and nature of the complexing ligands (including solubility and pH-dependent charge).⁴

Table 1.1: Worldwide and Domestic (US) Metal Resources. (Adapted from reference 4)

Metal	Properties ^a	Major Uses	Ore, aspects of resources ^b
Lead	m.p. 327 °C b.p. 1750 °C s.g. 11.35 Silvery color	5 th most widely used metal Storage batteries Decreasing for environmental reasons: Gasoline, pigments, and ammunition	Ore: galena (PbS) Worldwide consumption about 3.5 million metric tons, 1/3 in U.S. Global reserves about 140 million metric tons, 39 metric tons U.S.
Mercury	m.p. -38 °C b.p. 357 °C s.g. 13.6 Shiny, liquid metal	Electronic apparatuses, electrodes, chemicals	Ore: cinnabar (HgS) Annual world production 11,500 metric tons, 1/3 used in U.S. World resources 275,000 metric tons, 6,600 U.S.

^a Abbreviations: m.p. = melting point; b.p. = boiling point; s.g. = specific gravity

^b All figures are approximate; quantities of minerals are subject to fluctuation

1.2 METALS IN BIOLOGICAL SYSTEMS

Within biological organisms, essential, trace metals are required for optimal functioning of biochemical processes, while toxic, trace metals disrupt these processes leading to physiological abnormalities or even organism death.

In the 16th century, Theophrastus Bombastus von Hohenheim (a.k.a. Paracelsus) the “father of toxicology” stated the basic tenet of toxicology “All things are poisons and nothing is without poison, only the dose makes a thing a poison” (translated from the original German).⁶ This means that while some elements may be deemed essential, all elements have the potential to be toxic depending on the concentration of the elements that are present within the body. This concept is illustrated in Figure 1.1. In order for organisms to function properly, optimum concentrations of essential metals are required, below this concentration results in deficiencies and above this concentration results in toxicity. There is a fine balance between aiding and destroying the normal function of a biochemical process; because of this, essential metal uptake and removal is often tightly regulated in most organisms. Trace metals that are not required for organism survival can be present within an organism without ill effects until a critical concentration is reached at which point toxicity occurs, as seen in the toxic metal dose-response curve in Figure 1.1.

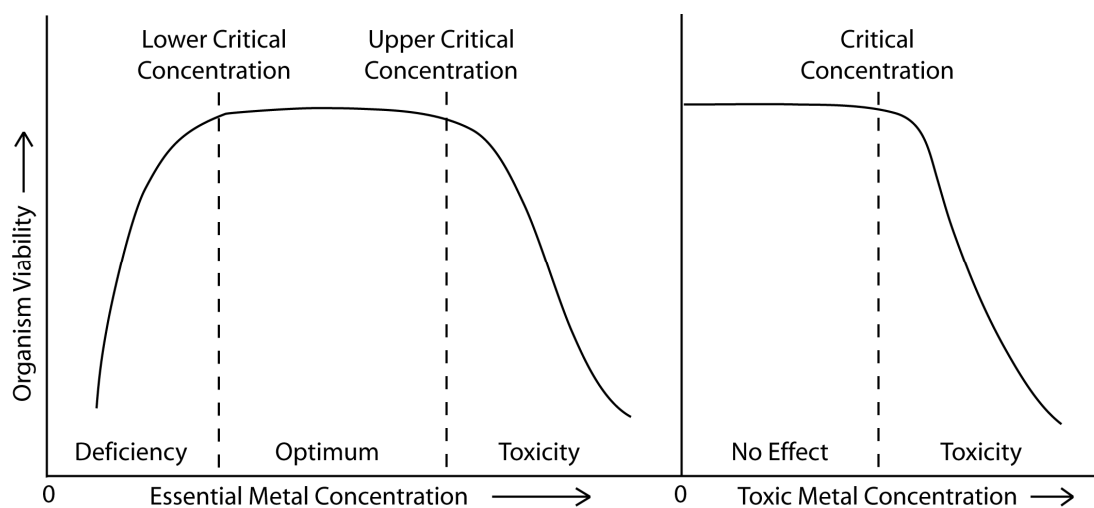


Figure 1.1: Dose-response curves for essential and toxic trace metals. (Adapted from reference 4)

The amount of a trace metal that causes toxic effects is dependent on physical and chemical properties of that metal and the accessibility of the metal for biological ligands and processes. In health related terms, there are a few measurements that are used to describe the amount of trace metal that will cause no effect, toxic effects or death. These include maximum allowable daily intake for humans, toxic dose for humans, lethal dose for humans, TD₅₀ (toxic dose where 50% of the tested animal population feels toxic effects) and LD₅₀ (lethal dose where 50% of the tested animal population dies).^{7,8} These values are dependent on the species of metal, the organism in question and the route of exposure. Some examples of elemental mercury and lead LD₅₀ and human daily dose values are shown in Table 1.2. TD₅₀ and LD₅₀ are usually tested on mice or rats. Therefore, these values do not necessarily reflect the doses that would affect humans.⁸ The route of exposure is also an important factor when consider when evaluating health risk indices and values. The amount of trace metal that enters the blood stream by an oral dose (absorbed by the intestines and gastrointestinal (GI) tract) will be much smaller than by inhalation (absorbed through the lungs), by an intraperitoneal (ip) dose (injected into the gut cavity), or by an intravenous (iv) dose (injected into the veins).

Table 1.2: Relative mammalian toxicity of elemental lead and mercury in injected doses and diets. (Adapted from reference 4)

Metal	LD ₅₀ (<i>ip</i>)* in mammals (mg/kg bodyweight)	Dose in human diet (mg/day)	
		Toxic	Lethal
Lead	70	1	10 000
Mercury	1.5	0.4	150–300

* Injected into the peritoneum to avoid absorption through the digestive tract. Chemical form of the element will affect its toxicity.

The toxicology of mercury is enhanced and modulated by the various forms that mercury can take in the body.⁸ Inorganic mercury can be ingested or inhaled. In this form it cannot easily cross the blood brain barrier but will interact with thiol groups on proteins inducing autoimmune diseases and other adverse effects. Inorganic mercury is also thought to

interact with DNA and RNA affecting normal protein synthesis. While in the body, inorganic mercury can be reduced or methylated thus increasing the lipophilicity of the metal allowing it to cross the blood-brain barrier or accumulate in other lipid rich tissues.^{9;10} Due to the ease with which mercury(I) disproportionates in the presence of stronger Lewis donors, mercury(I) is not expected to be in the monovalent form in biological systems.²

Due to its charge and ionic radius, lead(II) is known to replace the essential dications calcium(II) and zinc(II) in biological processes.¹¹⁻¹⁴ For example, lead(II) can mimic calcium(II) and access the central nervous system (CNS) through the calcium dependent channels. While in the CNS, it can replace essential calcium cations in protein kinase C isozymes. Calcium(II) can also be replaced by lead(II) in bones, forming $\text{Pb}_3(\text{PO}_4)_2$. The most commonly known effect of lead intoxication is the development of sideroblastic anemia (loss of normal red blood cell function which causes decreased oxygen delivery to tissues). This anemia is a result of the decrease in haem synthesis by the inhibition of a zinc(II) dependent enzyme δ -aminolaevulinic acid dehydratase. Lead is also known to compete with zinc for the zinc binding site of zinc fingers, altering the shape of the protein and destroying its ability to bind DNA.¹¹⁻¹³

The current treatment for metal exposure and poisoning consists of the removal of the metal from an individual's environment, followed by chelation therapy—in which molecules that bind to metals are administered in the expectation that the toxic metals will be removed from the body. At present, these therapeutic chelators are not specific for toxic metals, binding both essential and toxic metals, and will redistribute toxic metals throughout the body.¹⁵

In order to improve the effectiveness of chelation therapy, new metal chelators must be designed and synthesized. But before this is possible, the fundamental biological coordination chemistry of each metal must be understood and a clearer comprehension of the toxic roles that lead or mercury play in the human body must be attained.

1.3 BIOLOGICAL MOLECULES

In general, biological structures and large biomolecules are composed of four types of biological molecule subunits, namely: amino acids, carbohydrates, lipids and nucleotides. Large structures may be composed of either a single type or a combination of these subunits, where more complexity may be added by functionalizing or altering the subunits (e.g., phosphorylation with inorganic phosphate, or deoxygenation of carbohydrates).¹⁶

As mentioned in the previous section, addition of toxic metals to complex biological systems results in a disruption of many biological processes, where the majority of these processes result from protein and enzyme (catalytically active protein) action. Our interest is in studying the interactions and coordination chemistry of trace metals and the amino acid and peptide units that make up larger protein biomolecules.

All protein forming chiral amino acids found in higher organisms are in the L enantiomeric form. The D/L nomenclature is based upon the position of the amine on the chiral carbon stereocentre to which it is attached. In a Fischer projection of an L-amino acid (with the carboxylate in the top position and the R group in the bottom position) the amine is on the left side of the carbon. In a D-amino acid the amine resides on the right side of the carbon. The Fischer projection of α -L-alanine in Figure 1.2a shows this “L” positioning of the amine. The amino acid diagrams in Figure 1.2 have two additional features: the α and β carbon centres are labelled and they are in the zwitterionic form.

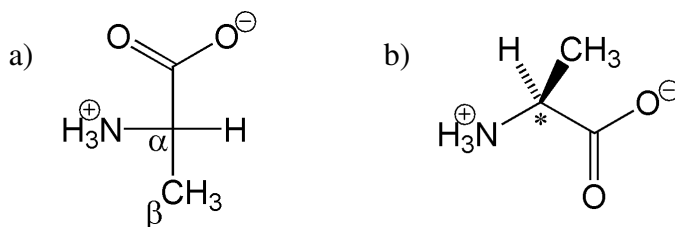


Figure 1.2: The amino acid L-alanine (where R=CH₃) a) Fischer projection, and b) perspective diagram. α and β indicate the alpha and beta carbon atoms from the carboxylate group, respectively, and the asterisk (*) indicates the chiral carbon.

The twenty most common amino acids found in proteins (Figure 1.3) are α -amino acids, named for the attachment of the amine group on the alpha carbon centre. There is only one β -amino acid found in biological systems: β -alanine, but it is not found in proteins.¹⁶

The order of the groups that make up the “amino acid backbone” is *primary amine–chiral α -carbon–carboxylic acid*. These groups are usually drawn from left to right, respectively (Figure 1.2b). There are two exceptions to this description: 1) the side chain (usually denoted “R”) of the simplest amino acid, glycine, is a hydrogen atom, which removes the chirality of the α -carbon; and, 2) the three carbon chain of the cyclic amino acid proline starts from the α -carbon centre and terminates with a covalent bond to the nitrogen atom, resulting in a secondary amine.

Side chains (or R-groups) of amino acids have a variety of chemical characteristics that influence the interactions between amino acid residues within a protein and between amino acid residues and other molecules in the protein environment.¹⁶ The chemical interactions within the protein direct the structural form of the protein. For example, if two cysteine residues are in close proximity, then the thiol groups can be oxidized to form a disulfide bond. This sulfur-sulfur bond is critically important in maintaining the structural conformation of the protein or protein subunit (tertiary structure) and the connection between protein subunits (quaternary structure). Side chains of amino acids vary with respect to hydrophobicity, hydrophilicity, polarity, and acidity or basicity; there are R-groups with alcohol, aromatic, alkyl or even thioether functional groups (as seen in Figure 1.3). This large variety of coordination and bonding possibilities make amino acids invaluable in biochemical pathways, where intermolecular interactions are of vital importance.

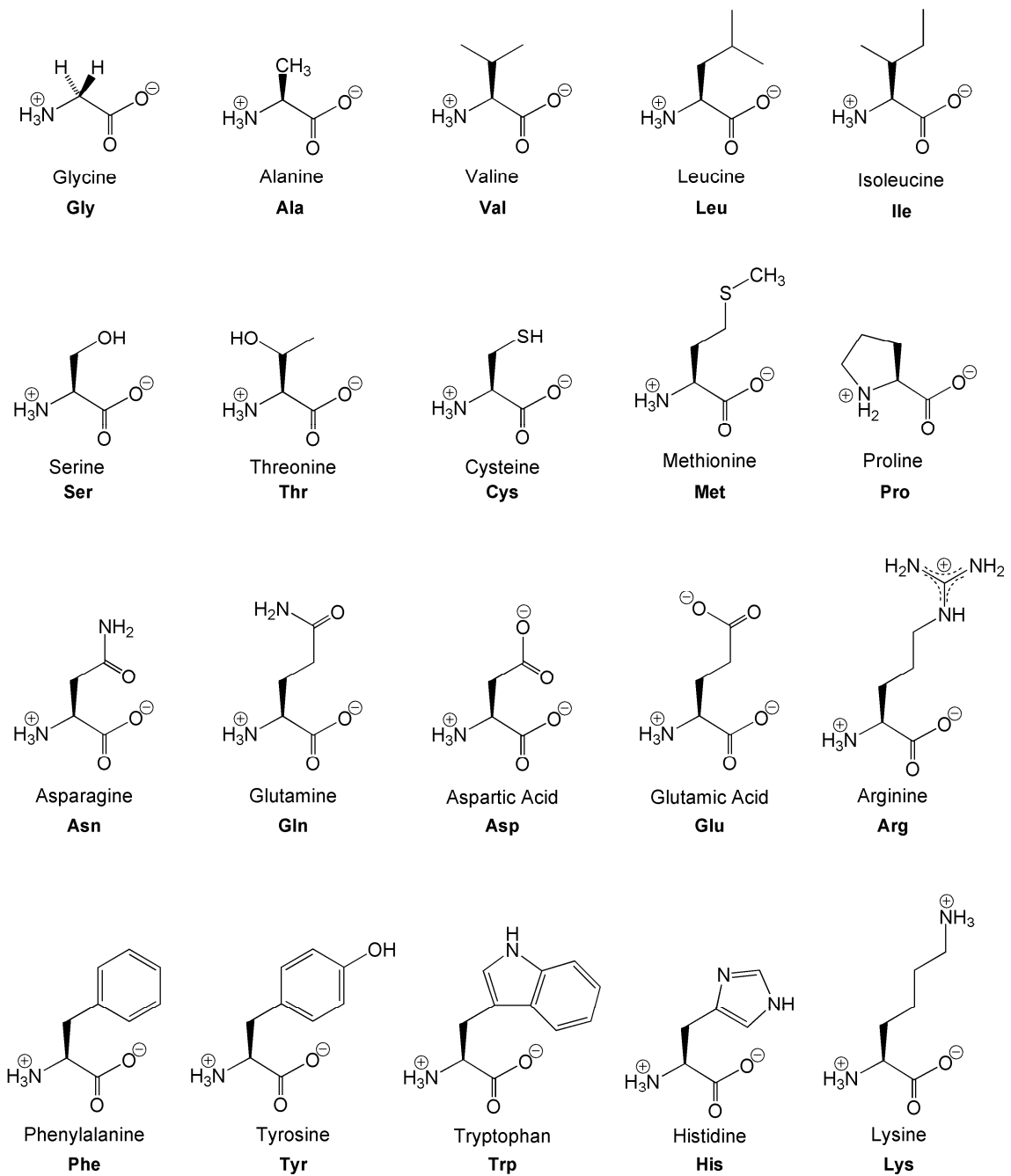


Figure 1.3: The twenty most common amino acids found in biological systems.

The formal charges on the nitrogen and oxygen atoms, in the zwitterionic model of amino acids (Figure 1.2 and Figure 1.3), are determined by the pK_a of the functional group. For example, for all amino acids the pK_a of the carboxylic acid moiety is *ca.* 2; and the pK_a of the protonated amine is *ca.* 10. pH dependence of amino acid protonation and charge may be seen in Figure 1.4. At very acidic pH values, the amino acid will be fully protonated and will have a cationic charge, while at basic pH values the amino acid will be fully deprotonated and will hold an anionic charge. At neutral pH values, the amino acid will hold both positive and negative charges (depending on the exact solution pH value and the pK_a of the R-group). The amino acids in subsequent figures will show the expected structure at biological pH; however, if a different pH is specified, the appropriate structure will be drawn.

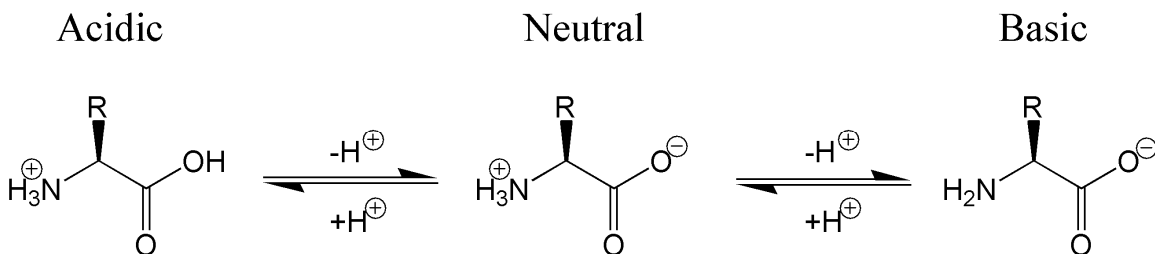


Figure 1.4: pH equilibria of an amino acid.

The overall and individual moiety charges of an amino acid in solution will affect the properties of that solution (such as ionic strength). Ionic strength is directly related to the concentration (c) and charge (Z) of the ions within a solution, and is calculated using equation 1.¹⁷ Zwitterions have been found to have no effect on the ionic strength of a solution.¹⁸ As a result of this, when calculating the ionic strength of a solution containing an amino acid, the pH of the solution must be obtained and the relative ratio of cations, anions and zwitterions must be taken into account.

$$\text{ionic strength} = \frac{1}{2} \sum cZ^2 \quad (1)$$

Mercury and lead are known to disrupt the function of proteins and enzymes by interacting with electron-donating Lewis basic atoms in biomolecules. In order to understand the chemistry of these metals within biological molecules and biological systems, the coordination of metals by electron-donating atoms (such as nitrogen, oxygen and sulfur) in amino acids and peptides must be studied. This coordination chemistry, however, is dependent on the physical and chemical properties (such as, oxidation state, radius, concentration, degree of hydration, coordination with Lewis basic atoms, pH and solution redox status) of these two toxic, trace metals.

1.4 CHEMISTRY OF MERCURY AND LEAD

Three general forms may be considered when examining the speciation of toxic, trace metals—elemental metal, inorganic salts and organo-metal (where the metal is incorporated into a carbon framework). Although metals in each of these three forms can be studied with respect to the effect on biological systems, the majority of discussion in this document will focus on lead or mercury salts of the most common oxidation state(s) of each metal.

1.4.1 Relativistic Effects

Although the relativistic effects on electron velocity and mass may be calculated for all elements, they only become significant for an element with an atomic number greater than or equal to 79.¹⁹ If the theory of relativity is applied to these higher mass elements, increasing the atomic number (Z) increases the electron velocity (v) (equation 2) and, in turn, the relative mass (m) of the electrons (equation 3), where n is the quantum number, e is the elementary charge, h is Plank's constant, m₀ is the electron rest mass and c is the speed of light.

$$v = \left(\frac{2\pi e^2}{nh} \right) Z \quad (2)$$

$$m = m_0 \left(1 - \frac{v^2}{c^2} \right)^{-1/2} \quad (3)$$

This increase in electron mass and velocity affects both the energy of the electrons and the symmetry of the orbitals. This is especially important for the core electrons closest to the nucleus. As a consequence of the higher mass effect, *s*-orbitals (to a greater extent) and *p*-orbitals (to a lesser extent) decrease in size and contract around the nucleus resulting in increased shielding of the *d*-orbitals and *f*-orbitals, which in turn become more dispersed. Orbitals with orbital angular momentum quantum number(s) greater than zero ($l > 0$), such as the three degenerate *p*-orbitals, will split into two subgroups of different energy and symmetry (indicated by the subscript fractions in Figure 1.5).¹⁹ A qualitative diagram of this orbital splitting is shown in Figure 1.5, where the 6*p* orbitals split into one 6*p*_{1/2} and two 6*p*_{3/2} orbitals and the 5*d* orbitals split into two 5*d*_{3/2} and three 5*d*_{5/2} orbitals.¹⁹

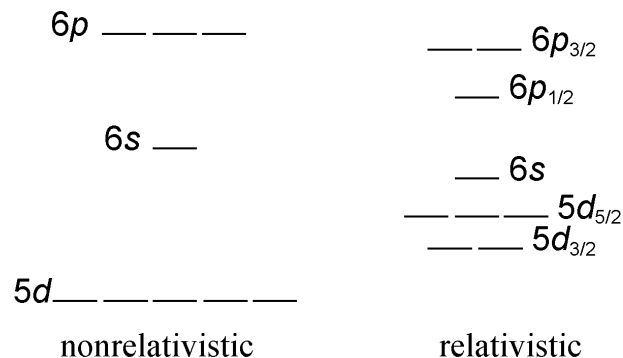


Figure 1.5: Qualitative diagram of heavy element atomic orbitals when relativistic effects are taken into account. (Adapted from reference 19)

These changes in orbital energy and symmetry are termed *relativistic effects*. For mercury and lead, relativistic effects and the stabilization of the 6s electrons are responsible for a number of chemical phenomena associated with each element.

Stabilization of the outermost 6s electrons of mercury(0) results in weaker interatomic interactions for mercury(0) than those of gold(0) or cadmium(0). The weaker mercury(0) interactions result in a liquid state for the metal rather than a solid state (as for gold(0) and cadmium(0)), which would involve stronger interatomic interactions.

Loss of the 6s electrons affords both mercury(I) and mercury(II) as stable oxidation states of mercury in aqueous conditions. Mercury(I) is found as the cluster compound Hg_2^{2+} , and is the only water soluble metal dimer.¹⁹ Calculating to the change in Gibbs energy from the reduction potentials in the mercury Latimer diagram for acidic environments, Figure 1.6, the disproportionation from the mercury(I) dimer to mercury(II) and mercury(0) is non-spontaneous. However, this dimeric pair may be considered as a Lewis acid-base interaction between the Lewis acid mercury(II) cation and the weak Lewis base mercury(0) atom,¹⁹ and as such, in acidic conditions with a stronger Lewis base present in solution, mercury(I) readily disproportionates to mercury(II) and mercury(0).

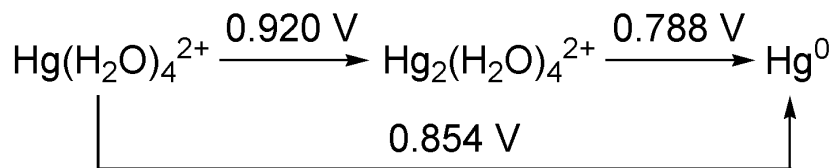


Figure 1.6: Latimer diagram for mercury in acidic solutions. (Adapted from ref. 20)

The so called *inert pair* of electrons in lead(II) are the stabilized 6s electrons. Due to the atomic 2+ charge and the 6s² electron stabilization, formation of the higher oxidation state lead(IV) is disfavoured. Ionization energies (IE) of the 6s electrons are much higher than that of the 6p electrons, as seen in Table 1.3. As a result, the most stable oxidation

states of the heavy *p*-block elements are thallium(I), lead(II) and bismuth(III) as opposed to thallium(III), lead(IV) and bismuth(V).

Table 1.3: Ionization energies of four metals. Shaded values are ionization energies of the 6*s* orbital electrons. (Adapted from reference 21)

Metal	IE1	IE2	IE3	IE4	IE5
Mercury	1007	1810	3300	4400	
Thallium	589	1971	2878	4900	6100
Lead	715	1450	3081	4083	6640
Bismuth	703	1610	2466	4372	5400

1.4.2 Hard-Soft Acid-Base Theory and Donor-Acceptor Strength

The biomolecules discussed in Section 1.3 Biological Molecules all contain electron-donating atoms (Lewis bases), such as sulfur, oxygen or nitrogen. According to Pearson's hard-soft acid-base theory, sulfur (as S²⁻) is described as a soft Lewis base while oxygen (as O²⁻) and nitrogen (in NH₃ and RNH₂) are described as hard Lewis bases. Of the two second row elements, oxygen is described as a harder base than is nitrogen. The trace metals with which these elements interact are designated as borderline Lewis acids (as in the case of lead) and soft Lewis acids (as in the case of mercury).²² The hardness or softness designation is arbitrary and was used initially to describe the behaviour of preferential acid-base interactions, where soft Lewis bases form adducts with soft Lewis acids and hard Lewis bases interact electrostatically with hard Lewis acids. Soft atoms are said to contain diffuse orbitals which are easily polarizable, conversely, the orbitals of hard atoms are less diffuse and so less polarizable.

Metal-ligand interactions result from the symmetry dependent combination of the orbitals of the metal and the ligand, or more specifically from the enhanced stabilization of the highest occupied molecular orbital (HOMO) of the Lewis base upon combining with the orbitals of the Lewis acid that possesses the same symmetry (such as, potentially, the

lowest unoccupied molecular orbital (LUMO)). According to the Hard-Soft Acid-Base theory, soft acids interact preferentially with soft bases (forming covalent interactions through favourable orbital overlap) over hard bases, and the opposite is true for hard acids (forming ionic pairs). Figure 1.7 shows the frontier orbital diagram comparison of hard acid-hard base and soft acid-soft base interactions, in each case the HOMO is stabilized (lower in energy) upon acid-base interaction.

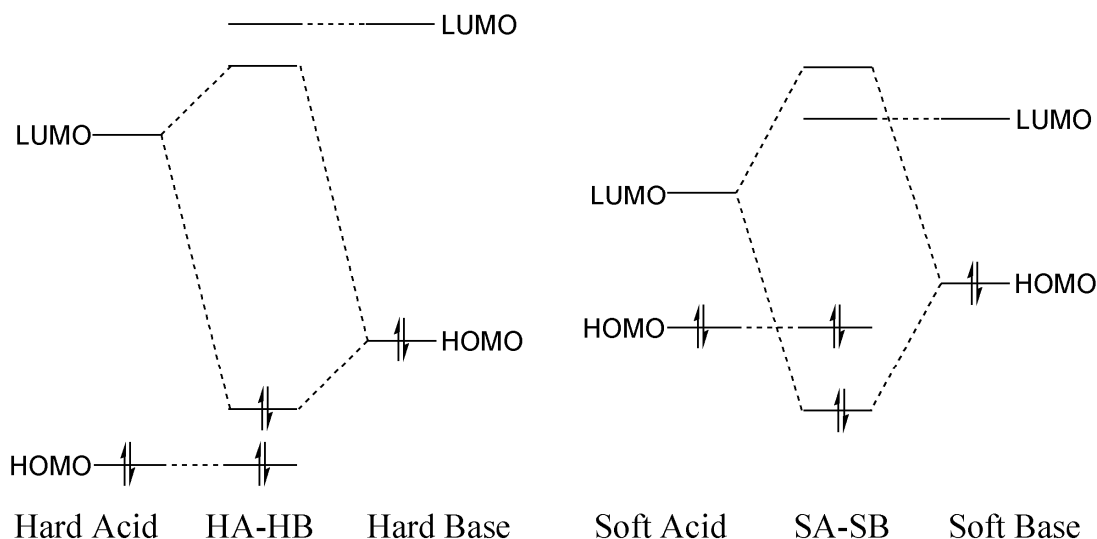


Figure 1.7: Idealized frontier orbital diagram of a) a hard acid-hard base interaction (HA-HB), and b) a soft acid-soft base interaction (SA-SB). (Adapted from reference 23)

Hardness is not the only characteristic that must be taken into account when comparing acid-base interactions; donor (or acceptor) strength is also a factor. If two bases of equal softness are in competition for a soft acid, the stronger donor will preferentially form complexes with the acid. However, if there is a large difference in softness, and the weaker donor is softer and has more favourable orbital overlap with the acceptor, then the weaker base will preferentially complex with the acid.

1.4.3 Donor-Acceptor Complexes

Within the adducts (or complexes) that form from metal-ligand interactions, the metal is the Lewis acid and the ligand is an atom or a molecule that contains Lewis basic atoms that donate electron density to the metal centre. Although hardness or softness and donating or accepting strength of the acids and bases affect complex formation, the form of the complex will also depend on the number of atom attachments to the metal, the state in which the complex is studied (i.e. solid, liquid, gas, or aqueous) and the stability of the complex itself.

Due to the large atomic radius of the heavier elements (relative to lighter elements in the same group) and to the large number of orbitals available for bonding, heavier elements have a larger coordination sphere than do the lighter elements. This means that more ligands can coordinate to heavier elements, giving higher coordination numbers. Table 1.4 contains a range of the known coordination numbers and the van der Waals radii of mercury and lead.^{21;24;25}

Table 1.4: Known coordination numbers and van der Waals radii for mercury and lead.

Metal	Coordination Number (ref. 24;25)	van der Waals Radius (pm) (ref. 21)
Mercury	2 - 8	155
Lead	2 - 10	202

The coordination environment about a metal can be separated into two spheres, the inner coordination sphere and the outer coordination sphere, Figure 1.8. The inner coordination sphere includes all atoms that are bonded to the metal centre, giving the coordination number of the metal. The outer coordination sphere includes atoms that are more distant and have more of an electrostatic (non-covalent) interaction with the metal.

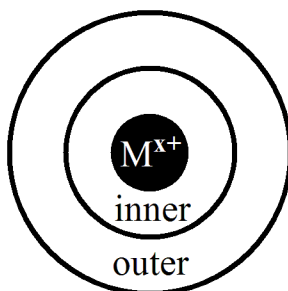


Figure 1.8: Coordination spheres of a metal cation in the solid state.

As the strength of a bond increases, the bond length decreases so that there can be a range of bond lengths within the inner coordination sphere. In this document, the maximum limit of the inner sphere radius has been defined as the sum of the van der Waals radii of the metal and bonded ligand atom.

1.4.4 Solid State Coordination Geometries of Lead(II)

The coordination geometry of all metals is dictated by both electronic and steric factors. The effect of relativity on the frontier orbitals of lead gives rise to two general coordination geometries of a lead(II) centre.

Due to the relativistic contraction of the s orbitals, it has been proposed that there is a decrease in the overlap between the s orbitals and any ligand orbital possessing appropriate symmetry, leaving an *inert pair* of electrons in the $6s$ orbital which do not take part in bonding.^{19;26;27} The geometry of the structures is said to be affected by this lone pair. That is, the ligands on some lead solid state structures are hemidirected (fill a portion of the coordination sphere) with a *stereochemically active lone pair* while others are holodirected (fill the whole coordination sphere) with a *stereochemically inactive lone pair*, Figure 1.9.²⁵ Using the *valence shell electron pair repulsion* model and *valence bond theory*, the lone pair orbital in the hemidirected case possesses both s and p character while the lone pair orbital in the holodirected case has only s character.²⁵

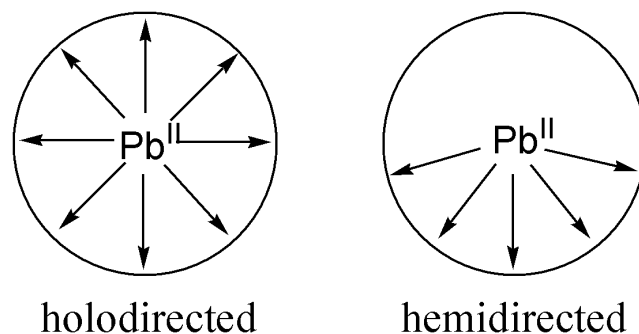


Figure 1.9: Holodirected and hemidirected coordination of lead(II). (Adapted from reference 25)

Rationalization of the solid state geometry in terms of this lone pair of electrons is potentially flawed as the initial explanation was developed to justify the observed geometries and does not take into account the tendency of decreased orbital hybridization as one descends a Group in the Periodic Table. Another explanation of the observed geometries would be a ground state effect of ligand coordination to the metal centre, or a *pseudotrans*-influence of the coordinating ligands. In the case of an oxygen donor, mixing of the filled oxygen $2p$ and empty lead $6p$ orbital would lead to weaker ligand interactions at the coordination site opposite the oxygen atom, and thus result in a hemidirected geometry about the metal centre.²⁸

The factors that dictate the holo- or hemidirection of the coordination sphere include: hardness of the donor atom, where soft donors lead to a holodirected geometry and hard donors generally lead to a hemidirected geometry; steric bulk of the ligands, where steric crowding leads to holodirected geometry; and coordination number of the lead centre.²⁵ In general, lead(II) atoms with coordination numbers of 2 to 5 are hemidirected, those of coordination number 9 and 10 are holodirected and those of intermediate coordination numbers, from 6 to 8, may be either hemidirected or holodirected. Of the hemidirected geometries with coordination numbers of 7 and 8, lead-oxygen bonds are prevalent within the structure.²⁵

An issue that may confuse the hemidirected and holodirected geometry discussion is the defined inter-atom distance limit of each lead centred sphere. For example, when viewing some intermediate coordination number complexes that contain lead-oxygen bonds, three lead-oxygen distance ranges are seen: 2.3-2.6 Å (short), 2.6-2.9 Å (intermediate) and 2.9-3.54 Å (long), where 3.54 is the sum of the van der Waals radii,^{25;29} Bond lengths in holodirected geometries generally have intermediate bond distances, Figure 1.10. Hemidirected geometries will have short bonds directly opposite the “empty” hemisphere (through the lead) and additional long bond interactions within the “empty” hemisphere. Inclusion of these long bond interactions, however, implies a holodirected geometry, by the broadest meaning of the term.

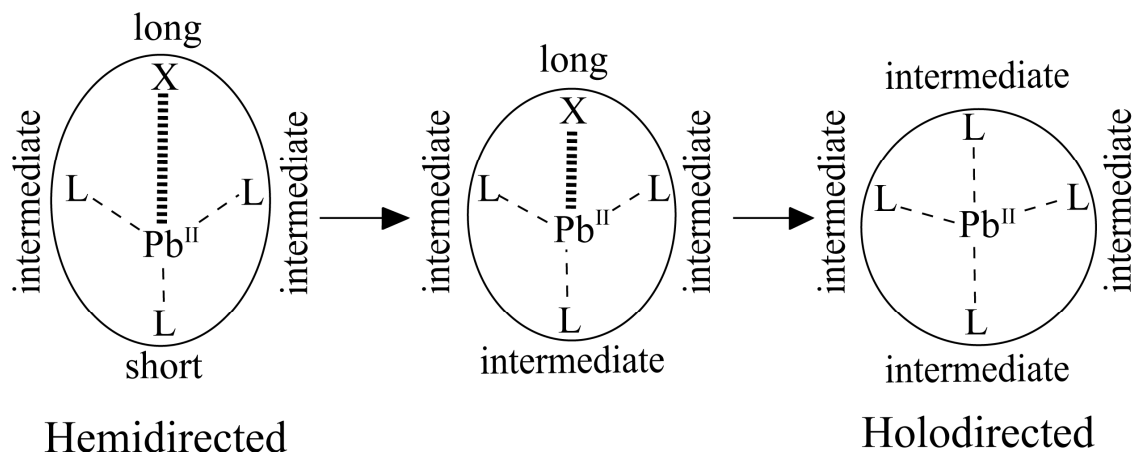


Figure 1.10: Bonding interaction diagrams ranging from the hemidirected geometry and holodirected geometry extremes. L is a ligand coordinated at short and intermediate distances and X is a ligand with long range interactions. (Adapted from reference 25)

Six solid state lead-amino acid complexes have been previously characterized and all were found to have hemidirected geometries, at the shorter bond length range.

Crystallographic data have been reported for complexes involving protonated aspartate³⁰ (AspH), valine³¹ (Val), phenylalanine³² (Phe), proline³³ (Pro), as well as for the non-biological amino acids D-penicillamine³⁴ (DPen) and 3,5-dinitrotyrosine³⁵ (DNTyr), Figure 1.11. Within this set of structures, five were synthesized in aqueous environments (Figure 1.11 a, b, d, e, f) and three were synthesized in acidic environments (Figure 1.11 a, b, e). The lead-valine complex (Figure 1.11b) will be discussed in this document, as it was isolated by a different method to that previously published.

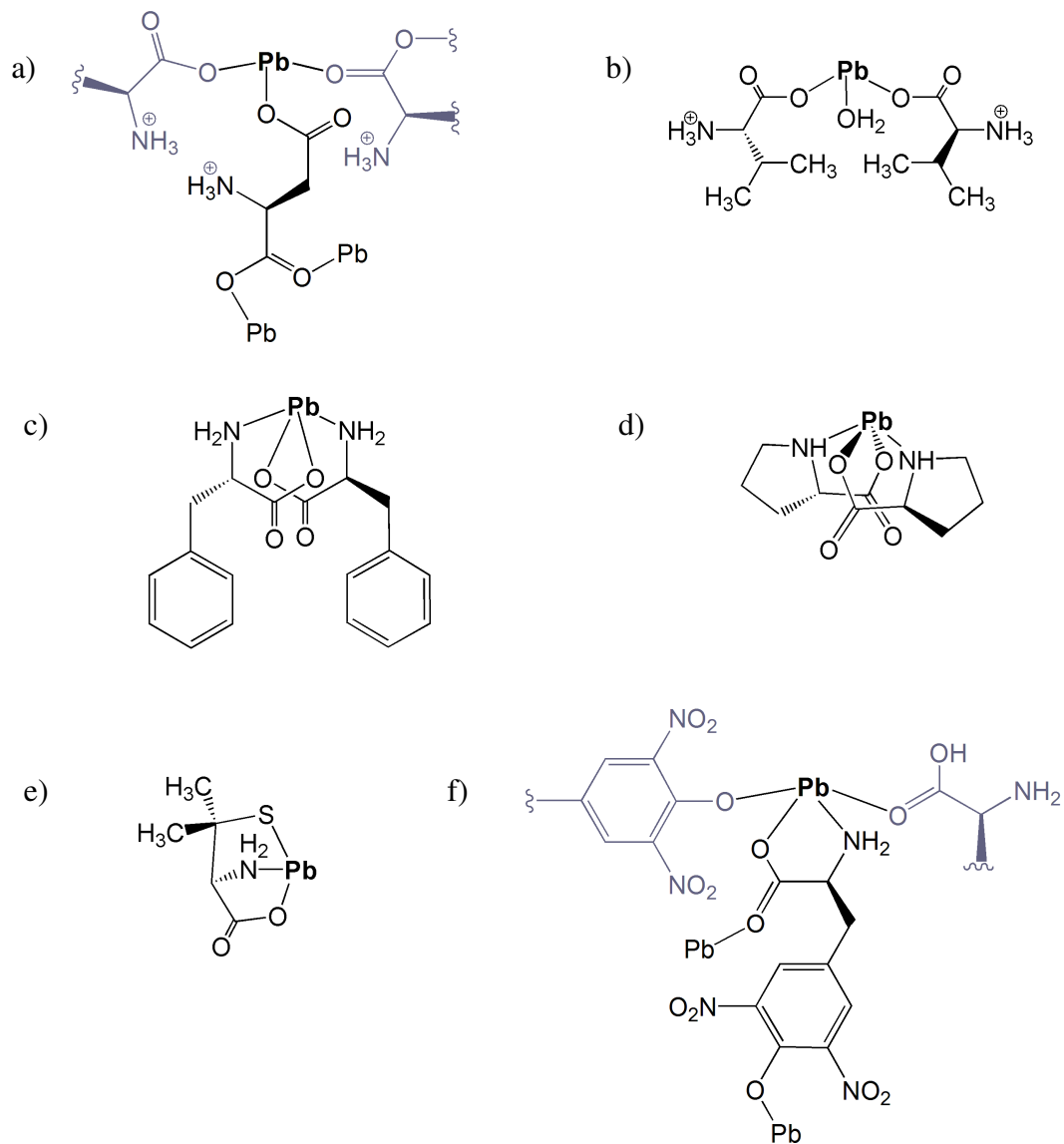


Figure 1.11: Diagrams showing the coordination geometry of the known solid state lead-amino acid complexes (only the shortest lead-heteroatom bonds are drawn).

a) $\text{Pb}(\text{AspH})(\text{NO}_3)$,³⁰ b) $\text{Pb}(\text{Val})_2(\text{H}_2\text{O})_2(\text{NO}_3)_2$,³¹ c) $[\text{Pb}(\text{Phe})_2]_n$,³²
d) $[\text{Pb}(\text{Pro})_2(\text{H}_2\text{O})]_n$,³³ e) $\text{Pb}(\text{DPen})$,³⁴ f) $\text{Pb}(\text{DNTyr})(\text{H}_2\text{O})_{0.5}$.³⁵

1.4.5 Solid State Coordination Geometries of Mercury

The coordination geometries of mercury(I) and mercury(II) result from the hybridization of the 6s and 6p_{1/2} orbitals of mercury. This hybridization leads to a linear geometry of the shortest bonds for both mercury(I) and mercury(II). Additional mercury-ligand interactions are usually also present and fill the inner coordination sphere of the atom.

In a study of sixteen minerals containing mercury(I) dimers,³⁶ mercury(I) and oxygen containing minerals were found to have Hg-Hg bond lengths of *ca.* 2.5 Å, Hg-O bond lengths between 2.0 Å and 2.3 Å, and relatively linear Hg-Hg-O bond angles (167° to 178°). Additional Hg···O interactions were found at a greater distance, in the range of 2.6 Å to 2.9 Å. In addition, the distance between the mercury(I) dimers ranged from 3.4 Å to 4.0 Å.

This linearity and distance of the mercury-oxygen bonds is also evident in complexes containing mercury(I)-carboxylate oxygen interactions, Figure 1.12 and Table 1.5. In these structures, adjacent units are connected by more distant Hg···O interactions (dotted lines in Figure 1.12) and form long polymeric arrays.

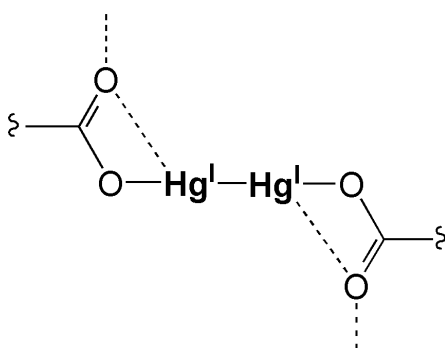
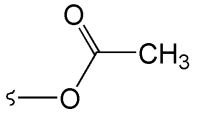
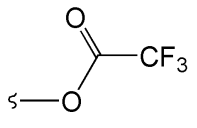
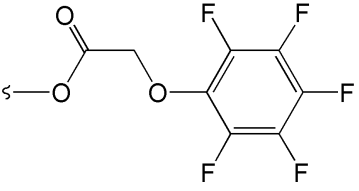
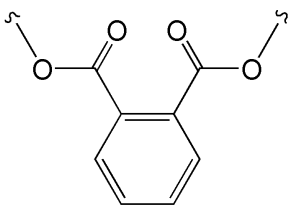


Figure 1.12: Mercury(I)-oxygen interactions in complexes containing mercury(I) and a carboxylate group. The dashed lines indicate distant interactions from an oxygen atom to a mercury(I) atom.

Table 1.5: Bond lengths and bond angles of known mercury(I)-carboxylate complexes.

Ligand [†]	Hg-Hg Bond Length(s) (Å)	Hg-O Bond Length(s) (Å)	Hg-Hg-O Bond Angle(s) (°)	Hg...O Bond Length(s) (Å)	Ref.
 acetate	2.5202	2.152	178.0	2.776 [2.6802]	37
 trifluoroacetate	2.505	2.14	166.6	2.81 [2.64] [2.88]	38
 (perfluorophenoxy)acetate	2.514	2.13	173.9	2.82 [2.63]	39
 <i>o</i> -phthalate	2.519	2.08 2.16	175 171	Not Reported	40

[†] Lines on the oxygen atoms directed away from the carboxylate groups indicate attachment to a mercury(I) centre.

Mercury is classified as a soft Lewis acid and, as such, preferentially bonds with soft Lewis bases. This property is very evident in the bonding preferences of mercury(II), where mercury(II) will form short covalent bonds with softer nitrogen or sulfur atoms over harder oxygen atoms on an amino acid.⁴¹ The linear geometry found in mercury(I) complexes is also evident in mercury(II) complexes. The shortest bonds for this oxidation state are generally trans across the metal centre; however, additional longer interactions are usually present and result in a coordination number greater than two for the mercury atom. Diamminemercury(II) dication would be the ideal case of a mercury(II) centre coordinated by nitrogen donors, Figure 1.13. In this example, Hg-N bond lengths are 2.07 Å and the N-Hg-N bond angle is 180°.⁴¹

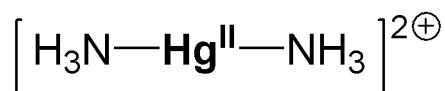


Figure 1.13: Diagram of diamminemercury(II) dication, with a linear geometry through the mercury centre.

Complexes containing organic or inorganic mercury(II) with amino acid ligands have been crystallographically characterized (amino acid = alanine,⁴²⁻⁴⁴ cysteine,^{45;46} glycine,⁴² histidine,⁴⁷ methionine,⁴⁸⁻⁵⁰ proline,⁵¹ serine,⁵² tryptophan,^{53;54} tyrosine,⁵⁵ N-acetyltryptophan,⁵⁴ 2-amino-4-phenylbutanoic acid,⁵⁵ ethionine,⁵⁶ homocysteine,⁵³ S-methyl-cysteine,^{48;56} and penicillamine;^{49;57-59} and the dipeptide glycylglycine⁶⁰); a linear geometry about the mercury(II) centre is evident in each case. Diagrams of selected examples of these complexes showing the general connectivity are presented in Figure 1.14 and the bond lengths and angles are listed Table 1.6.

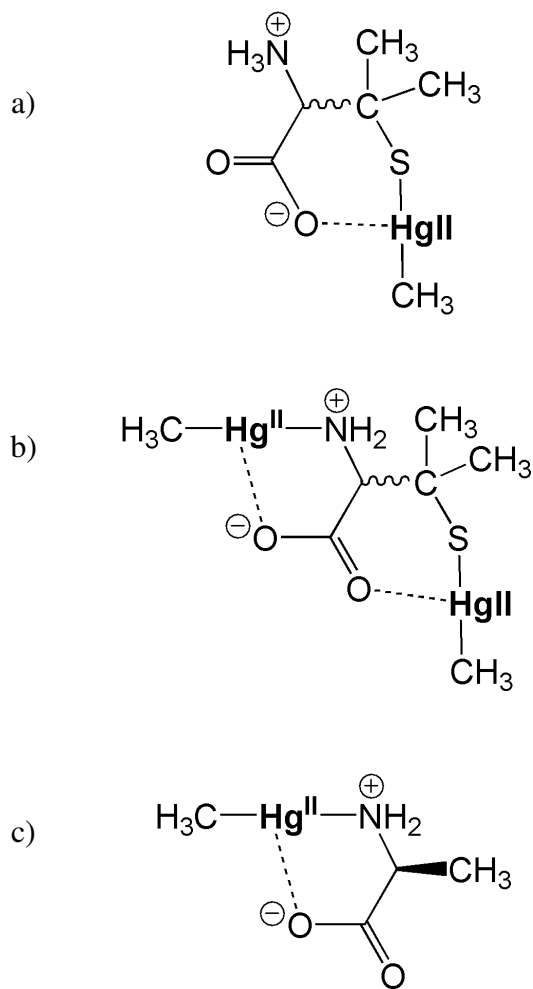


Figure 1.14: Diagram of methylmercury-amino acid coordination in a) $[\text{HgCH}_3(\text{DLPen})] \cdot \text{H}_2\text{O}$,⁵⁸ b) $[(\text{CH}_3\text{Hg})_2(\text{DLPen})]$,⁵⁸ and c) $\text{CH}_3\text{Hg}(\text{DLAla})$.⁴² Long Hg-O interactions are indicated by the dashed lines.

Table 1.6: Bond lengths and bond angles of the three methylmercury-amino acid complexes found in Figure 1.14.

Complex	Hg-S Hg-N Bond Lengths (Å)	Hg-CH ₃ Bond Lengths (Å)	S/N-Hg-CH ₃ Bond Angles (°)	Hg...O Bond Lengths (Å)	Ref.
[HgCH ₃ (DLPen)]•H ₂ O	2.38 (S)	2.07	175	2.88	58
	2.36 (S)	2.09	175	2.89	
[(CH ₃ Hg) ₂ (DLPen)]	2.35 (S)	2.04	176	2.85	58
	2.13 (N)	2.07	170	2.72	
				2.92 (S)	
CH ₃ Hg(DLAla)	2.14 (N)	2.04	175.6	2.63	42
				2.92	
				3.05	

1.4.6 Solution Chemistry of Metal Ions

As with metal ions in the solid state, it can be imagined that ions in the solution state are surrounded by coordination spheres (Figure 1.15). In the primary (inner) coordination sphere all ligands, including solvent molecules, are coordinated to the metal ion.

Molecules in the secondary sphere are influenced by the metal ions and the coordinated molecules (ligands and solvent). As the distance from the ion increases, the effect of the ion on the solvent molecules decreases (from the disordered to the bulk phases).

In solution the exchange of ligands or solvent molecules may be very dynamic, where a solvent molecule will exchange places with a ligand and coordinate to the metal centre, and vice versa.⁶¹ The rate at which the molecules exchange depends on the lability and the strength of the metal-ligand and metal-solvent interactions and the concentration of each component in solution.⁶² When studying the metal-ligand interactions, if the exchange is very dynamic and is faster than the rate at which the interaction can be

observed, then only an average interaction will be detected.⁶³ Also, if the concentration of ligands in solution is low, and the ligand-metal interaction is weak and labile, then for the majority of the time solvent molecules will be coordinated to the metal.⁶²

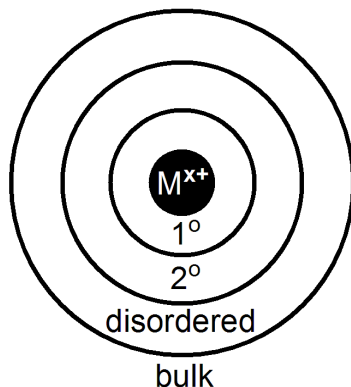


Figure 1.15: Idealized diagram of polar solvent coordination spheres (primary, secondary, disordered spheres) about a metal cation (M^{x+}). (Adapted from reference 64)

Ionic strength is a property of a solution that is affected by the quantity and charge of ions in solution. As mentioned previously, zwitterions have no effect on the ionic strength of a solution, but, as ions in a solution, zwitterions will interact electrostatically with the solvent and other ions.¹⁸

Upon coordination to the metal ion, solvent molecules may undergo a chemical reaction with the metal, but these reactions will depend on the solution pH and electropotential.⁶⁵ Both mercury and lead form stable, insoluble oxides with water at neutral pH values, Figure 1.16. These oxides are in dynamic equilibrium with the metal cations and by varying the pH of the solution, at intermediate acidic pH values (*ca.* pH 3 to 5) either oxide or ion will be present in solution.

More specifically to this report, at intermediate acidic pH values and based on the protonation equilibria of amino acids (Figure 1.4), both cationic and zwitterionic forms of an amino acid will be present in solution. This means that at these intermediate pH values, an amino acid may be protonated, metallated or remain as a free zwitterionic molecule in solution (Figure 1.17).⁶⁶

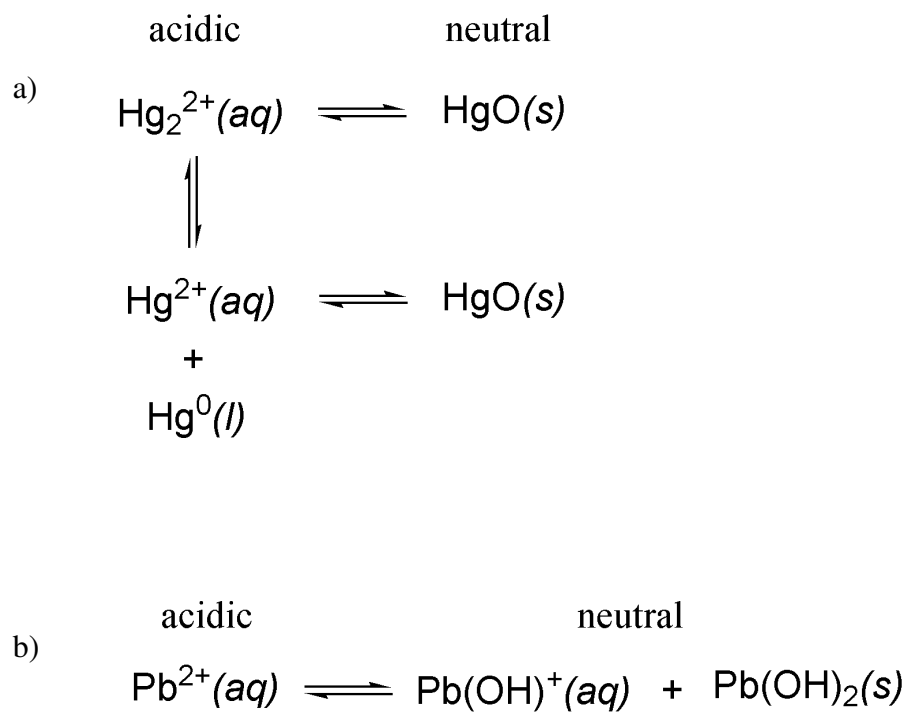


Figure 1.16: Formation equilibria of a) mercury oxide and b) lead hydroxide. (Adapted from reference 65)

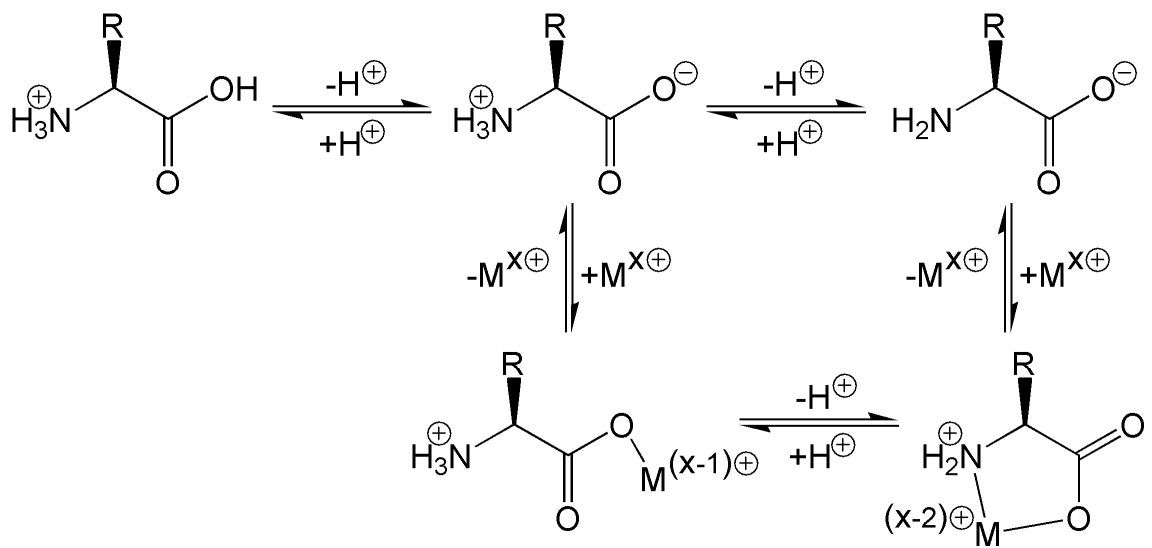


Figure 1.17: Protonation and metallation equilibria for amino acids.

1.4.7 Gas Phase Metal-Ligand Complexes

Electrospray ionization (ESI) mass spectrometric analysis of metal with ligand solutions allows for the definitive identification of kinetically stable complex ions in the gas phase. The formation of these complexes gives insight into metal-ligand coordination ratios in solution and, potentially, the strength of the metal-ligand interaction, but not the coordination geometry of the metal centre.⁶⁷ A discussion of the ESI mass spectrometric method may be found in Section 1.5.3.

Trace metal-amino acid complex cations have been definitively identified in the gas phase from ethanol/water solutions of six metal nitrates (cadmium(II), mercury(I), mercury(II), thallium(I), lead(II), and bismuth(III)) and the twenty common amino acids, Figure 1.3, as well as homocysteine (HCys, formula: $\text{SHCH}_2\text{CH}_2\text{CH}(\text{NH}_3^+)\text{COO}^-$).⁶⁸ As seen in Table 1.7, the complexes contain not only the metal and amino acid in question but may also contain solvent and counter anions. Clusters with large numbers of metals and ligands were also present in the gas phase and, as with the solvent and counter ion containing adducts, were most likely present as a result of the electrospray process.

Mixtures of glutathione (a tripeptide shown in Figure 1.18) with chlorides, nitrates or oxides of heavy *p*-block or late *d*-block cations (cadmium(II), mercury(II), thallium(I), lead(II), arsenic(III), antimony(III) or bismuth(III)) in ethanol/water solutions were analysed by both positive and negative ion ESI-MS.⁶⁹ The thiophilicity of these metals and metalloids was evident by the fragmentation patterns exhibited during the tandem analysis, where the fragment ions consistently contained both metal and sulfur atoms.

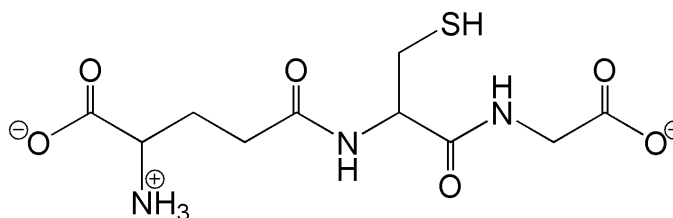


Figure 1.18: Diagram of glutathione, a sulfur containing tripeptide composed of glutamic acid-cysteine-glycine.

Table 1.7: Mercury-amino acid and lead-amino acid complexes detected in the gas phase.
(Adapted from reference 68)

	Gly	Ala	Val	Leu	Ile	Phe	Trp	Tyr	His	Met	Cys
Hg ^I	1:1		1:1 ^a	1:2	1:2	1:1	2:1	1:1	1:2	1:2	1:2
	1:1 ^a		2:1 ^a	2:3	2:3	1:2	2:2 ^c	1:2	2:2	2:3	
				2:4	2:4		3:3 ^c		2:3		
				2:4 ^c	3:4						
				3:4	4:4						
			4:4								
Hg ^{II}	1:1 ^a	1:1 ^a	1:1 ^a	1:1	1:1	1:1	1:2	1:2	1:2	1:1	1:2
	3:3	1:2		1:1 ^a	1:1 ^a	1:1 ^b		2:2	2:3	1:2	2:3
		2:2		1:2	1:2	1:2		2:3		2:2	
		2:3		3:3	3:3	1:2 ^b				2:3	
		3:3				2:2					
					2:3						
Pb ^{II}	1:1	1:1	1:1	1:1	1:1	1:1	1:1	1:1	1:1	1:1	1:1
	2:3	1:1 ^c	1:1 ^c	1:2	1:2	1:2	1:2		2:2	1:2	1:2
		1:2	1:2	2:2	2:2	2:2	2:2		2:3	2:2	2:2
		2:2 ^a	2:2 ^b	2:3	2:3	2:3	2:3			3:2	
		2:3	2:2 ^c	2:3							
		2:3									
	HCys	Ser	Thr	Asp	Glu	Asn	Gln	Lys	Arg	Pro	
Hg ^I		1:1	1:1			1:2		1:1	1:2	1:1	
			2:3			2:3		1:2	2:2	2:3	
								2:2	2:3		
								2:3	3:4		
							3:3				
Hg ^{II}		1:2	1:1	2:2 ^a	2:2	1:1	2:2	1:1	1:1	1:1	
		2:2	1:2			1:2	2:3	1:2	1:2	2:3	
		2:3	2:2			1:3		2:2	2:2		
		3:2	2:3			2:2		2:3	2:3		
		3:3	3:3			2:3					
					3:3						
Pb ^{II}	1:1	1:1	1:1	1:1	1:1	1:1	1:1	1:1	1:1	1:1	
	1:2		2:2	2:2	2:1	1:2	2:2	2:3	1:1 ^c	1:1 ^c	
	2:2		2:3	2:3	2:1 ^b	2:2	2:3		1:2	1:2	
			3:3	3:3	2:2	2:3			1:2 ^c	2:3	
									1:3		
									1:3 ^c		
								1:4 ^c			
								1:5 ^c			
								1:6 ^c			

^a Ethanol adduct

^b Water adduct

^c Nitrate adduct

1.5 CHARACTERIZATION TECHNIQUES

A number of characterization techniques have been used to study the interactions between trace metals and biomolecules—among these methods are Raman spectroscopy, infra-red (IR) spectroscopy, potentiometry, X-ray absorption spectroscopy (XAS), nuclear magnetic resonance spectroscopy (NMR), X-ray crystallography, and mass spectrometry (MS). Different properties of each metal (Table 1.8) and of atoms coordinating to the metal centre are the basis for each characterization technique. For example, in order for an element to be detected using NMR spectroscopy, the nucleus must be NMR active and have a nuclear spin greater than or equal to $\frac{1}{2}$, while metal complex analysis using MS involves an isotope pattern comparison of the natural abundance and mass of each naturally occurring isotope.

The state of the sample will dictate the type of analysis that can be performed. Liquids can be analysed with XAS, NMR, and the other spectroscopic techniques, solids can be analysed using solid state NMR, XAS, X-ray crystallography and vibrational spectroscopic techniques, and mass spectrometry is used to analyse samples in the gas phase.

Although each of these experimental techniques provides vital information about the connectivity or interactions of metals and biomolecules, three techniques will be discussed in this report as primary analytical tools: X-ray crystallography, solid state and solution state NMR spectroscopy, and MS with an ESI source. Raman spectroscopy and IR spectroscopy will be discussed as secondary techniques which were used to provide further information about isolated or detected complexes.

Table 1.8: Properties of mercury and lead.²¹ (Bolded entries indicate isotopes or oxidation states that will be discussed in the text.)

Metal	Stable Oxidation States	Isotope(s)	Natural Abundance (%)	Nuclear Spin	Covalent and Ionic Radii (Å)
Mercury	0 I II	¹⁹⁶ Hg	0.14	0	r _{covalent} 1.44
		¹⁹⁸ Hg	10.02	0	
		¹⁹⁹Hg	16.84	1/2	
		²⁰⁰ Hg	23.13	0	Hg ^I r _{ionic} 1.27
		²⁰¹ Hg	13.22	3/2	Hg ^{II} r _{ionic} 1.12
		²⁰² Hg	29.80	0	
		²⁰⁴ Hg	6.85	0	
Lead	0 II IV	²⁰⁴ Pb	1.4	0	r _{covalent} 1.54
		²⁰⁶ Pb	24.1	0	
		²⁰⁷Pb	22.1	1/2	Pb ^{II} r _{ionic} 1.32
		²⁰⁸ Pb	52.4	0	

1.5.1 X-Ray Crystallography

Analysis of solid state structures using X-ray crystallography can provide invaluable information of metal-complex geometries (including, bond lengths and angles) in the solid state. The technique is highly dependent, however, on the availability of high quality crystals for analysis.⁷⁰

Crystallizations are perceived by some chemists as fickle procedures, because the products of crystallization on one day may seem unattainable on all others. By carefully studying each system and taking clear notes on the procedure (and environment) of each crystallization, the reproducibility of a crystallization can be improved. Solution pH, concentration, temperature, solvent (or combination of solvent) used, reactant purity, rate of evaporation or mixing, and size of crystallization vessel are among the variables which must be taken into account during a crystallization.⁷¹

As the name implies, the single crystal X-ray diffraction technique involves the collection of two-dimensional X-ray radiation patterns that result from the diffraction of a beam of

X-ray radiation by a single crystal.⁷⁰ These two dimensional patterns are collected over a large number of incident angles. The X-rays interact with the electrons in each atom of the crystal and the relative three dimensional location of electron density may be calculated from the two dimensional pattern and reflection intensity.⁷⁰ Areas of higher electron density are used to indicate the location of an atom.

The absorption coefficient of a compound is a value which describes how well a compound absorbs light. In X-ray crystallography, absorption of X-rays increases with atomic number so that the heavier elements (such as mercury and lead) give more intense reflections than do the lighter elements.⁷⁰

A number of solutions (models) are applied to the resulting diffraction patterns and the three dimensional atomic positions are calculated. In these models, the molecular geometry of the molecule must chemically make sense. Least squares refinement of the observed and calculated data provides estimated standard deviation values for the atom coordinates.⁷⁰ These values will propagate in the calculations of bond lengths and angles.

Crystalline order is of significant importance to the method so that a reliable diffraction pattern can be attained. In some structures, however, functional groups or molecules in the crystal may be disordered (found in more than one position). Disorder can arise from molecular vibrations (dynamic disorder) or two or more energetically equivalent positions (static disorder).⁷⁰ If disorder is present within a structure, the occupancy of each position is calculated and reported as the *site occupancy factor* (SOF).

Model reliability is evaluated by use of an R-factor given in equation 4, where observed (F_{obs}) and calculated (F_{calc}) structure factors, F , are related to reflection intensity, I (equation 5), and are summed over all angles.⁷² This R-factor value is used to determine the closeness of the observed and calculated structure factor values. Low R-factors (in this work less than *ca.* 0.07) indicate a good refinement of the data and solution. The Goodness of Fit (GOF) value is also used to compare the calculated and observed structure factors, in this case an ideal structure and model combination would have a GOF value of one.⁷³

$$R = \frac{\sum ||F_{obs}| - |F_{calc}||}{\sum |F_{obs}|} \quad (4)$$

$$I_{hkl} \propto |F(hkl)|^2 \quad (5)$$

Because single crystal X-ray diffraction is used to examine only one crystal from a sample of multiple crystals, a question arises as to whether or not the single crystal data is representative of the bulk of the sample or if it is one of a variety of solid state structures within the sample. To answer this question a portion of the bulk of the sample should be analysed using a method such as elemental analysis (EA) and/or solid state NMR (ssNMR) spectroscopy.

1.5.2 Nuclear Magnetic Resonance Spectroscopy

NMR Spectroscopy is an excellent tool for the elucidation of the structure of compounds in the solid and solution states. The technique involves initially aligning the nuclear spin progression of the atoms within a sample to an external magnetic field (B_0), then applying an additional magnetic field (B_1), at a particular radiofrequency, which realigns the nuclear spin progressions, followed by detecting the relaxation back to the original alignment.

The spin of a nucleus, or the *spin quantum number* (I), is the combination of the spins of the protons and neutrons within the nucleus.⁷⁴ The nuclear spin progression is the motion of the spin about the direction of the magnetic field. The value of I can be equal to or greater than zero, where a specific value of I is associated with each isotope of an element.

A nucleus with an I value of zero has no magnetic properties; these include carbon-12 and oxygen-16. Those nuclei with I values of one half and greater have magnetic properties and are NMR active. That is, these nuclei have magnetic moments which can

be affected by the external and applied magnetic fields. For spin $\frac{1}{2}$ nuclei, two possible spin states are available, one pointing in the direction of the external magnetic field (+z) and one in the opposite direction (-z), and both these spin states are populated following the Boltzmann distribution. Those nuclei of spin one and greater have additional spin states, all of which are populated to a different extent.

Of the NMR active nuclei, those with I equal to $\frac{1}{2}$ are most practical in NMR analyses.^{63;74} The magnetic properties of the spin $\frac{1}{2}$ nuclei discussed in this work are found in Table 1.9. Those nuclei with I values greater than and equal to one are called *quadrupolar nuclei*. These nuclei have faster relaxation times and give broader lines in NMR spectra than the spin $\frac{1}{2}$ nuclei and as such are more difficult to detect.

Table 1.9: Properties of five spin $\frac{1}{2}$ nuclei of interest.⁷⁵

	^1H	^{13}C	^{15}N	^{199}Hg	^{207}Pb
Natural Abundance [%]	99.9885	1.07	0.386	16.87	22.1
Magnetogyric Ratio, γ [$10^7 \text{ rad s}^{-1} \text{ T}^{-1}$]	26.7522	6.7283	-2.7126	4.8458	5.5805
Relative NMR Frequency [MHz]	100.0	25.1	10.1	17.9	20.9
Relative Receptivity	1.000	1.70×10^{-4}	3.84×10^{-6}	1.00×10^{-3}	2.01×10^{-3}
Suggested Reference Compound(s)	TMS DSS [†]	TMS DSS [†]	CH_3NO_2	$(\text{CH}_3)_2\text{Hg}$	$(\text{CH}_3)_4\text{Pb}$

TMS = Tetramethylsilane

DSS = 2,2-Dimethyl-2-silapentane-5-sulfonic acid (3-Trimethylsilanyl-propane-1-sulfonic acid) or the sodium salt

[†]DSS is a substitute for TMS as an internal standard in highly polar solvents.⁷⁵

The magnetic moment of a nucleus is proportional to the magnetogyric ratio.⁷⁴ The larger the magnitude of this ratio, the larger the effect an external magnetic field has on the nucleus. The natural abundance and magnetogyric ratio of an isotope can be combined to give the relative receptivity of the isotope (relative to that of hydrogen-1). The lower the relative receptivity value of a nucleus, the more difficult it is to detect in an NMR experiment, such as for nitrogen-15.

The frequency of the precessional motion of a nucleus (the Larmour frequency) is directly proportional to the magnetogyric ratio of and the magnetic field felt by the nucleus.⁷⁶ When observing one isotope, the spin of each nucleus in a molecule will precess at a different frequency (resonance frequency) depending on the strength of the magnetic field, the environment of the nucleus, and the shielding of the nucleus from the magnetic field by the electrons. This means that the oxidation state of the atom, the identity of neighbouring bonded atoms, the type and strength of chemical bonds in the molecule, and the through space interactions between atoms will affect the resonance frequency.

In an NMR experiment, resonance frequencies (Hz) are used to identify nuclei in different chemical and magnetic environments.^{63;76} Since a resonance frequency is affected by the external magnetic field (frequency in MHz), the ratio of the two frequencies (Hz/MHz) is reported as the chemical shift of the nucleus, in units of parts per million (ppm). In order to compare different samples, the chemical shifts are calibrated to an internal or an external standard (Table 1.9). In aqueous solutions, 3-trimethylsilylpropane sulfonic acid or its sodium salt (DSS), at a concentration of 10 mM, is the suggested internal standard for carbon-13 and hydrogen-1 NMR experiments.⁷⁵

The precession of nearby NMR active atoms in a molecule will also affect the chemical shift of a nucleus by splitting the spin states of that nucleus.⁷⁴ This is a magnetic effect known as *coupling*. Both the number of bonds and three dimensional geometry between the NMR active nuclei affect the extent of coupling, where three or four bond coupling is usually the detectable limit.

For example, in a C-H bond, both carbon-13 and hydrogen-1 are spin $\frac{1}{2}$ (NMR active). Viewing from the perspective of the carbon atom, there would be a one bond coupling between the carbon-13 and hydrogen-1 atoms (denoted $^1J_{CH}$) and the carbon chemical shift would be split into two signals by the hydrogen-1. When determining the coupling of the atoms, the isotopic abundance of the nuclei must also be taken into account. The natural abundance of carbon-13 is 0.1 %, while NMR inactive carbon-12 is 99.9 % abundant. This means that in a C-H bond, only 1 out of 1000 hydrogen-1 atoms will be bonded to (and the chemical shifts split by) a carbon-13 atom. The other chemical shifts of the other 999 hydrogen-1 atoms are not split and will only give one signal. The signals that result from carbon-13 coupling are called *satellite peaks*.

In the solution state, interactions with the solvent or other molecules also affect the environment of the nucleus. These interactions (solvent effects, ionic strength effects, concentration effects, ligand exchange) will change the chemical shift of the nucleus and the shape of the resulting peak in the NMR spectrum, and must be taken into account during spectral analysis.^{63;76}

The detected chemical shift of a nucleus is the average of the environments felt by that nucleus on the NMR time scale. This means that fast, dynamic interactions may only result in one signal while the slow, dynamic interactions may result in more than one chemical shift. Broad chemical shifts are indicative of dynamic interactions or the presence of a nearby quadrupolar nucleus. If a dynamic exchange is very fast on the NMR time scale (less than 10^{-4} s)⁶⁴ then the single peak will not be broadened to a great extent. However, by decreasing the temperature of the NMR sample, these dynamic processes may be slowed enough to be observed.

Metal and proton/deuteron interactions with amino acids will affect the chemical shift of the interacting nuclei to differing extents.⁶⁶ Since both metal and proton/deuteron are in solution, the detected interactions will depend on the concentration of the interacting element. In order to make a comparison of the effects of metal ions or protons/deuterons on the chemical shifts of the amino acids, the pH or pD of a solution needs to be measured and taken into account in the analysis. Also, because deuterium has slightly

different chemical properties than hydrogen,⁷⁷ a pH probe must be calibrated in order to measure the pD of a solution.^{78;79}

During solid state NMR analysis of crushed crystals, the through space (*dipole-dipole*) interactions of NMR active nuclei and the orientation of the molecules with respect to the magnetic field (*chemical shielding anisotropy*) will give rise to a large number of potential nuclear environments.⁷⁴ Dipole-dipole interactions can be eliminated during the NMR experiment by applying a second strong magnetic field to the sample.

Each nucleus in a different three dimensional orientation to the external magnetic field will have its own chemical shift. In solution, the molecules are tumbling so that an average of the shifts is detected, the *isotropic shift*. In solid state analysis, anisotropy effects can be removed by mimicking the three dimensional tumbling of solution.⁷⁶ This is done by spinning the solid state sample at a *magic angle* ($54^{\circ}44'$) to the external magnetic field (magic angle spinning, MAS). The resulting spectrum shows signals for the isotropic shift and spinning side bands, where the frequency difference between the side bands is the frequency of the sample spinning speed. If multiple sample spinning speeds are used, the isotropic shift can be identified as it will not change position while the spinning side band positions will change.

High relative receptivity value allows for facile detection of lead-207 signals in NMR analyses.⁸⁰ However, the large chemical shift range (17000 ppm) may make locating a lead signal difficult as the chemical shifts are affected by the structure of the complex, the substituents and the coordination number of lead.⁸⁰ Lead-207 NMR analysis of lead nitrate solutions with glycine showed a pD dependence of the lead-amino acid interaction.⁶⁶

Mercury-199 also has a high NMR receptivity value and a large chemical shift range.⁸¹ Of the two oxidation states, mercury-199 signals of mercury(II) salts are at a higher field than those of mercury(I). For example, comparing the acetate salts the mercury-199 chemical shift for $\text{Hg}(\text{OAc})_2$ is -2497 ppm and for $\text{Hg}_2(\text{OAc})_2$ is -1450 ppm.⁸² In general, lower oxidation numbers are expected at higher fields. The exception in the case of

mercury-199 is most likely due to the effect of the Hg-Hg bond of mercury(I) dimers.⁸¹ Broadening of the mercury-199 line widths occurs in spectra of solutions that contain both mercury(I) and mercury(II) ions.⁸³ This is most likely due to the rapid exchange between the mercury centres, Figure 1.19.⁸³

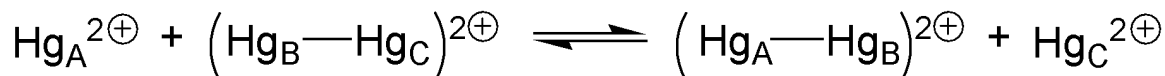


Figure 1.19: Exchange equilibrium between mercury(I) and mercury(II).

Mercury(II)-cysteine interactions in aqueous solutions were studied using mercury-199 NMR spectroscopy.⁸⁴ Based on the chemical shifts and at the concentrations studied, 10 % to 15 % of the mercury centres in solution are coordinated by three cysteine molecules.

Hydrogen-1 and carbon-13 NMR spectroscopy was used to study lead(II)-cysteine and lead(II)-glutathione interactions in aqueous (deuterated water) solutions over a large pD range with a variety of starting material stoichiometries.⁸⁵ Lead was found to be coordinated by the sulfur atom of the amino acid and tripeptide forming 1:1 and 1:2 lead to bioligand complexes. Lead-cysteine complexation was not detected in acidic conditions (pD 1.8 to 2.4), while in basic conditions (pD 12.9) lead-cysteine interactions were present (this was attributed to the full deprotonation of cysteine at the higher pD values).

Methylmercury-glutathione interactions were studied using hydrogen-1 NMR spectroscopy.⁸⁶ A constant chemical shift value for the cysteinyl methylene protons over a large pD range indicated that coordination of the glutathione to the methylmercury was through the thiol moiety.

1.5.3 Electrospray Ionization Mass Spectrometry

Mass spectrometry is an analytical technique that is used to detect the presence of ions in the gas phase by separating the ions as a function of their mass to charge ratios (m/z). The separation is accomplished by applying an electric field and/or a magnetic field to ions within a defined space (distance, area or volume). The flight path and lifetime of an ion within the mass analyser are affected by both the applied fields and the geometrical space in which the ion travels. The difference in the flight paths (or velocity in the case of time of flight mass analysers) of the ions allows for their separation and subsequent detection.

Figure 1.20 shows the general mass spectrometric analysis scheme. The samples can initially be in the solid state, the solution state or the gas phase; however for ion separation to occur, the ions must be in the gas phase when they enter the mass analyser and the concentration of the ions must be very low to reduce inter-atomic collisions.⁸⁷

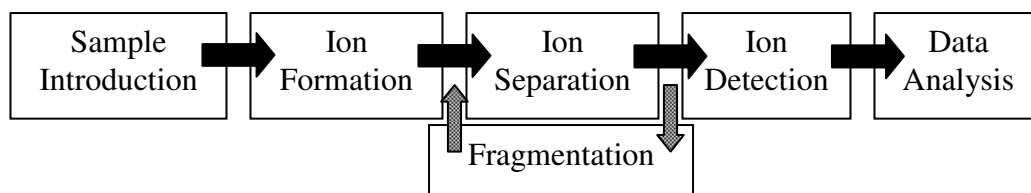


Figure 1.20: Schematic of the mass spectrometric process.

The method by which the molecules are vaporized and ionized depends on the initial phase of the sample and the chemical characteristics of the molecule or complex. A sample in the liquid state must first be brought into the gas phase and then ionized. Electrospray ionization (ESI) is a well known ionization technique used for the introduction of liquid samples to the mass analyser. It is a so called *soft ionization* technique, where the complex ion does not undergo a significant amount of fragmentation.

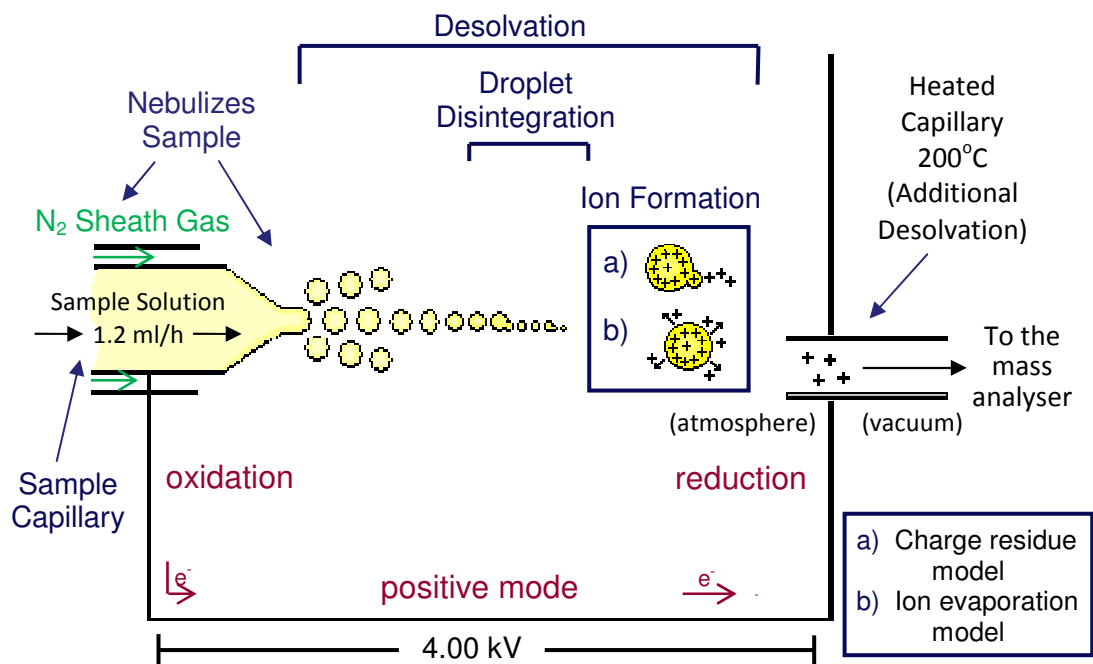


Figure 1.21: Electrospray ionization (ESI) source of the Finnigan LCQDUO ion trap. (Adapted from references 87;88)

ESI is an electrochemical process in which an electric potential (in the low kV range) is generated across the source (Figure 1.21). The sample is introduced to the source through a small, charged sample capillary. Some sample molecules are ionized by redox reactions within the sample capillary and subsequent charge and proton transfer between the sample molecules occurs resulting in the formation of molecular ions. At the tip of the capillary, similarly charged ions repel each other and collect on the solution surface. Droplets form as a result of both charge repulsion and the effects of a nebulizing sheath gas, and travel toward the charged plate and heated capillary. The charged plate is attached to the heated capillary is present in the ESI source of the mass spectrometer that was used for this work (Finnigan LCQDUO ion trap). This charged plate is negatively charged for the positive ion mode and positively charged for the negative ion mode.

When the charged droplets form, the sheath gas aids in the further reduction in size of the droplets by removing solvent molecules. This reduction in size concentrates the molecular ions and increases the charge density on the surface of the droplets. As charges continue to concentrate on the surface of the droplet, the Rayleigh limit is reached—this is the point at which the surface charge repulsion exceeds the surface tension of the droplet—resulting in droplet disintegration, by which smaller droplets bud off of the larger droplet yielding more surface area for the same volume. The droplets continue to desolvate and disintegrate until single ions (or very small clusters of ions) are released, completing the ion formation process.

Ions formed during the electrospray ionization process generally result from protonation or deprotonation of sample molecules or complexes. A protonated molecular ion is referred to as a *pseudomolecular ion*. The extent to which a molecule is protonated or deprotonated depends on the acidity of the protons on the molecule in relation to those on the other molecules in the system (such as solvent molecules or impurities).

As the ions leave the source they enter an area of lower pressure and continue to the mass analyser. In the mass analyser ions are separated by their mass to charge ratios (m/z). By varying the electric fields felt by the ions within the mass analyser, the trajectories of the ions with differing mass to charge ratios are differentiated. Ions of a selected mass to charge ratio can then be ejected from the mass analyser and detected. The resulting mass spectrum is a plot of the relative intensity as a function of the mass to charge ratio. In the experiments described in the subsequent chapters of this report an ion trap mass analyser was used. A general diagram of an ion trap is shown in Figure 1.22.

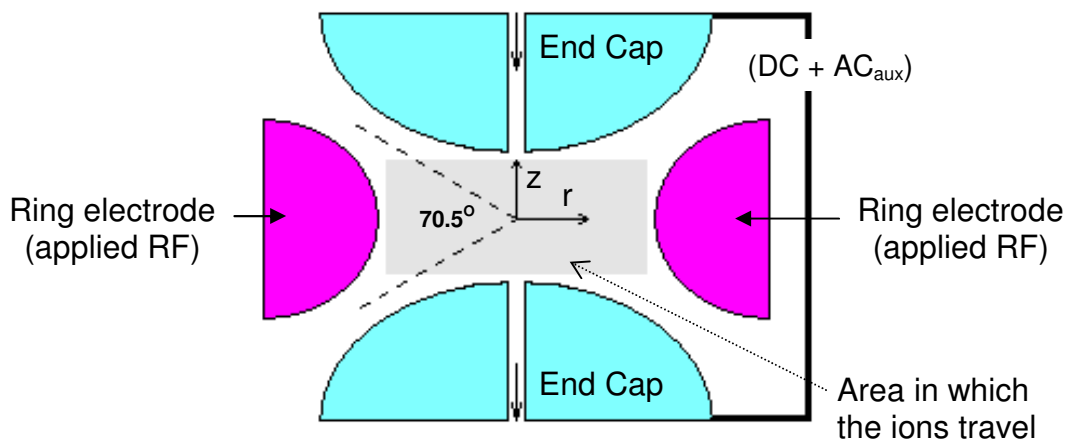


Figure 1.22: Diagram of the ion trap mass analyser. (Adapted from references 87;89)
 DC = direct current; RF = resonating radiofrequency; AC_{aux} = potential auxillary alternating current; r and z are the dimensions of the trap core

The intensity of the peak in a mass spectrum is a result of the ESI response of the complex. For example, if the complex is easily solvated or readily forms ion pairs in the charged droplets, then it will not easily form gas phase ions during the ESI process.⁶⁷

Metal containing complex ions of a particular mass to charge ratio that give a peak in the mass spectrum can be identified using two methods: an isotope pattern comparison and fragmentation the ions of a particular mass to charge ratio within the mass analyser.⁶⁷

The first method involves an examination of the isotope pattern of expanded mass spectral peaks. Such analyses are performed by comparing a calculated isotope pattern (using an isotope calculation program) to the experimental isotope pattern.⁶⁷ This method works well for mercury and lead because these metals have multiple naturally occurring isotopes.

For second described identification method, specific m/z values are selected to remain in the mass analyser. These ions are then bombarded with an inert gas (such as helium)

which results in ion fragmentation. These fragments have differing m/z values and differing trajectories. This process is known as tandem mass spectrometry (MS/MS).⁸⁷ Analysis of tandem mass spectra is an excellent method for verifying the identity of the ion selected for fragmentation. During fragmentation, logical neutral losses resulting from the breakdown of the complex ion are expected, leaving fragment ion peaks in the MS/MS spectrum.

As ESI is a soft ionization technique, metal-ligand complex ions are generally not fragmented during the ionization process and this method has been used to identify metal-organic molecule complex ions in the gas phase.⁸⁷ ESI-MS has been used to identify mercury-amino acid and lead-amino acid complex cations as discussed in Section 1.4.7.⁶⁸

1.5.4 Other Characterization Techniques

A number of other spectroscopic techniques have been used to study the interactions within metal-biological molecule complexes.

X-Ray Absorption Spectroscopy (XAS) involves the excitation of core electrons, of a particular element, resulting in an excited state of the atom. By fitting a calculated model to the observed absorption spectrum, information can be gleaned regarding the atom and the environment about the atom (such as, oxidation state and coordination number of the element of interest). The versatility of this technique is evident in the variety of sample states (such as, solids, liquids, solutions and gases) and the sheer number of elements that can potentially be studied; however, the availability of this technique is limited as a high energy tuneable X-ray source must be used, which is generally a synchrotron source.^{63;90} Among other examples, XAS has been used to study the coordination environments of lead(II) in sulfur-rich zinc binding proteins⁹¹ and the coordination environments of mercury(II) in solutions containing mercury with cysteine,⁸⁴ penicillamine,⁹² or glutathione.⁹³

Vibrational spectroscopies provide insight into the bonding interactions within a complex and these methods can also be used to study solids, solutions, liquids and gases. For IR spectroscopy, the vibrational modes that change the dipole moment of a molecule or complex will be detected.⁶³ This is done by observing the wavelengths of IR light that are absorbed (or transmitted) by the complex. Peaks within the resulting spectrum can then be associated with a particular vibrational mode of the elements within a bond (or set of bonds) and the entire spectrum can be used as a fingerprint for the complex. Complexes of lead(II) with cysteine and other thiol containing bioligands were studied using IR spectroscopy.⁹⁴ The sulfur-lead(II) interaction was found to be stronger than the carboxylate oxygen-lead(II) interaction.

Raman scattering results from vibrations that change polarization of the electron density of the complex in question. One wavelength of light is used to excite the electrons and the emitted wavelengths orthogonal to the incident light are detected.⁶³ Raman spectroscopy can be used to study both solid samples and aqueous solutions. Due to the high polarizability of the mercury(I)-mercury(I) bond and the effect of the ligands on each mercury atom,^{82,95-97} Raman spectroscopy may provide invaluable insight into mercury(I)-amino interactions in the solid state and the solution state.

1.6 SUMMARY

There is relatively little known about the specific biochemical effects of trace metals in biological systems. However, some information may be elucidated by examining relatively simple systems in which one metal interacts with one or two biomolecules. By studying the coordination environment of the metal and determining the metal and ligand content of the complexes that are formed, information can be discerned about the interactions of these metals with the atoms in biomolecules and subsequently the effect of trace metals on biological systems.

The main focus of the research presented in this document was the study of the interactions between lead or mercury and amino acids. Complexes that contain both

metal and amino acid(s) have been isolated in the solid state, and have been characterized in the solid state (by the use of X-ray crystallography, solid state NMR spectroscopy and vibrational spectroscopies), the solution state (using solution state NMR spectroscopy), and the gas phase (via ESI-MS). A range of techniques are used in order to gain a more complete picture of the system under study. Through these investigations the known biological coordination chemistry of lead and mercury has been advanced, and not only enhances our understanding of the toxic roles that these metals play in the human body but also may aid in the development of better treatments for metal poisoning.

CHAPTER 2 LEAD-AMINO ACID COMPLEXES

2.1 INTRODUCTION

Complexes of lead with L-valine, L-isoleucine, L-phenylalanine, or L-arginine, or with both L-valine and L-isoleucine (Figure 2.1) have been isolated from reaction mixtures containing lead(II) nitrate and the respective amino acid(s) in acidic aqueous solution. The compounds have been comprehensively characterized using X-ray crystallography, solid state nuclear magnetic resonance (NMR) spectroscopy and solution state NMR spectroscopy, Infrared (IR) and Raman spectroscopies, and electrospray ionization mass spectrometry (ESI-MS). In addition, the lead-valine-isoleucine and lead-arginine solid state structures are the first isolated heteroleptic lead-amino acid complex and the first isolated lead-cationic amino acid complex, respectively.

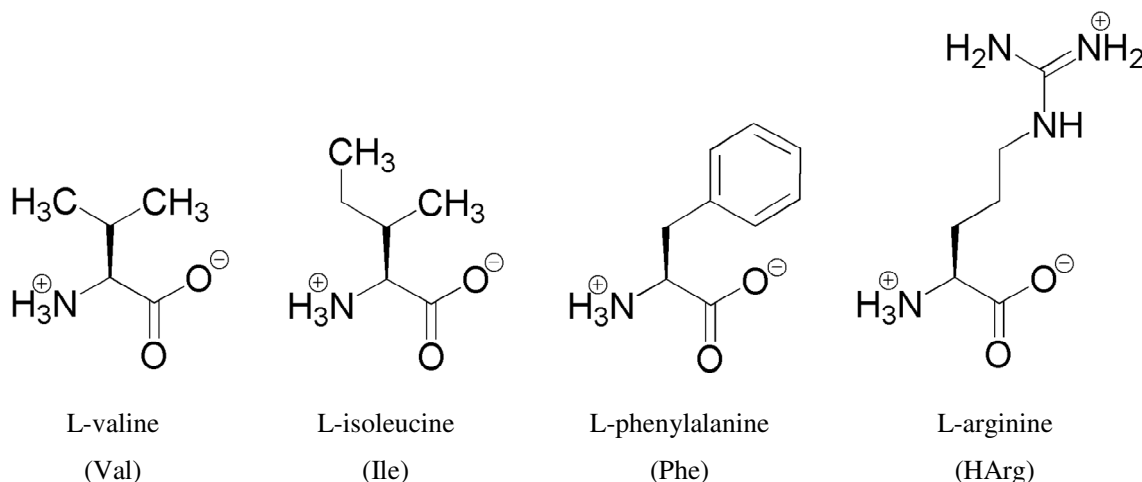


Figure 2.1: Amino acids of interest in Chapter 2.

The solid state structures of lead-phenylalanine, lead-isoleucine, lead-valine, and lead-valine-isoleucine complexes show a lead centre coordinated by the oxygen atoms from the carboxylic acid group of two amino acids. The lead-arginine complex is a cluster

involving two lead centres and three arginine molecules, where one lead centre has two amino acid ligands while the other has one amino acid ligand and a water ligand. The cationic arginine molecules coordinate to the metal centre through the carboxylate oxygen atoms.

2.2 RESULTS AND DISCUSSION: SOLID STATE CHARACTERIZATION

Appropriate conditions have been established for the crystallization of lead-amino acid complexes for valine, isoleucine, phenylalanine, arginine and a combination of valine and isoleucine. Heated (95-100 °C) mixtures of amino acid with lead nitrate in water resulted in clear, colourless solutions that give crystals by slow cooling and evaporation. The crystalline samples have been characterized as $[\text{Pb}(\text{OH}_2)_2(\text{Val})_2(\text{NO}_3)][\text{NO}_3]$, $[\text{Pb}(\text{OH}_2)(\text{Ile})_2][\text{NO}_3]_2 \cdot \text{H}_2\text{O}$, $[\text{Pb}(\text{OH}_2)_2(\text{Val})(\text{Ile})(\text{NO}_3)_2]$, $[\text{Pb}(\text{OH}_2)_2(\text{Phe})_2(\text{NO}_3)][\text{NO}_3]$, and $[\text{Pb}(\text{OH}_2)(\text{Phe})_2][\text{NO}_3]_2 \cdot 2\text{H}_2\text{O}$. $[\text{Pb}_2(\text{HArg})_3(\text{H}_2\text{O})(\text{NO}_3)_7] \cdot 3\text{H}_2\text{O}$ was isolated from a mixture of lead nitrate and L-arginine that was acidified with nitric acid, until the solution became clear (pH *ca.* 3), prior to heating. Solids were characterized using X-ray crystallography, IR, Raman and NMR spectroscopy, and aqueous solutions of redissolved crystals and reaction mixtures were characterized using NMR spectroscopy and ESI-MS.

2.2.1 Single Crystal X-Ray Diffraction: Lead-L-Valine

The previously published lead-L-valine complex,³¹ with a formula of $[\text{Pb}(\text{OH}_2)_2(\text{Val})_2(\text{NO}_3)][\text{NO}_3]$ (Pb-Val, Figure 2.2), was isolated following the method described above and was comprehensively characterized. The closest contacts (≤ 2.6 Å) in the asymmetric unit to the lead centre are from an oxygen atom of each valine carboxylate (Pb-O21 2.356(2) Å and Pb-O11 2.459(2) Å) and from the oxygen atom in a water molecule (Pb-O1 2.512(3) Å). The acute bond angles of these interactions (O1-Pb-O11 88.24(8)°, O1-Pb-O21 79.81(8)°, and O11-Pb-O21 76.26(8)°) reflect the hemidirected geometry of the coordination environment for lead. Within the next coordination sphere (≤ 2.9 Å) more distant lead-oxygen interactions are evident, from a second oxygen atom of a valine carboxylate group (Pb-O22 2.892(2) Å) and two oxygen

atom interactions from a nitrate counter ion (Pb-O33 2.790(3) Å and Pb-O32 2.847(3) Å). A holodirected geometry about the lead centre is evident within the van der Waals radii of lead (see Sections 1.4.4 and 2.2.7), where there are lead-oxygen interactions with an additional water molecule (Pb-O2 2.915(2) Å), the second oxygen from the carboxylate group (Pb-O12 3.266 Å) and two oxygen atoms from a nitrate counter ion (directly above the shortest Pb-O bonds) (Pb-O31' 2.969(3) Å and Pb-O33' 3.174(3) Å) leading to the two dimensional lead-nitrate chain.

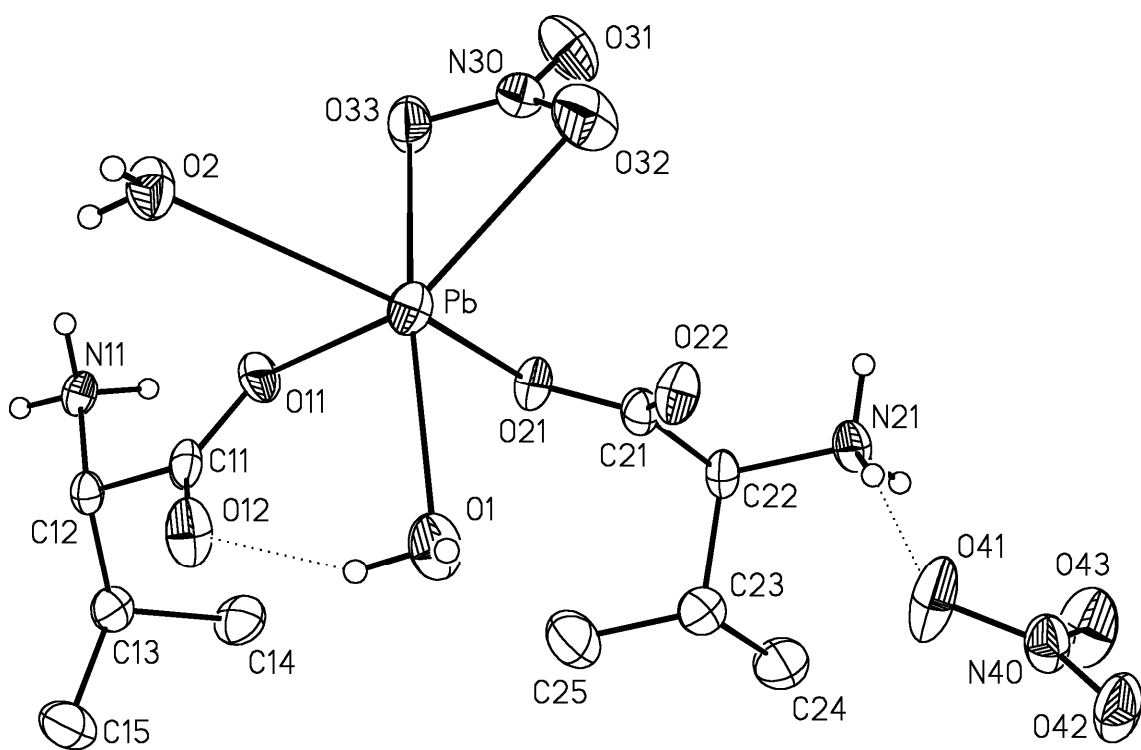


Figure 2.2: Perspective view of the asymmetric unit (unique atom set) of Pb-Val showing the atom labelling scheme. Non-hydrogen atoms are represented by Gaussian ellipsoids at the 50% probability level. Hydrogen atoms attached to oxygen or nitrogen atoms are shown with arbitrarily small thermal parameters; all other hydrogen atoms are not shown.

Each L-valine ligand coordinates to the lead centre through the carboxylate group, while the primary amine is protonated. N-H \cdots O hydrogen bonding within the structure occurs between the protonated amine functional groups and the oxygen atoms of the nitrate counter anions, a water molecule and a carboxylate group. The hydrogen atoms of the water molecules interact with oxygen atoms on carboxylate groups resulting in O-H \cdots O hydrogen bonds.

The R-groups of the valine molecules within the crystal structure are aligned and are directed into a “hydrophobic plane”—labelled R-group plane in the Figures—Figure 2.3. Between the R-group planes are the lead atoms, amino acid backbones and water molecules. These structural features are consistent in all of the other lead-neutral amino acid solid state packing discussed in this chapter.

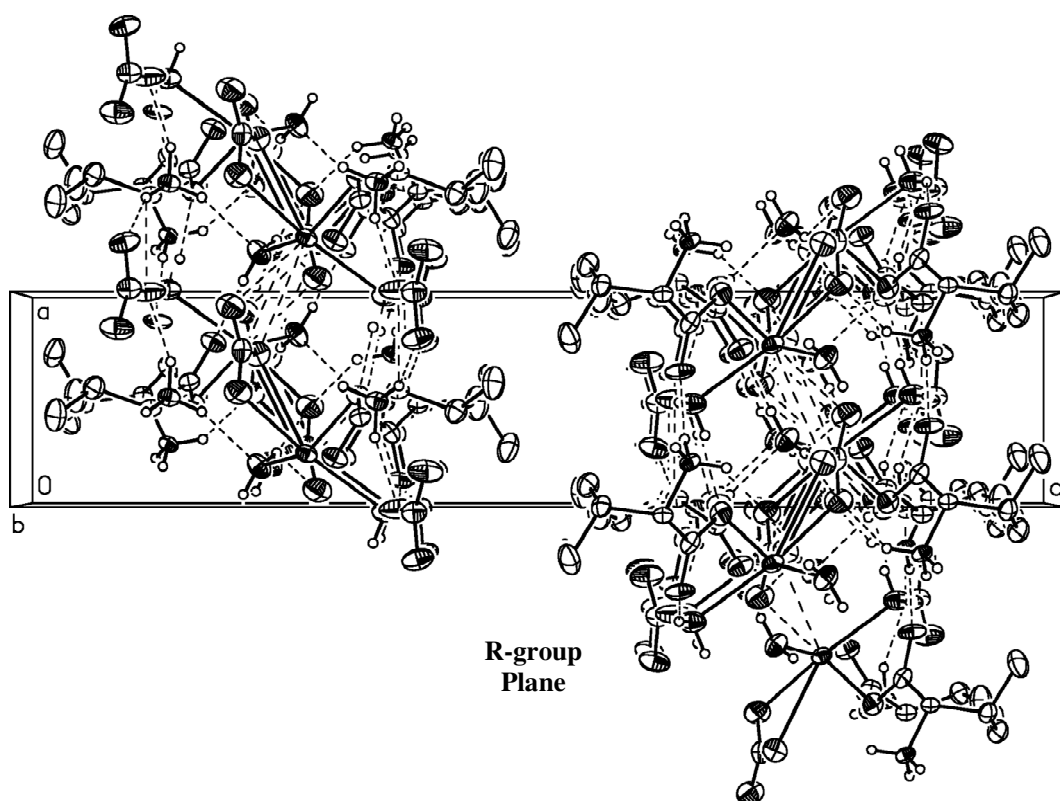


Figure 2.3: Illustration of crystal packing of Pb-Val, showing the vertical R-group planes. View direction is parallel to the crystal *b* axis.

2.2.2 Single Crystal X-Ray Diffraction: Lead-L-Isoleucine

With a formula of $[\text{Pb}(\text{OH}_2)(\text{L-isoleucine})_2][\text{NO}_3]_2 \cdot \text{H}_2\text{O}$, the asymmetric unit of the lead-isoleucine complex (Pb-Ile) contains one lead centre, two neutral zwitterionic L-isoleucine molecules, two water molecules and two nitrate counter ions (Figure 2.4). Within the smallest coordination sphere ($\leq 2.6 \text{ \AA}$), the lead centre has a hemidirected geometry and interacts with one oxygen atom from each isoleucine carboxylate group (Pb-O20 2.379(3) \AA and Pb-O10 2.492(3) \AA) and one water molecule (Pb-O1 2.497(3) \AA), giving acute bond angles of $76.30(8)^\circ$ (O10-Pb-O20), $79.55(9)^\circ$ (O1-Pb-O20) and $84.79(9)^\circ$ (O1-Pb-O10). Additional contacts occur in the next coordination sphere ($\leq 2.9 \text{ \AA}$), where the lead centre interacts with a second oxygen from one carboxylate group, an additional water molecule (Pb-O2' 2.907(2) \AA) and two oxygen atoms (Pb-O33 2.809(3) \AA and Pb-O31 2.824(3) \AA) from a nitrate counter anion. The coordination sphere is filled, within the sum of the van der Waals radii, with a nitrate counter ion from the adjacent asymmetric unit (Pb-O32" 2.934(3) \AA and Pb-O33" 3.106(3) \AA), forming a two dimensional chain of alternating lead(II) atoms and nitrate counterions.

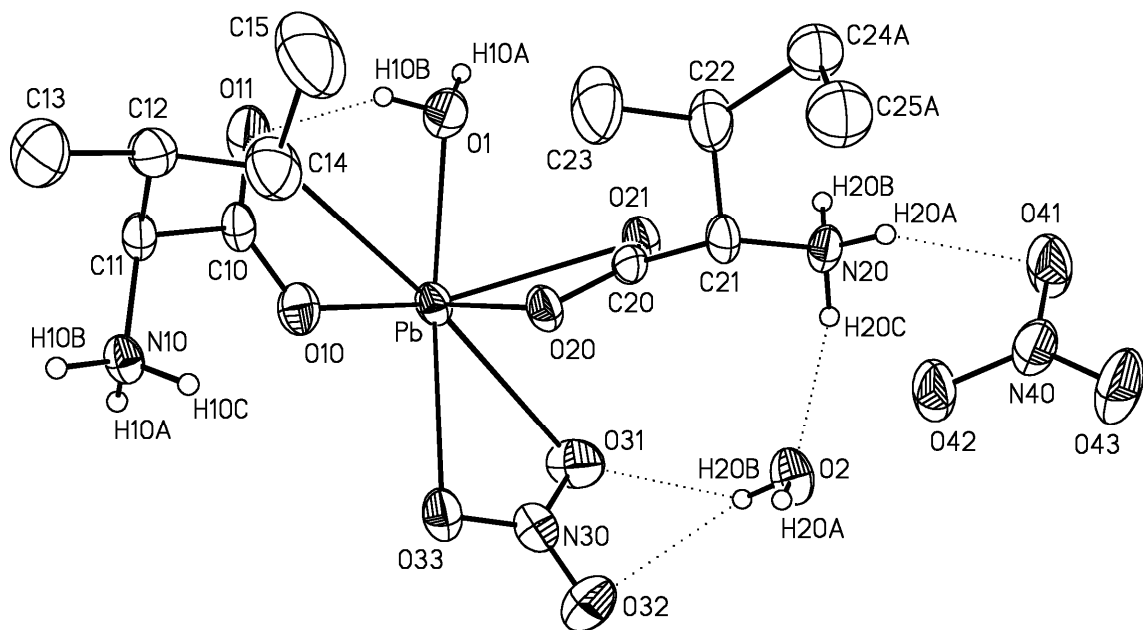


Figure 2.4: Perspective view of the asymmetric unit of Pb-IIe showing the atom labelling scheme (only one part of the disordered isoleucine ligand (carbon atoms C24A and C25A) are shown). Non-hydrogen atoms are represented by Gaussian ellipsoids at the 50% probability level. Hydrogen atoms attached to oxygen or nitrogen atoms are shown with arbitrarily small thermal parameters; all other hydrogen atoms are not shown.

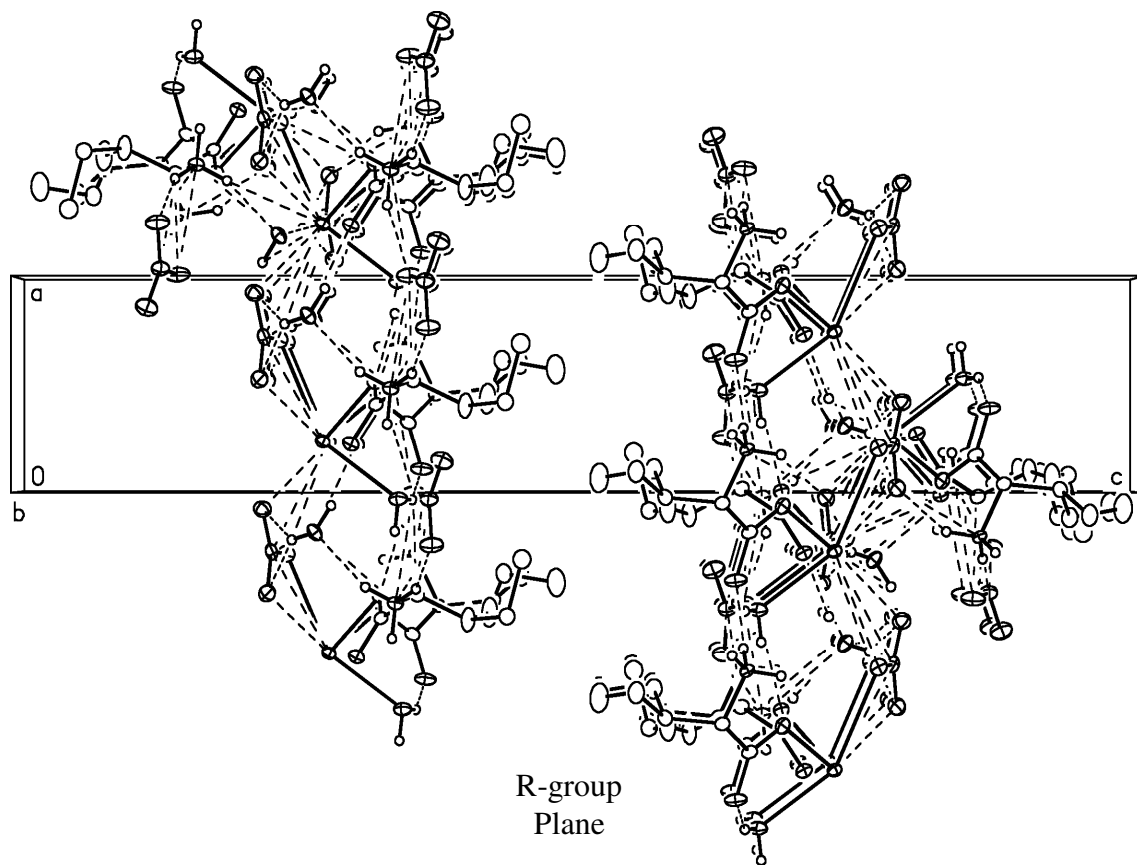


Figure 2.5: Illustration of crystal packing of Pb-IIe, showing the vertical R-group planes. View direction is parallel to the crystal *b* axis.

2.2.3 Single Crystal X-Ray Diffraction: Lead-L-Valine-L-Isoleucine

With two different amino acids coordinating to the lead centre, the lead-valine-isoleucine structure (Pb-Val-Ile), formula $[\text{Pb}(\text{OH}_2)_2(\text{L-valine})(\text{L-isoleucine})(\text{NO}_3)_2]$, is the first of this family of heteroleptic complexes. The asymmetric unit of this complex (Figure 2.6) contains one lead centre, two neutral zwitterionic L-amino acid molecules (valine and isoleucine), two water molecules and two nitrate counter ions. Within the smallest coordination sphere ($\leq 2.6 \text{ \AA}$), the lead centre has a hemidirected geometry and interacts with the oxygen atoms from the carboxylate group of the valine molecule (Pb-O20 2.379(3) \AA) and of the isoleucine molecule (Pb-O10 2.475(3) \AA) and from the one water molecule (Pb-O1 2.484(4) \AA). The hemidirected geometry is seen with the acute (bond angles between these short bonds of $75.73(11)^\circ$ (O10-Pb-O20), $80.15(12)^\circ$ (O1-Pb-O20) and $85.11(11)^\circ$ (O1-Pb-O10). Additional contacts occur in the next coordination sphere ($\leq 2.9 \text{ \AA}$), where the lead centre interacts with a second oxygen from one carboxylate group (Pb-O21 2.828(3) \AA), an additional water molecule (Pb-O2 2.886(3) \AA) and two oxygen atoms (Pb-O31 2.819(4) \AA and Pb-O32 2.827(4) \AA) from a nitrate counter anion. The coordination sphere is filled, within the sum of the van der Waals radii, with a nitrate counter ion from the adjacent asymmetric unit (Pb-O33' 2.925(4) \AA and Pb-O32' 3.126(3) \AA), forming a two dimensional chain of alternating lead atoms and nitrate counterions, and the remaining carboxylate oxygen atom from the isoleucine molecule (Pb-O11 3.463(4) \AA).

The hydrogen bonding interactions within the structure occur through the hydrogen atoms on the protonated amine functional groups and the water molecules. The amine N-H \cdots O interactions are to oxygen atoms on the nitrate anions, a water molecule and an isoleucine carboxylate group. The hydrogen atoms of the water molecules interact with oxygen atoms on carboxylate groups and a nitrate ion giving O-H \cdots O hydrogen bonding interactions.

As with the lead-isoleucine and lead-valine complexes, the R-groups of the amino acids are aligned and are directed into a “hydrophobic plane,” Figure 2.7.

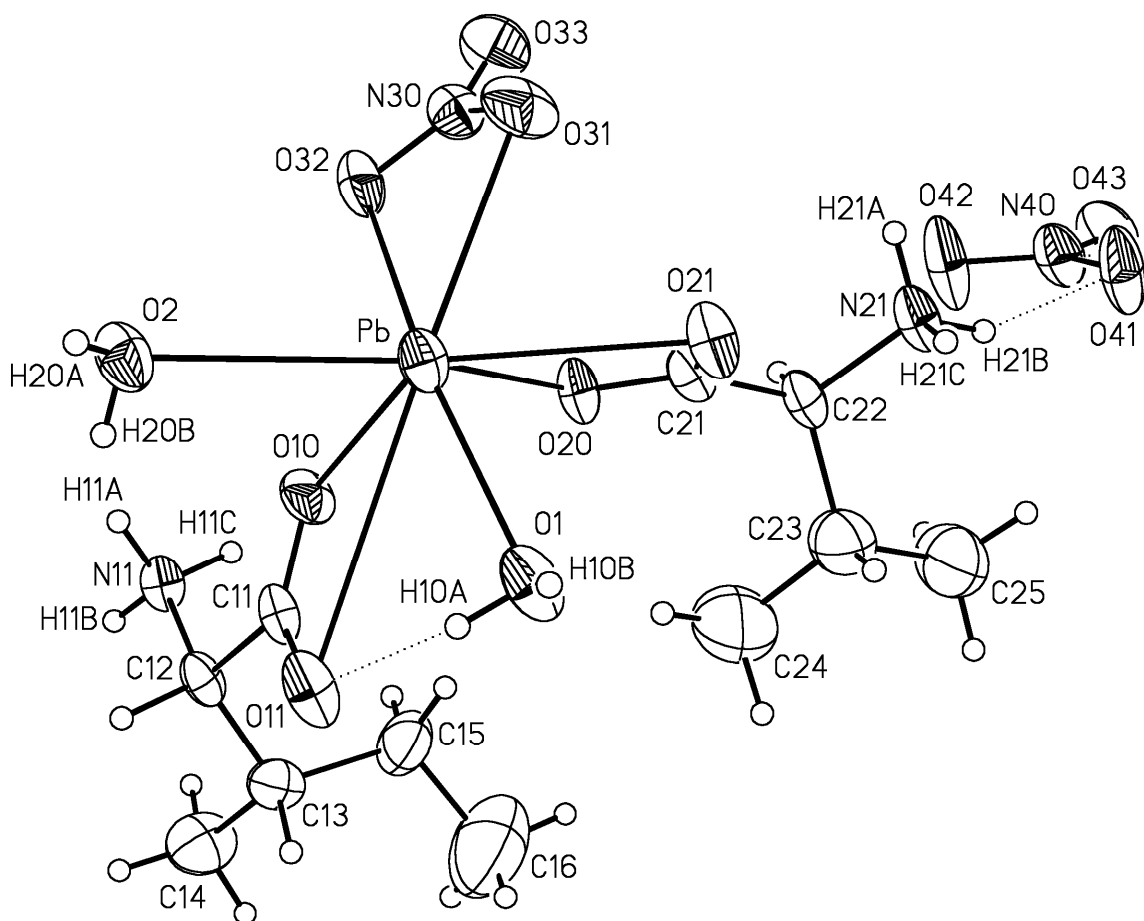


Figure 2.6: Perspective view of the asymmetric unit (unique atom set) of Pb-Val-Ile showing the atom labelling scheme. Non-hydrogen atoms are represented by Gaussian ellipsoids at the 50% probability level. Hydrogen atoms are shown with arbitrarily small thermal parameters.

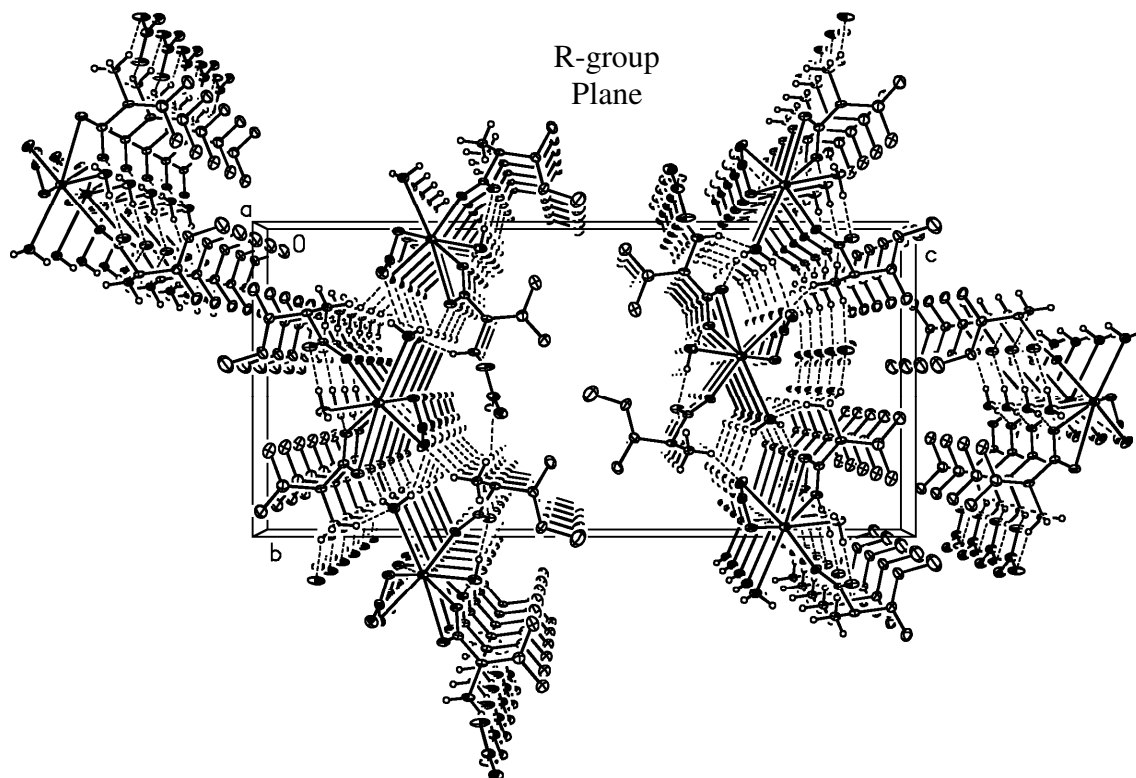


Figure 2.7: Illustration of crystal packing of Pb-Val-Ile, showing the vertical R-group planes. View direction is parallel to the crystal *a* axis.

2.2.4 Single Crystal X-Ray Diffraction: Lead-L-Phenylalanine Complexes

As with the previously discussed lead-amino acid structures, each lead-phenylalanine asymmetric unit contains one lead centre, two zwitterionic phenylalanine molecules, two nitrate counter anions and two or three water molecules (in the dihydrate and trihydrate, respectively). The formula of the dihydrate is $[\text{Pb}(\text{OH}_2)_2(\text{L-phenylalanine})_2(\text{NO}_3)] [\text{NO}_3]$ and of the trihydrate is $[\text{Pb}(\text{OH}_2)(\text{L-phenylalanine})_2] [\text{NO}_3]_2 \cdot 2\text{H}_2\text{O}$ (abbreviated Pb-Phe.2H₂O and Pb-Phe.3H₂O, respectively).

In Pb-Phe.2H₂O (Figure 2.8 a), the closest interactions with the lead centre ($\leq 2.6 \text{ \AA}$) are with an oxygen atom from the carboxylate group of each phenylalanine molecule (Pb-O20 2.343(3) \AA and Pb-O10 2.443 \AA , with a O10-Pb-O20 bond angle of 73.05(11) $^\circ$). Within the next coordination sphere ($\leq 2.9 \text{ \AA}$), four additional lead-oxygen contacts occur (two water molecules (Pb-O1 2.640(4) \AA and Pb-O2 2.871(3) \AA), a carboxylate oxygen atom (Pb-O11 2.747(3) \AA), and a nitrate counterion (Pb-O31 2.857(6) \AA)) leading to a hemidirected geometry about the lead centre. Within the sum of the van der Waals radii, the coordination sphere is filled by another carboxylate oxygen atom (Pb-O21 2.962(3) \AA), a second oxygen of the aforementioned nitrate counterion (Pb-O33 3.033(6) \AA), and a nitrate counterion from an adjacent asymmetric unit (Pb-O32' 3.016(5) \AA and Pb-O31' 3.373(3) \AA), again leading to a holodirected geometry about the lead centre and a two dimensional chain of alternating lead atoms and nitrate counter ions.

The N-H \cdots O hydrogen bonding interactions occur from the amine hydrogen atoms to the oxygen atoms of nitrate ions, a water molecule or a carboxylate group. The hydrogen atoms on the water molecules form O-H \cdots O hydrogen-bonding interactions with oxygen atoms from carboxylate groups or a nitrate ion.

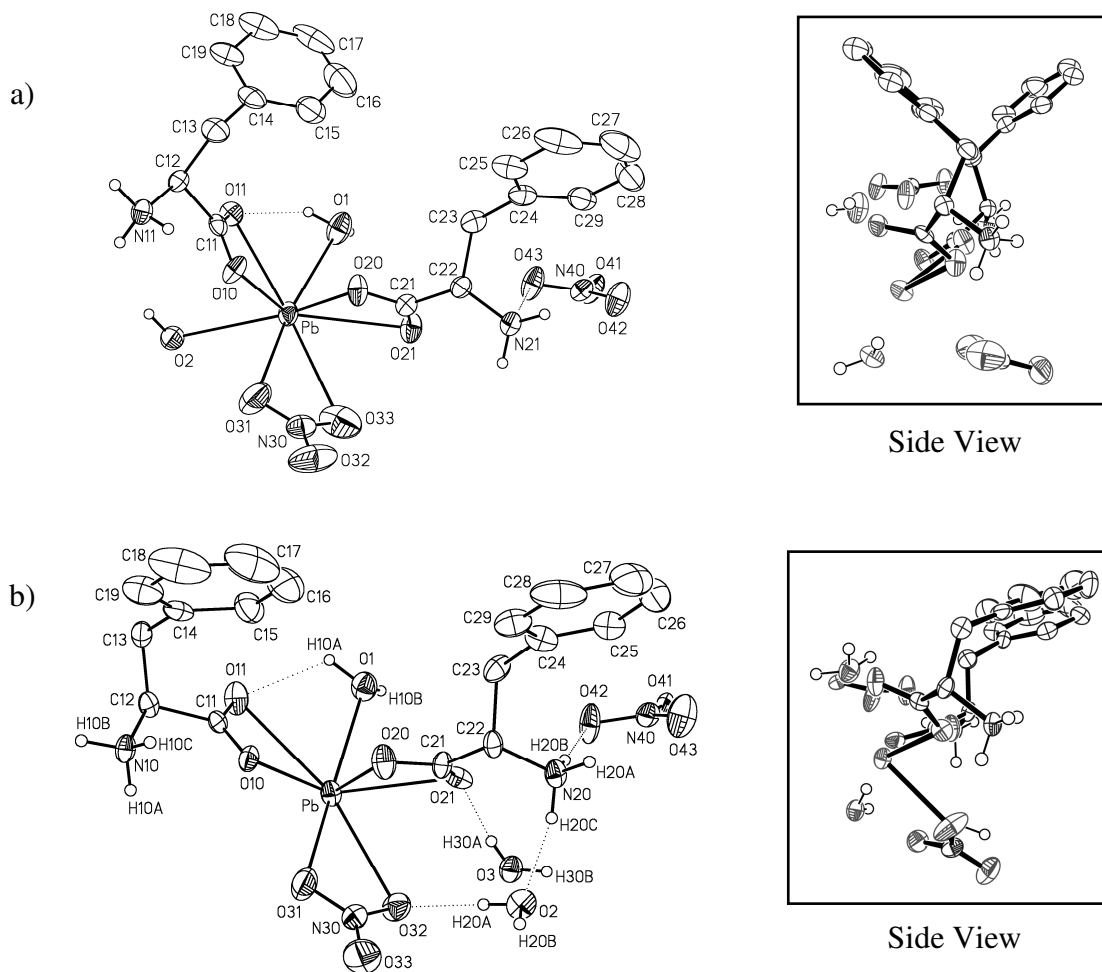


Figure 2.8: Perspective views of the asymmetric units of the lead-L-phenylalanine hydrates a) Pb-Phe.2H₂O and b) Pb-Phe.3H₂O, showing the atom labelling scheme and the position of the phenyl rings in the side view of the structures. Non-hydrogen atoms are represented by Gaussian ellipsoids at the 50% probability level. Hydrogen atoms attached to oxygen or nitrogen atoms are shown with arbitrarily small thermal parameters; all other hydrogen atoms are not shown.

The inner coordination sphere of the lead centre ($\leq 2.6 \text{ \AA}$) in Pb-Phe.3H₂O (Figure 2.8b) contains one oxygen atom from each phenylalanine carboxylate group (Pb-O10 2.380(8) \AA and Pb-O20 2.381(7) \AA , O10-Pb-O20 bond angle 74.2(3) $^\circ$). The next coordination sphere ($\leq 2.9 \text{ \AA}$) contains a contact with a nitrate counter ion (Pb-O31 2.602(8) \AA), a water molecule (Pb-O1 2.617(8) \AA), and a carboxylate oxygen (Pb-O21 2.827(7) \AA), giving a hemidirected geometry about the lead centre. And, within the sum of the van der Waals radii, the coordination sphere is completed with interactions between lead and a second oxygen from a carboxylate group (Pb-O11 2.966(8) \AA), and the oxygen atoms from two nitrate ions (one from a neighbouring asymmetric unit) (Pb-O32 2.962(8) \AA and Pb-O33" 3.325(10) \AA), forming a similar two dimensional chain to the previous lead-amino acid examples.

In the crystal structure, hydrogen bonding interactions (N-H \cdots O) occur between the protonated amine hydrogen atoms and nearby oxygen atoms of water molecules, nitrate counter ions and a carboxylate group. The hydrogen atoms of the three water molecules have O-H \cdots O hydrogen bonding interactions with: a water molecule and lead interacting nitrate; a carboxylate and lead interacting nitrate; or, an oxygen of one phenylalanine carboxylate group.

The positions in the solid state of the benzyl R-groups of the two lead-phenylalanine hydrates vary depending on the number of water molecules in the structure. The phenyl rings of the Pb-Phe.2H₂O are situated perpendicular to each other, while those of Pb-Phe.3H₂O are parallel, as seen in the side views of Figure 2.8. In both cases, the R-groups are directed into a "hydrophobic plane" in a similar fashion to the previously discussed lead-amino acid complexes, Figure 2.9.

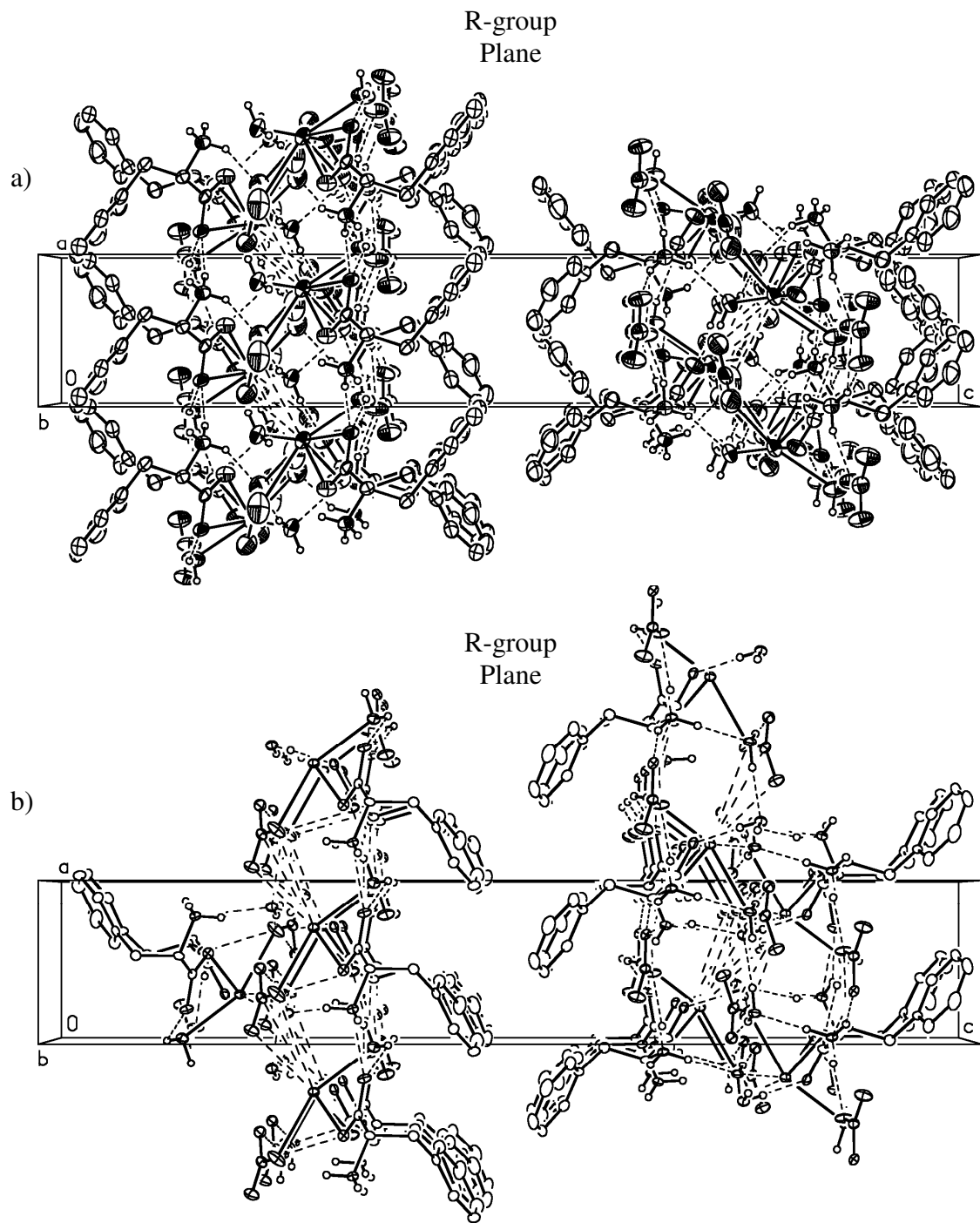


Figure 2.9: Illustration of crystal packing of a) Pb-Phe.2H₂O, and b) Pb-Phe.3H₂O, showing the vertical R-group planes. View direction is parallel to the crystal *b* axes.

Of the two lead-phenylalanine hydrates Pb-Phe.2H₂O has been consistently isolated under a variety of conditions, while Pb-Phe.3H₂O has been isolated only once. Pb-Phe.2H₂O crystallizes much more quickly than Pb-Phe.3H₂O (four days versus eleven days), and will form independently of reactant addition order, solution heating or crystallization vessel size; leading us to conclude that Pb-Phe.2H₂O is the more stable hydrate of the two.

2.2.5 Single Crystal X-Ray Diffraction: Lead-L-Arginine

The lead-arginine asymmetric unit, [Pb₂(OH₂)(L-arginine)₃(NO₃)₇]•3H₂O (referred to as Pb-HArg), contains two lead centres (denoted Pb1 and Pb2), three positively charged arginine molecules (each of which has protonated amine and guanidine groups, and a deprotonated carboxylate group), seven nitrate counter anions, and four water molecules (Figure 2.10). The Pb1 centre interacts with two positively charged arginine molecules through the carboxylate oxygen atoms while the Pb2 centre interacts with the carboxylate group of only one positively charged arginine molecule. This crystal structure is the first example of a cationic ligand coordinating to a lead centre.

For Pb1, within 2.6 Å the lead centre interacts with both oxygen atoms from the carboxylate group of one amino acid (Pb1-O11 2.518(3) Å and Pb1-O12 2.519(3) Å) and one oxygen atom from the carboxylate group of a second arginine molecule (Pb1-O22 2.401(3) Å). The acute bond angles between these shortest lead(Pb1)-oxygen bonds (O11-Pb1-O12 52.10(9)°, O11-Pb1-O22 79.04(10)° and O12-Pb1-O22 80.55(10)°) show the hemidirected geometry of the lead centre. A hemidirected geometry is also seen within the next coordination sphere (≤ 2.9 Å) with interactions between the lead centre and a fourth carboxylate oxygen atom (Pb1-O21 2.617(3) Å) and one oxygen atom on each of three nitrate counter ions (Pb1-O41 2.657(3) Å, Pb1-O61 2.803(4) Å and Pb1-O51 2.902(4) Å). The coordination sphere is filled within the sum of the van der Waals radii (Pb1-O52 3.124(5) Å, Pb1-O62 3.163(4) Å and Pb1-O42 3.312(5) Å) by the

interactions of an additional oxygen atom from each of the coordinating nitrate counter ions.

For Pb2, the inner coordination sphere (≤ 2.6 Å) contains an interaction from a carboxylate oxygen (Pb2-O31 2.494(3) Å) and a water molecule (Pb2-O1 2.576(3) Å), with an acute bond angle of $76.39(10)^\circ$ (O1-Pb2-O31). Within the next coordination sphere (≤ 2.9 Å), there are interactions between the lead centre and the second carboxylate oxygen atom (Pb2-O32 2.656(3) Å) and oxygen atoms of three nitrate counter ions (Pb2-O81 2.626(4) Å, Pb-O101 2.800(3) Å, Pb-O71 2.721(3) Å, and Pb-O72 2.803(3) Å), resulting in a hemidirected geometry at the lead centre. A holodirected geometry exists within the sum of the van der Waals radii, with interactions between the lead centre and oxygen atoms of three nitrate counter ions (Pb2-O82' 3.031(3) Å, Pb2-O91 3.133(4) Å, Pb2-O102 3.150(4) Å, and Pb2-O83 3.425(5) Å).

Hydrogen bonds of the type O-H \cdots O occur between the hydrogen atoms of the four water molecules and the oxygen atoms of a variety of groups, including a water molecule, a carboxylate functional group and five nitrate counter ions. N-H \cdots O hydrogen bonding interactions occur between the hydrogen atoms of the protonated amines and the oxygen atoms of a carboxylate group, two water molecules and three nitrate ions; and also between the hydrogen atoms of the guanidinium groups of the arginine molecule and oxygen atoms of two carboxylate groups and five nitrate counter ions.

The cationic, planar guanidinium R-groups point into an R-group plane (in a similar manner to those of the previously discussed lead-neutral amino acid structures) and interact with nitrate counter anions within this plane, Figure 2.11.

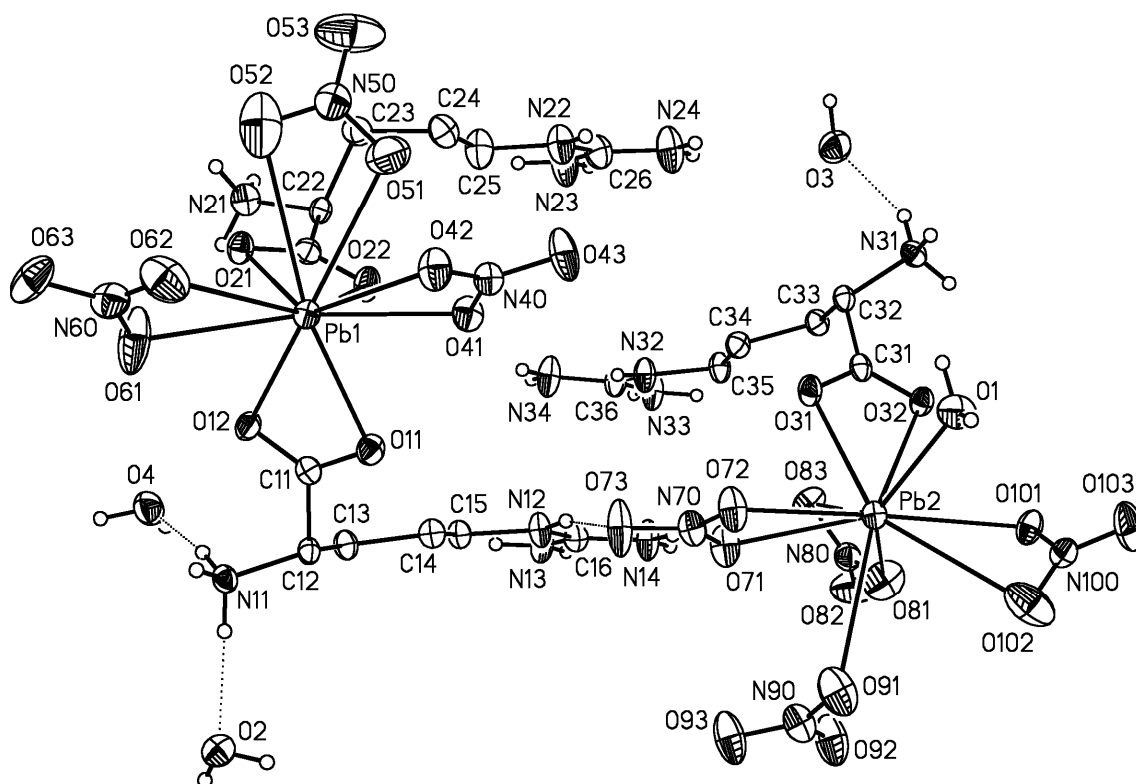


Figure 2.10: Perspective view of the asymmetric unit (unique atom set) of Pb-HArg showing the atom labelling scheme. Non-hydrogen atoms are represented by Gaussian ellipsoids at the 50% probability level. Hydrogen atoms attached to oxygen or nitrogen atoms are shown with arbitrarily small thermal parameters; all other hydrogen atoms are not shown.

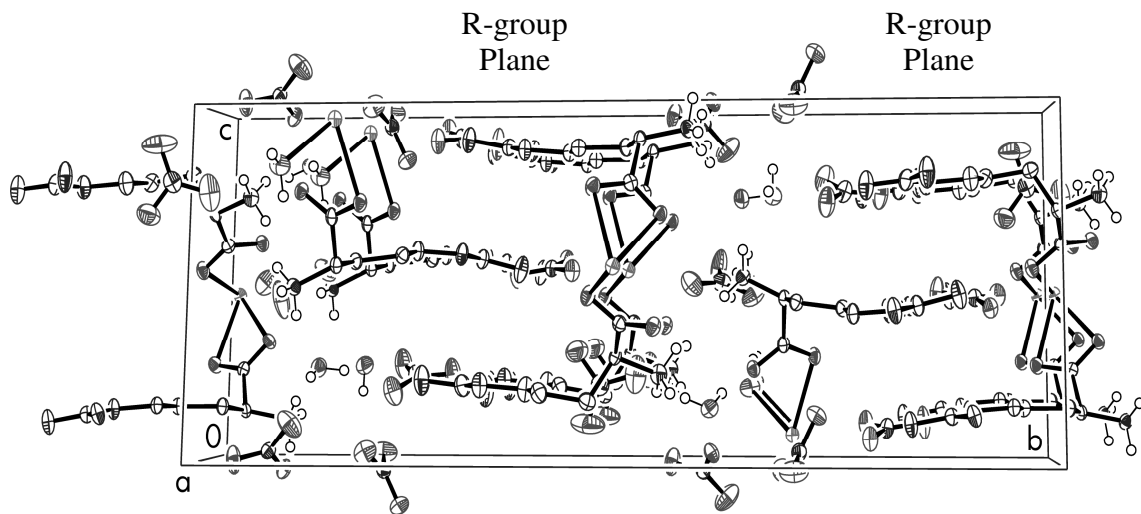


Figure 2.11: Illustration of crystal packing of Pb-HArg, showing the vertical R-group planes. View direction is parallel to the *a* axis.

2.2.6 Lead Coordination Environment: Hemidirected versus Holodirected Geometries

As described in the introduction and the preceding sections of this chapter, the geometry of the lead can be seen as either hemidirected or holodirected depending on the magnitude limitation placed upon the lead-oxygen bond lengths. For the structures described in this chapter, in all cases the lead centre can be described as both hemidirected, with the shorter lead-oxygen bond lengths on one side of the lead atom, and holodirected, with the whole coordination sphere of each lead centre filled within the sum of the van der Waals radii of the lead and oxygen atoms ($\Sigma\text{vdW Pb-O } 3.54 \text{ \AA}$). This trend is shown in Figure 2.12, where the cutoff for the coordination spheres about each lead centre increases from 2.6 \AA to 2.9 \AA to 3.5 \AA .

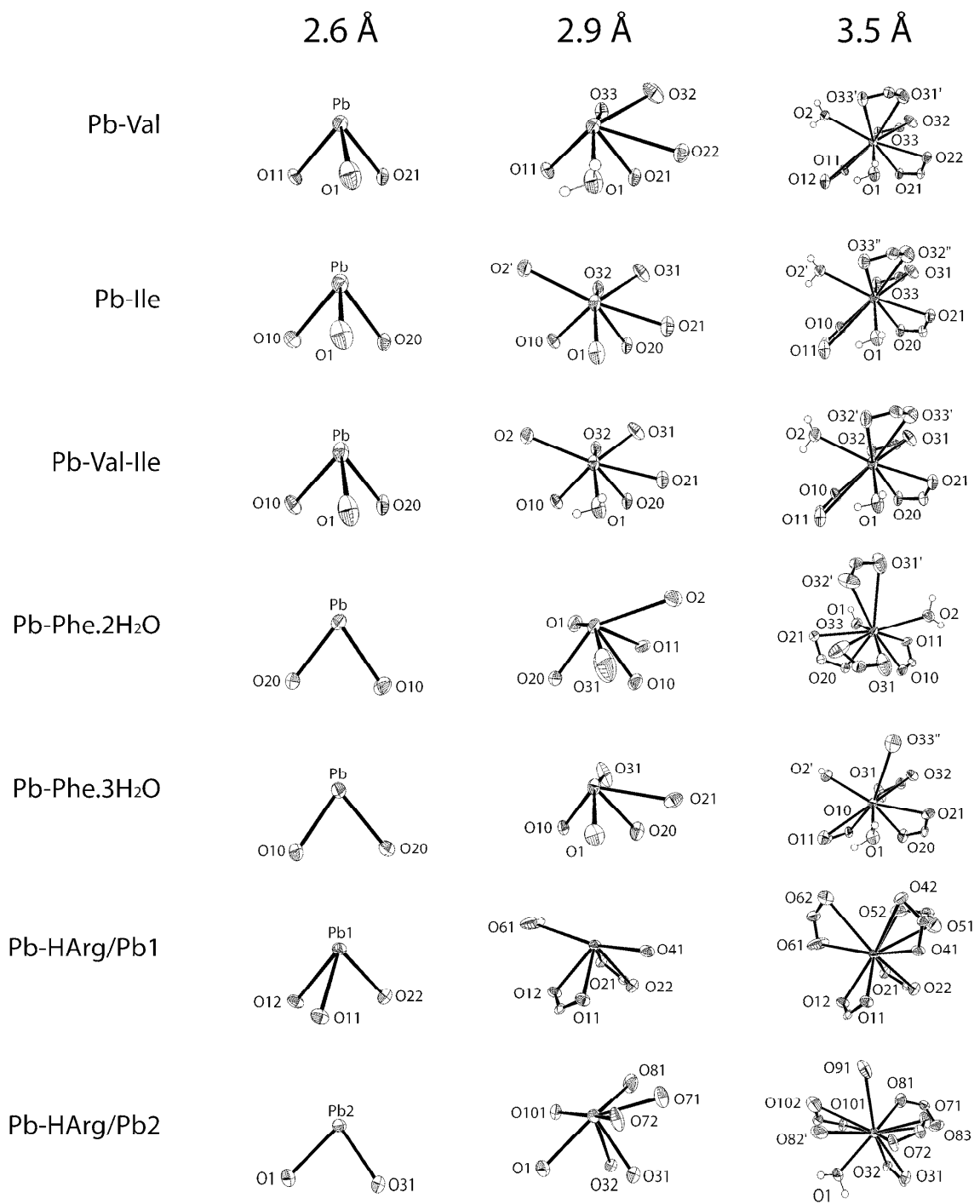


Figure 2.12: Coordination spheres about the lead centre in the six presented lead-amino acid crystal structures.

2.2.7 Lead-207 Solid State NMR Spectroscopy

In order to confirm that the analysed single crystals are representative of the bulk crystalline material, solid state carbon-13 and lead-207 CP-MAS NMR spectra were obtained. In all cases, the spectroscopic data are reproducible for crystalline samples.

The lead-207 ssNMR spectra contain isotropic shifts (and spinning side bands) for each non-symmetric lead in the asymmetric unit and for lead nitrate (which is present in some crushed crystal spectra but is not apparent in any of the crystal structure analyses). This temperature dependent lead nitrate single peak at -3490 ppm was used as an internal reference for some of the spectra. The lead-207 isotropic shifts are given in Table 2.1.

Table 2.1: Solid state lead-207 NMR data for the five lead-amino acid complexes. For Pb-HArg the lead peaks are assigned to the atoms labelled in Figure 2.10.

Structure	²⁰⁷ Pb NMR Isotropic shifts (ppm)
Pb-Val	-1707 ± 5
Pb-Ile	-1766 ± 4
Pb-Val-Ile	Not Determined
Pb-Phe.2H ₂ O	-1541 ± 5
Pb-Phe.3H ₂ O	-1541 ± 6
Pb-HArg	Pb1: -1285 ± 5
	Pb2: -2511 ± 5

The lead-207 isotropic shift for the Pb-Val-Ile structure could not be determined. Figure 2.13 is a comparison of the spectra for Pb-Val, Pb-Val-Ile and Pb-Ile crystals. The Pb-Val-Ile sample was analysed using 10 times the number of scans compared to the homoleptic structures, and using two different pulse sequence experiments (Single Pulse Excitation and Hahn echo). The resulting spectra had broad signals that, at three spinning speeds, resulted in two possible isotropic shifts one at *ca.* -1790 ppm and the other at *ca.* -1950 ppm, neither of which is conclusive. Nevertheless, in comparing the patterns of the three spectra in Figure 2.13 we can conclude that the lead centres of all three crystal structures are in similar environments, which is also evident in the X-ray crystal structures (Figure 2.2, Figure 2.4, and Figure 2.6).

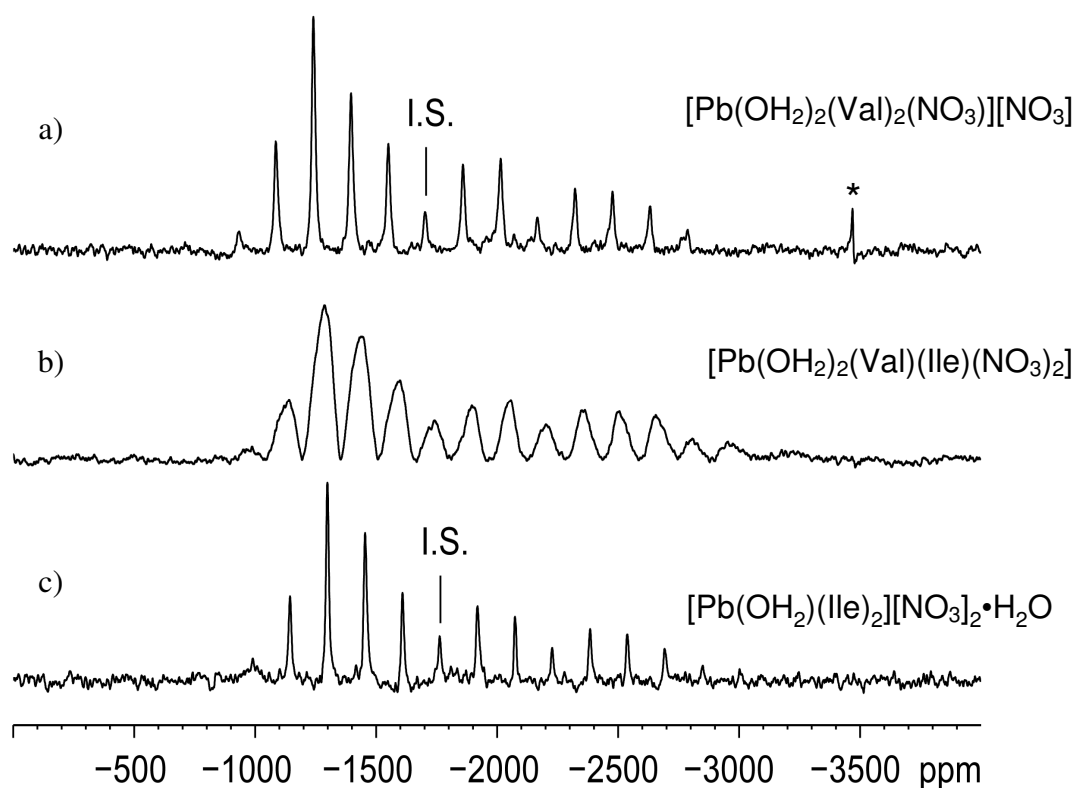


Figure 2.13: Lead-207 solid state NMR spectra of ground crystals of a) Pb-Val, b) Pb-Val-Ile, and c) Pb-Ile crystals. The isotropic shifts are marked with I.S., and the lead nitrate signal is marked with an asterisk (*).

In general, the variation of the lead-207 isotropic shifts can be explained by a downfield shift as the length of the Pb-O bonds decrease and the molecules or functional groups of the oxygen atom attachments change. At a chemical shift of -3490 ppm,⁹⁸ Pb(NO₃)₂ has the largest upfield shift of the studied compounds. The lead centre in the lead nitrate crystal structure is 12-coordinate with long Pb-O bond lengths of either 2.748 Å or 2.869 Å.⁹⁹ Comparing this lead centre to those of the lead-neutral amino acid structures (Pb-Val, Pb-Ile, Pb-Phe.2H₂O, and Pb-Phe.3H₂O), the lead-neutral amino acid structures have shorter bond lengths to oxygen atoms. With two close Pb-O_{carboxylate} interactions and one Pb-O_{water} interaction, the lead isotropic shifts of the Pb-Val and Pb-Ile are *ca.* 200 ppm upfield from those of the Pb-Phe hydrates, which have two close Pb-O_{carboxylate} interactions and no Pb-O_{water} interaction.

One of the lead centres in Pb-HArg (Pb1) has three contacts with carboxylate oxygens from two arginine molecules. This lead centre has been assigned the most downfield shift at -1285 ppm. Meanwhile the second lead centre in Pb-HArg (Pb2) has a close contact with one carboxylate oxygen of only one arginine molecule and was assigned a lead isotropic shift of -2511 ppm.

2.2.8 Carbon-13 Solid State NMR Spectroscopy

The carbon-13 ssNMR spectra of the lead-amino acid complexes are different from those of the free amino acids, and the number of carbon-13 signals is consistent with the symmetry of the crystal structure. For example, in Pb-Val each complex asymmetric unit contains pairs of non-symmetric carbon atoms in five chemically distinct environments and the ssNMR spectrum for these crystals contain seven distinct signals (Figure 2.14a), where three signals most likely result from the overlap of six non-symmetric carbon signals. Carbon-13 spectra for the lead-amino acid crystals and the corresponding amino acids are shown in Figure 2.14, Figure 2.15 and Figure 2.16.

As expected, Pb-Val-Ile complex solid state carbon-13 NMR spectrum (Figure 2.14) is similar to a combination of the lead-isoleucine and the lead-valine carbon-13 ssNMR spectra.

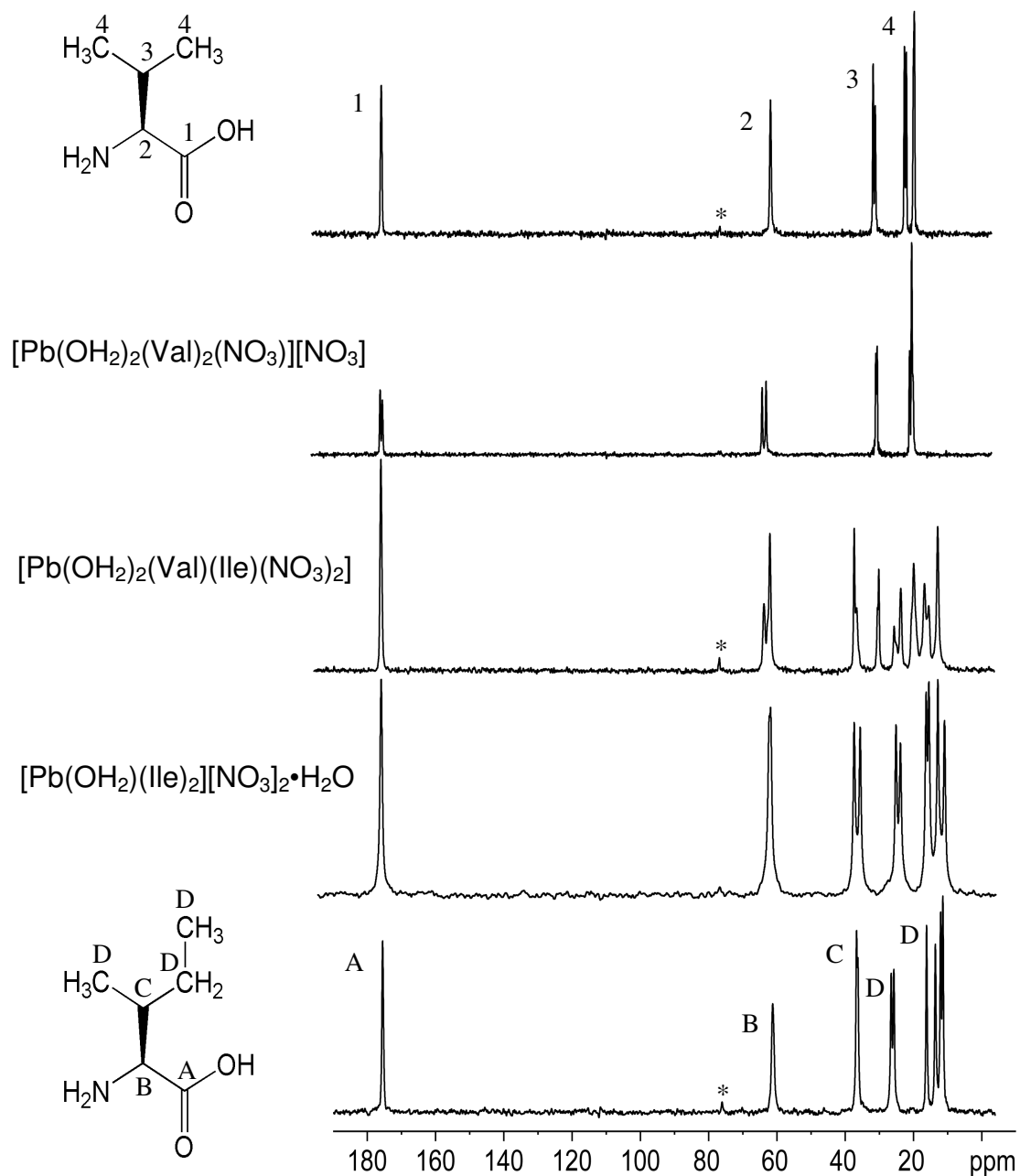


Figure 2.14: Carbon-13 ssNMR spectra of Val, Pb-Val, Pb-Val-Ile, Pb-Ile and Ile, from top to bottom, with the isotropic shifts for the amino acids labelled. Each spinning sideband is indicated with an asterisk (*)

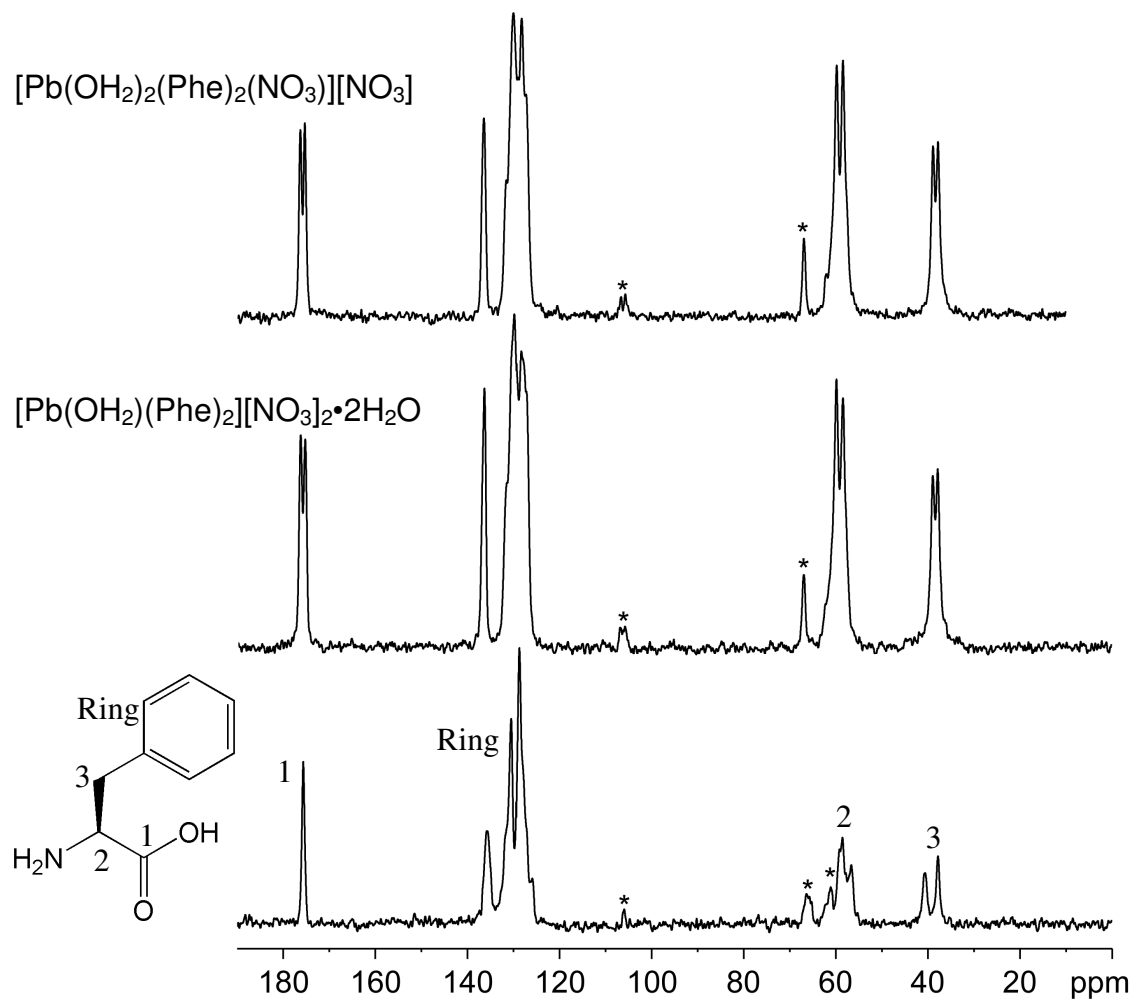


Figure 2.15: Carbon-13 ssNMR spectra of Pb-Phe.2H₂O, Pb-Phe.3H₂O and Phe, from top to bottom, with the isotropic shifts for the amino acid labelled, and each spinning sideband is marked with an asterisk (*).

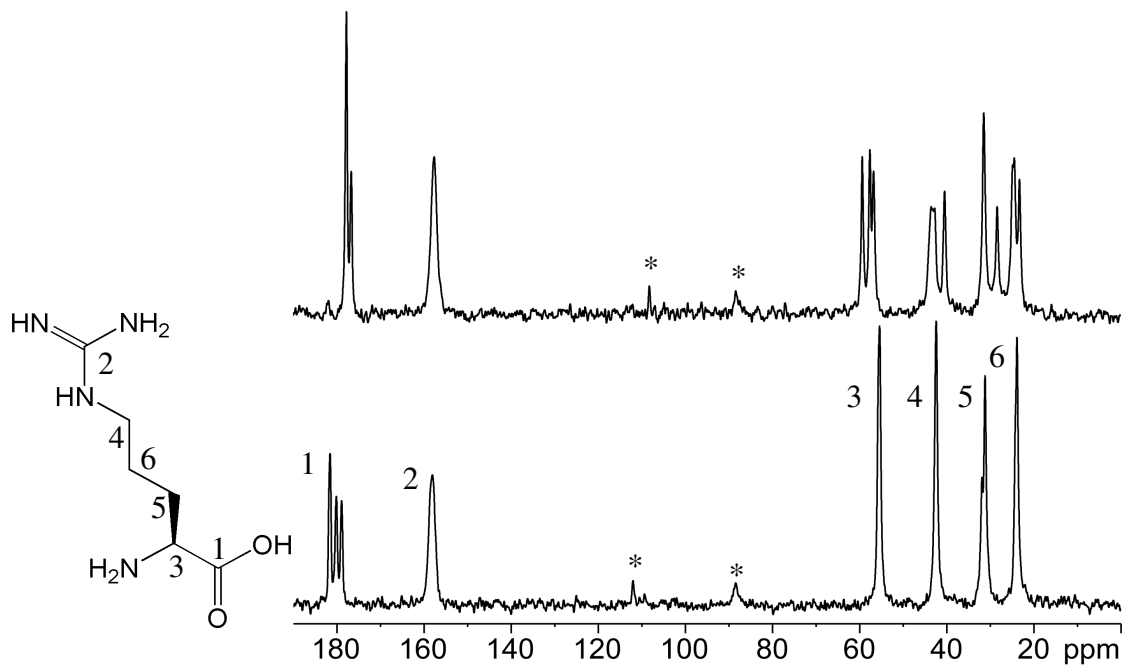
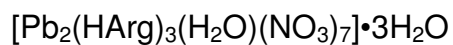


Figure 2.16: Carbon-13 ssNMR spectra of Pb-HArg (top) and Arg (bottom), with the isotropic shifts of the amino acid labelled and each spinning is sideband marked with an asterisk (*).

Solid state NMR analyses of the lead-phenylalanine complexes show identical carbon-13 and lead-207 isotropic shifts. There are three possible explanations for this similarity:

- 1) Both Pb-Phe.2H₂O and Pb-Phe.3H₂O crystallize out of solution.
- 2) Upon solvent loss, Pb-Phe.3H₂O packing changes to that of Pb-Phe.2H₂O.
- 3) The least unlikely is, the solid state carbon-13 and lead-207 chemical shifts of the two samples are identical.

Re-examination of Pb-Phe.3H₂O sample crystals 18 months after they had initially been isolated gave the unit cell of Pb-Phe.2H₂O.

In order to perform ssNMR analyses of the crystals, the samples were dried, crushed and packed into the rotors. So, loss of water molecules within the structure may have resulted in an overall structural change. The water molecules that are situated between the lead centres and nitrate ions (O2 for Pb-Phe.2H₂O, and O2 and O3 for Pb-Phe.3H₂O) are in similar positions when comparing the two structures, Figure 2.17. This change would have to be energetically small and sterically feasible, but examples of water molecule loss causing changes in lead crystal structures are known.¹⁰⁰

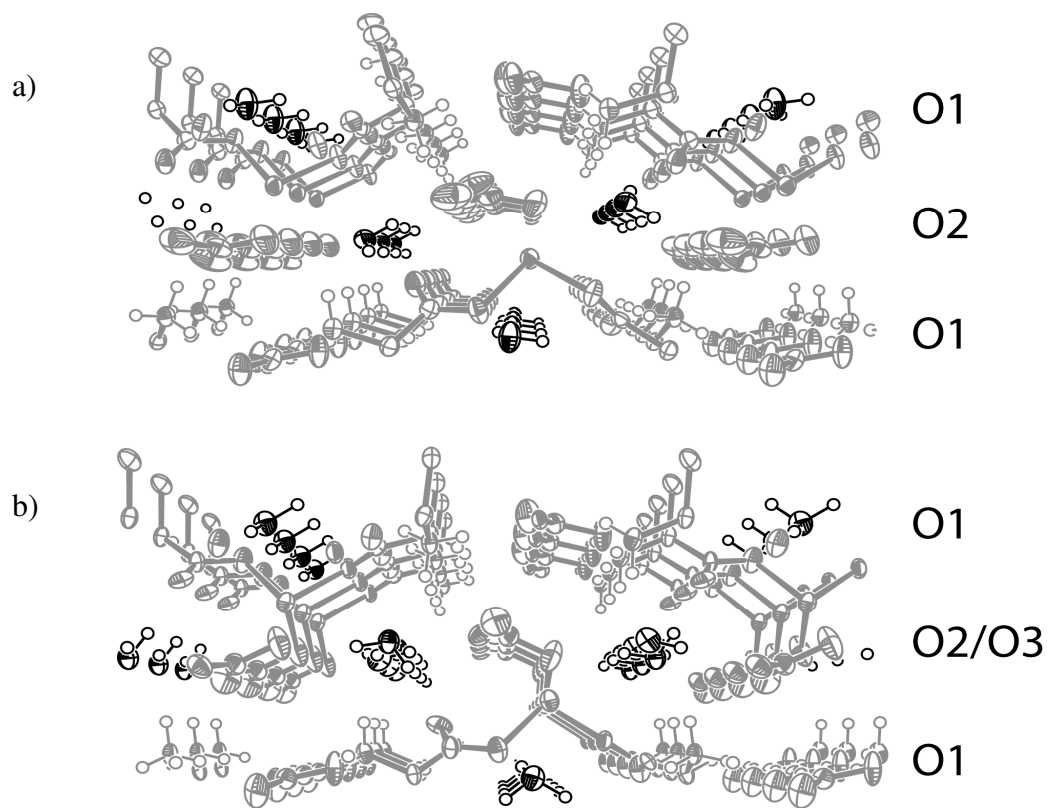


Figure 2.17: Water molecule (black) environments within the crystal structures of a) Pb-Phe.2H₂O and the b) Pb-Phe.3H₂O. The water molecule oxygen atoms in each row are labelled to the right.

2.3 RESULTS AND DISCUSSION: SOLUTION STATE CHARACTERIZATION

The lead-amino acid crystals were prepared from acidic solutions (pH *ca.* 3.3) so that the amine of the amino acid would be protonated and complexation should only occur through the deprotonated carboxylate group (Figure 2.18). In order to study the solution state chemistry of these complexes hydrogen-1, carbon-13 and lead-207 NMR analyses were performed on solutions of crystals dissolved in deuterium oxide and of reaction mixtures prepared in deuterium oxide (under a nitrogen gas atmosphere and with measured pD values).

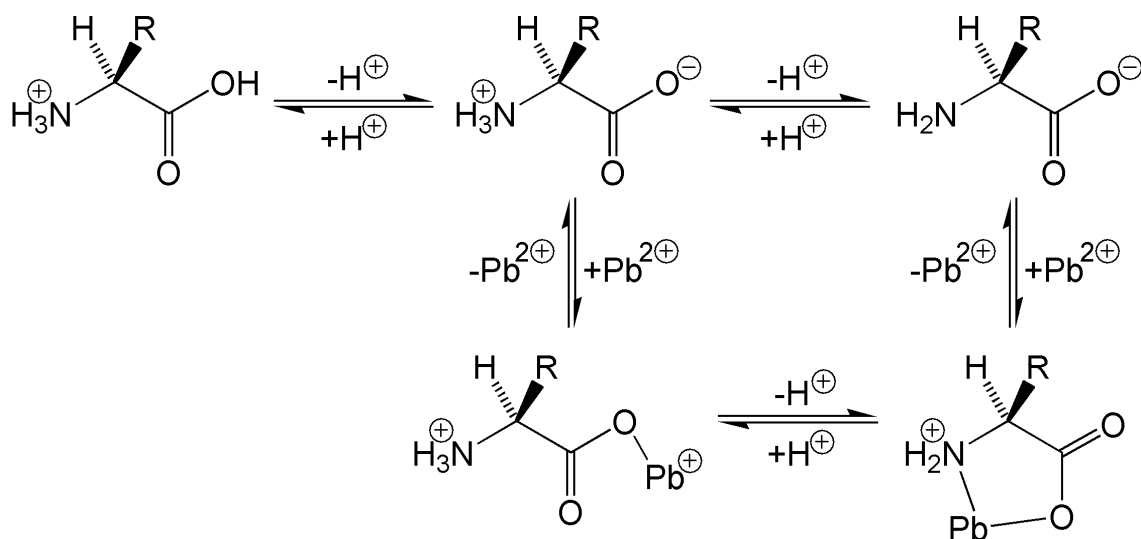


Figure 2.18: Competition equilibria between protons and lead for Lewis donating atoms on an amino acid.

2.3.1 Solution Characterization and Determination of Solution pD

In acidic lead-amino acid solutions there is a competition between lead atoms and protons for the Lewis donating atoms of the amino acid (Figure 2.18). Because of this competition, the concentration of deuterons was determined in terms of the pD of each NMR sample. In order to determine if a lead-amino acid interaction was occurring in solution at a particular pD value, lead-amino acid solutions were compared to those of the amino acid in question and also of lead nitrate (at the same pD).

pH probe calibration curves were prepared in terms of electrode potential (mV) and pD, using various concentrations of deuterium chloride in deuterium oxide. A second pH probe was used to measure the smaller volume NMR samples; this probe was referenced to the calibrated pH probe. The pD values of the smaller, referenced NMR probe are given to one decimal place, while those of the calibrated probe are given to two decimal places.

2.3.2 Lead-207 Solution NMR Spectroscopy

Lead-207 NMR analyses provided the most definitive assessment of lead-amino acid interactions in solution. Comparisons of the lead-207 chemical shifts of lead nitrate solutions at varying pD values and solutions of lead nitrate with L-valine (at varying pD values) showed a downfield shift as the pD of the solution increased. This downfield shift reached a maximum difference of *ca.* 225 ppm at pD values greater than *ca.* 3.5 (Figure 2.19).

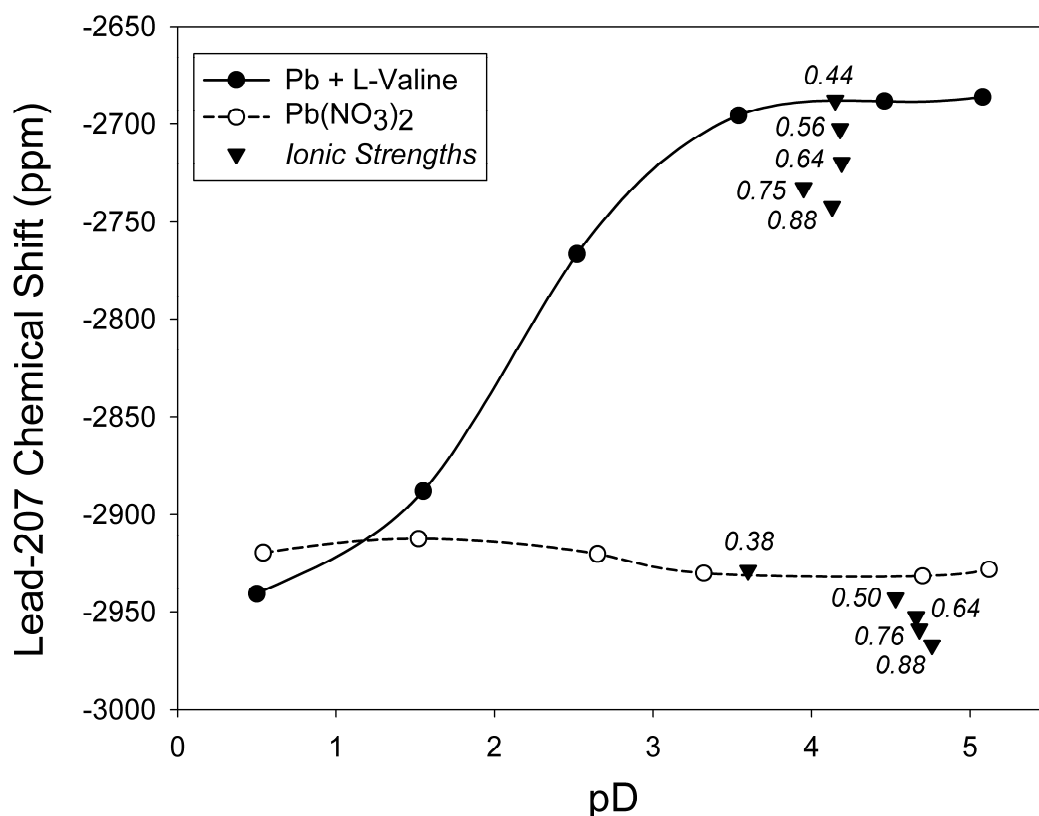


Figure 2.19: Change in lead-207 chemical shift with increasing pD values (and increasing solution ionic strength, adjusted with sodium nitrate) of a lead nitrate with Val solution (Pb + Val) and a lead nitrate solution (Pb(NO₃)₂).

Comparison the lead-207 signals of the reaction mixtures and dissolved crystals (at 0.125 M Pb) to the lead nitrate chemical shift showed a distinct downfield shift for all lead-amino acid solutions (Table 2.2). Since the pD values of both the reaction mixtures and the dissolved crystals were above pD 3.5, the concentration of lead was consistently 0.125 M in all solutions and ionic strength effects on chemical shift were minimal, the most likely explanation for the downfield shift is a difference in lead environment due to the increase in amino acid in solution. This trend was evidenced by adding increasing equivalents of L-valine to aqueous lead nitrate solutions at pH values between 4.26 and 4.44 (Figure 2.20). The environment about the lead centre is affected by an increase of L-valine concentration, which most likely increases the number of lead inner sphere interactions by valine molecules.

Table 2.2: Lead-207 chemical shifts of lead nitrate and lead-amino reaction mixtures or dissolved crystals at the given pD values and at 0.125 M concentration of lead.

Reaction Mixture or <i>Dissolved Crystals</i>	Solution pD	²⁰⁷ Pb NMR Chemical Shift (ppm)	Lead:Amino Acid Ratio
Pb(NO₃)₂	1 to 5	ca. -2925	1:0
Pb(NO ₃) ₂ + Val	4.63	-2703	1:1
<i>Pb-Val</i>	4.9	-2525	1:2
Pb(NO ₃) ₂ + Ile	4.48	-2693	1:1
<i>Pb-Ile</i>	5.0	-2474	1:2
Pb(NO ₃) ₂ + Val + Ile	4.50	-2485	1:2
<i>Pb-Val-Ile</i>	4.9	-2471	1:2
Pb(NO ₃) ₂ + Phe	4.36	-2708	1:1
<i>Pb-Phe.2H₂O</i>	4.7	-2536	1:2
<i>Pb-Phe.3H₂O</i>	4.7	-2610	1:2
Pb(NO ₃) ₂ + Arg + DNO ₃	2.78	-2819	1:1
<i>Pb-HArg</i>	4.7	-2675	1:1.5

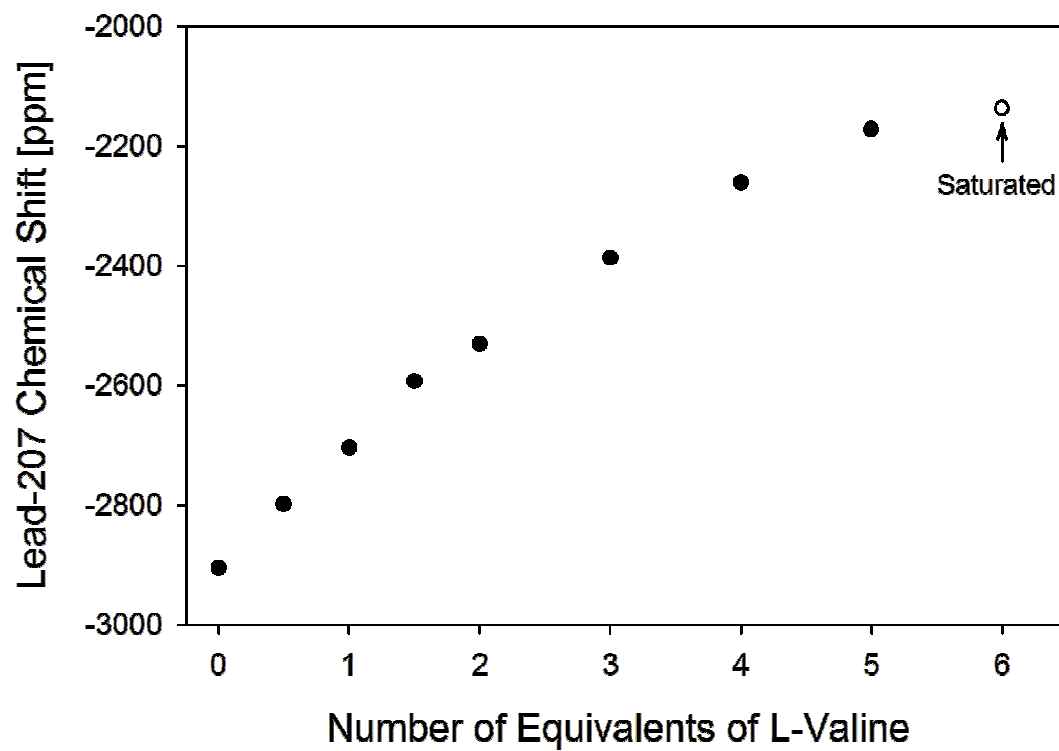


Figure 2.20: Change in lead-207 chemical shift with decreasing lead to valine ratios to the valine saturation point, which is at a ratio between 1:5 and 1:6.

2.3.3 Carbon-13 Solution NMR Spectroscopy

The carbon-13 chemical shifts of the amino acids in deuterium oxide solutions with and without lead nitrate were studied at various pD values, Figure 2.21, and with DSS as an internal standard. As the pD of the solutions increase, the chemical shift differences (for each nucleus) between the two solutions also increases. The maximum difference for both graphs is 0.7 ppm, which is found at pD values greater than *ca.* 3.5. This shift difference is not associated with differences in ionic strength (see section 2.3.5) and since the concentration, solvent, and temperature were consistent in all NMR experiments, we have concluded that the 0.7 ppm shift difference is due to the interactions of the amino acid with the lead centre and not due to the conditions of the NMR experiment.

Comparing the carbon-13 chemical shifts of the reaction mixtures and dissolved crystals shows very small chemical shift difference, Table 2.3. Increasing the concentration of amino acid in solution will affect the frequency of interactions between the amino acid and the lead centre and could affect the chemical shift of the carbon-13 centre (similarly to the lead-207 chemical shift). In these carbon spectra, however, the small chemical shift difference was deemed insignificant.

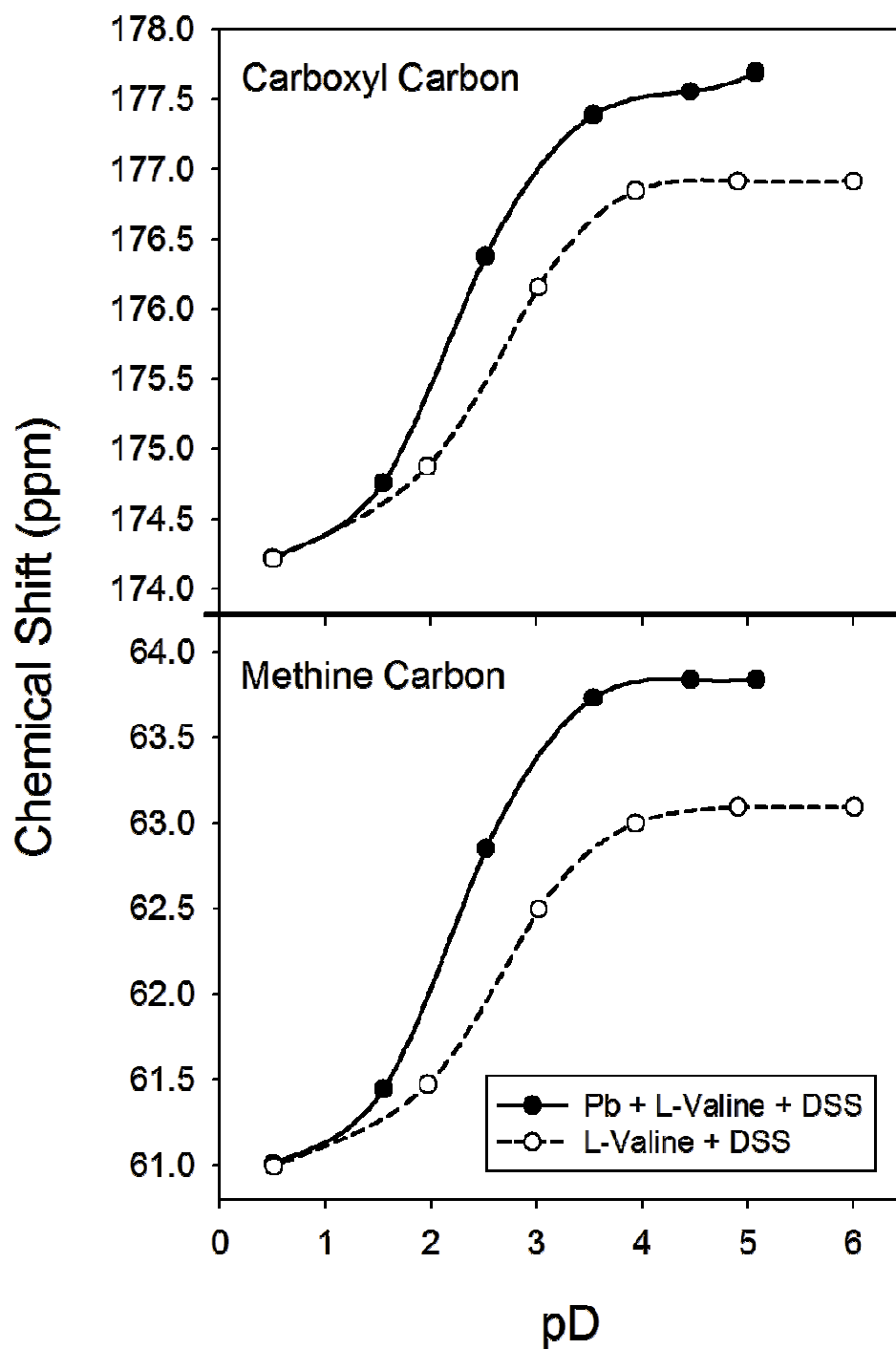


Figure 2.21: Carbon-13 chemical shifts of the carboxyl carbon (top) and the methine carbon (bottom) of an L-valine solution (Val + DSS) and a lead with Val solution (Pb + Val + DSS) at varying pD values. DSS was used as an internal standard in each case.

Table 2.3: Amino acid methine and carboxyl carbon-13 chemical shifts of amino acid solutions and lead-amino acid solutions at defined pD values and at 0.125 M concentration of amino acid.

Reaction Mixture or <i>Dissolved Crystals</i>	Solution pD	¹³ C NMR Chemical Shift (ppm)		Lead:Amino Acid Ratio
		Carboxyl Carbon	Methine Carbon	
Val + DNO ₃	4.59	177.0	63.1	0:1
Pb(NO ₃) ₂ + Val	4.63	177.6	63.8	1:1
<i>Pb-Val</i>	5.0	177.4	63.6	1:2
Ile + DNO ₃	4.44	176.9	62.2	0:1
Pb(NO ₃) ₂ + Ile	4.48	177.5	63.0	1:1
<i>Pb-Ile</i>	5.2	177.3	62.7	1:2
Val + Ile + DNO ₃	4.56	176.8 176.9	62.2 63.0	0:1:1
Pb(NO ₃) ₂ + Val + Ile	4.50	177.4 177.5	63.0 63.7	1:1:1
<i>Pb-Val-Ile</i>	4.9	177.4 177.5	63.0 63.7	1:1:1
Phe + DNO ₃	4.31	176.6	58.7	0:1
Pb(NO ₃) ₂ + Phe	4.36	177.3	59.5	1:1
<i>Pb-Phe.2H₂O</i>	5.0	177.0	59.1	1:2
<i>Pb-Phe.3H₂O</i>	4.9	177.2	59.3	1:2
Arg + DNO ₃	2.71	176.2	56.5	0:1
Pb(NO ₃) ₂ + Arg + DNO ₃	2.78	176.9	57.2	1:1
<i>Pb-HArg</i>	4.9	177.5	57.5	1:1.5

2.3.4 Hydrogen-1 Solution NMR Spectroscopy

Hydrogen-1 NMR analysis of the methine proton was not found to provide any lead-amino acid coordination information. This was most likely due to a lack of amine-lead interaction in solution. Figure 2.22 shows the curve of the chemical shift of the methine proton versus solution pD for the L-valine, and lead with L-valine deuterium oxide solutions (with DSS as an internal standard).

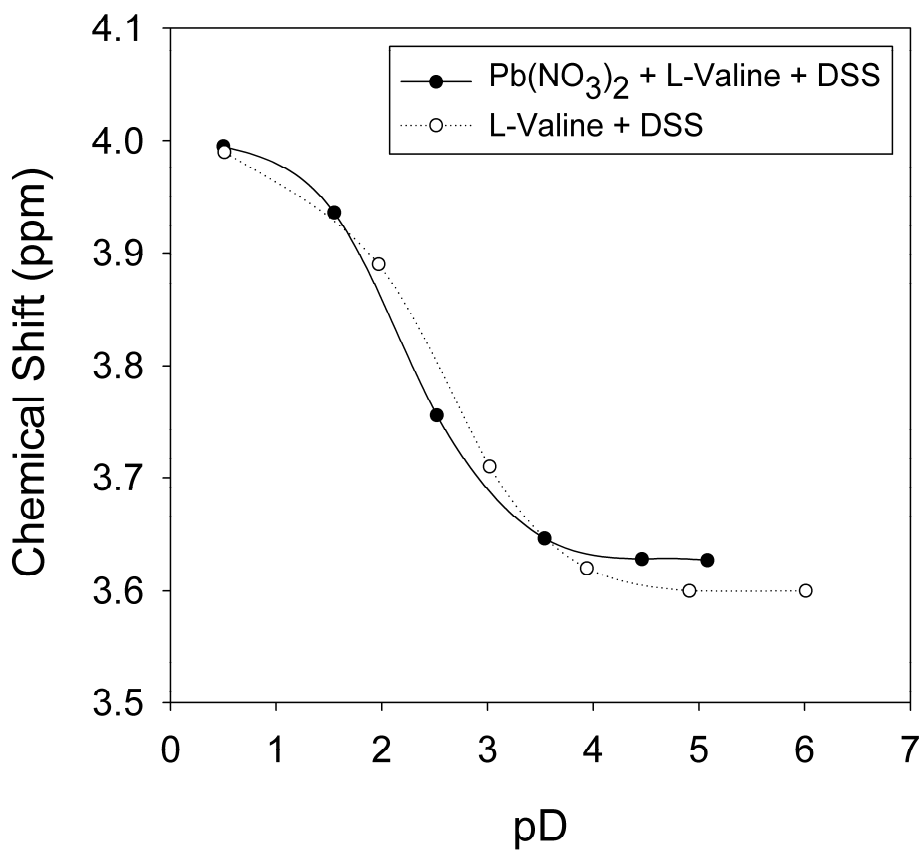


Figure 2.22: Hydrogen-1 chemical shifts of the methine proton of an L-valine solution (Val + DSS) and a lead-L-valine solution (Pb + Val + DSS) at varying pD values. DSS was used as an internal standard in each case.

2.3.5 Solution Characterization Ionic Strength Effect

Lead-valine reaction mixtures were used to determine the effects of pD and ionic strength on the studied chemical shifts. The ionic strength of each solution was adjusted with sodium nitrate. The carbon-13 and lead-207 chemical shifts were shown to be dependent on the pD of the solution. The ionic strength of the solution at pD *ca.* 4 had no significant effect on the internally calibrated carbon-13 shift ($\Delta\delta_{\text{DSS}} = 174.8 \text{ ppm}$ to 174.9 ppm), Figure 2.23. The externally calibrated lead-207 chemical shifts shifted upfield ($\Delta\delta = -54 \text{ ppm}$) with increasing ionic strength (range: 0.38 to 0.88);¹⁸ however, changes in pD had a much larger effect on the lead-207 chemical shifts (-2686 ppm at pD 5.08 compared to -2941 ppm at pD 0.50), Figure 2.19.

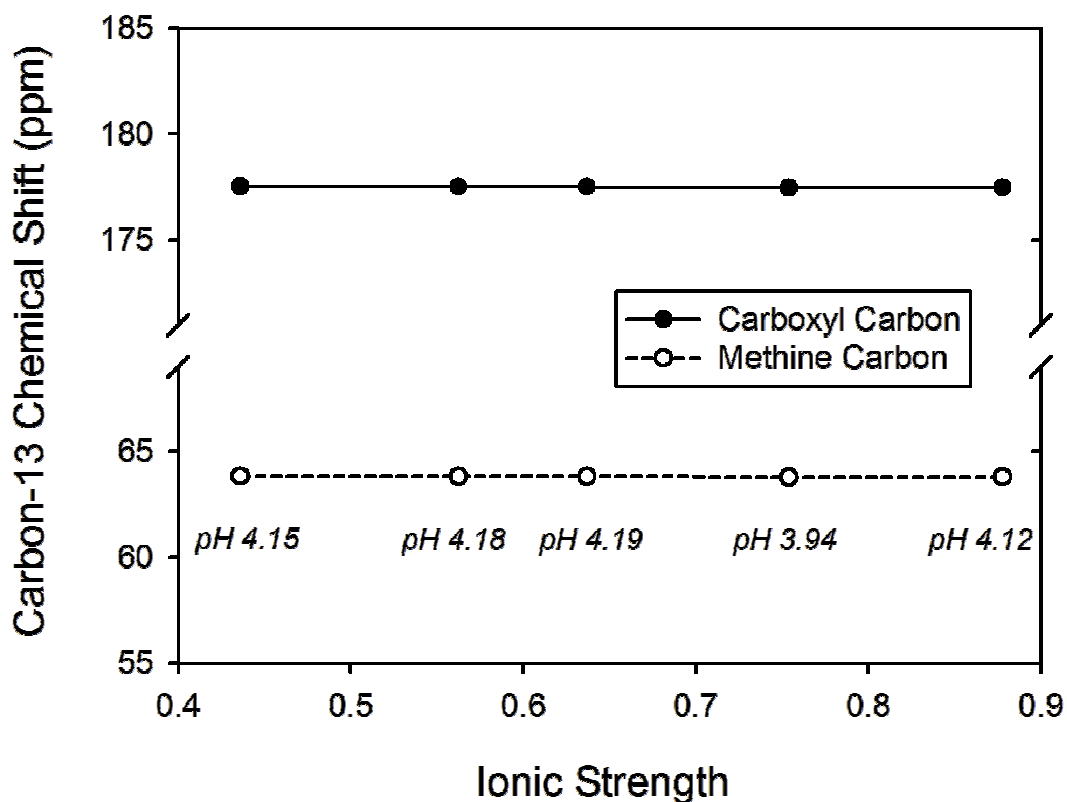


Figure 2.23: Effect of ionic strength on carbon-13 chemical shifts of the carboxyl and methine carbons of Val in five Pb + L-valine +DSS solutions

2.4 RESULTS AND DISCUSSION: GAS PHASE CHARACTERIZATION

2.4.1 ESI-MS

ESI-MS data was obtained for reaction mixtures of lead nitrate with L-valine, L-isoleucine or L-phenylalanine, for an acidified reaction mixture of lead nitrate with L-arginine, and for aqueous solutions of crystals of Pb-Val, Pb-Ile, Pb-Val-Ile, Pb-Phe.2H₂O, Pb-Phe.3H₂O, and Pb-HArg diluted in distilled water or 50% methanol/water (v/v). Peaks associated with complex ions containing both lead and the amino acid of interest are summarized in Table 2.4, the presence of these peaks is independent of flow solvent (distilled water and 50% methanol/water (v/v)) and these peaks are consistent with previously published lead-amino acid complexes, with a few additional complexes present in these newer spectra. Peak assignments have been confirmed by comparison of experimental and calculated isotope peak patterns, as well as tandem mass spectra for selected mass to charge ratios. An amino acid can hold a positive, neutral or negative charge depending on the number of protons it possesses. The complex cation formulae observed in the ESI mass spectra are considered to contain neutral amino acid ligands with a loss of -xH from the complex.

The 1:2 lead:amino acid ratios present in all five single amino acid solid state structures, as well as the 1:1 lead:arginine ratio and the 1:1:1 lead:valine:isoleucine ratio in those solid state structures are all present in the gas phase. Additional gas phase complex cations are present at larger mass to charge ratios, which may be thought of as combinations or clusters of the smaller complex cations.

Gas phase analyses of the lead-valine-isoleucine dissolved crystals and reaction mixture show the presence of complex cations with a combination of valine and/or isoleucine ligands. The variability of the lead to amino acid ratios and the presence of 1:1 lead to amino acid complexes support the theory of a 1:1 ratio of lead to amino acid in the solution state.

Table 2.4: ESI-MS peak assignments of the dissolved crystals and reaction mixtures of lead-amino acid solutions in water and 50% (v/v) methanol/water (*italicized*).

Lead-Amino Acid Sample	<i>m/z</i>	Relative Abundance*		Complex Cation Assignment [Pb ^{II} :Amino Acid] ⁺
		Dissolved Crystals	Reaction Mixture	
Pb-Val	324	L (<i>M</i>)	M (<i>H</i>)	[1:1 -H] ⁺
	463	L (<i>L</i>)	L (<i>L</i>)	[1:2 -2H +Na] ⁺
	665	L (<i>L</i>)	L (<i>L</i>)	[2:2 -2H +OH] ⁺
	764	H (<i>H</i>)	H (<i>H</i>)	[2:3 -3H] ⁺
	903	L (<i>L</i>)	V (<i>L</i>)	[2:4 -4H +Na] ⁺
	1150	V (<i>L</i>)	L (<i>L</i>)	[3:4 -4H +NO ₃] ⁺
Pb-Ile	338	M (<i>L</i>)	L (<i>L</i>)	[1:1 -H] ⁺
	491	L (<i>L</i>)	L (<i>L</i>)	[1:2 -2H +Na] ⁺
	693	L (<i>L</i>)	M (<i>M</i>)	[2:2 -2H +OH] ⁺
	804	H (<i>H</i>)	H (<i>H</i>)	[2:3 -3H] ⁺
	959	L (<i>V</i>)	V (<i>V</i>)	[2:4 -4H +Na] ⁺
	1206	V (<i>L</i>)	L (<i>L</i>)	[3:4 -4H +NO ₃] ⁺
Pb-Val-Ile (For cation assignment: [Pb:Val:Ile])	324	M (<i>M</i>)	M (<i>M</i>)	[1:1:0 -H] ⁺
	338	H (<i>H</i>)	H (<i>H</i>)	[1:0:1 -H] ⁺
	441	V (<i>V</i>)	L (<i>L</i>)	[1:2:0 -H] ⁺
	455	L (<i>M</i>)	L (<i>M</i>)	[1:1:1 -H] ⁺
	469	L (<i>H</i>)	L (<i>M</i>)	[1:0:2 -H] ⁺
	477	L (<i>V</i>)	L (<i>L</i>)	[1:1:1 -2H +Na] ⁺
	491	L (<i>L</i>)	L (<i>L</i>)	[1:0:2 -2H +Na] ⁺
	679	L (<i>L</i>)	L (<i>L</i>)	[2:1:1 -2H +OH] ⁺
	693	L (<i>L</i>)	L (<i>L</i>)	[2:0:2 -2H +OH] ⁺
	764	L (<i>V</i>)	L (<i>L</i>)	[2:3:0 -3H] ⁺
	778	L (<i>L</i>)	M (<i>M</i>)	[2:2:1 -3H] ⁺
	792	H (<i>H</i>)	H (<i>H</i>)	[2:1:2 -3H] ⁺
	806	H (<i>H</i>)	M (<i>M</i>)	[2:0:3 -3H] ⁺
	931	V (<i>V</i>)	V (<i>L</i>)	[2:2:2 -4H +Na] ⁺
	945	V (<i>L</i>)	V (<i>L</i>)	[2:1:3 -4H +Na] ⁺
	959	V (<i>V</i>)	V (<i>L</i>)	[2:0:4 -4H +Na] ⁺
1178	V (<i>L</i>)	V (<i>V</i>)	[3:2:2 -4H +NO ₃] ⁺	
1192	L (<i>L</i>)	L (<i>L</i>)	[3:1:3 -4H +NO ₃] ⁺	
1206	V (<i>L</i>)	V (<i>V</i>)	[3:0:4 -4H +NO ₃] ⁺	

Continued on the next page...

(Table 2.4 continued.)

Lead-Amino Acid Sample	<i>m/z</i>	Relative Abundance*		Complex Cation Assignment [Pb ^{II} :Amino Acid]
		Dissolved Crystals	Reaction Mixture	
Pb-Phe (For crystals: Pb-Phe.2H ₂ O/ Pb-Phe.3H ₂ O)	372	$\frac{\mathbf{H} (M)}{\mathbf{H} (H)}$	H (<i>H</i>)	[1:1 -H] ⁺
	559	$\frac{\mathbf{L} (L)}{\mathbf{L} (L)}$	V (<i>V</i>)	[1:2 -2H +Na] ⁺
	761	$\frac{\mathbf{L} (L)}{\mathbf{L} (L)}$	L (<i>L</i>)	[2:2 -2H +OH] ⁺
	908	$\frac{\mathbf{H} (H)}{\mathbf{H} (H)}$	H (<i>H</i>)	[2:3 -3H] ⁺
	1095	$\frac{\mathbf{L} (L)}{\mathbf{L} (L)}$	V (<i>V</i>)	[2:4 -4H +Na] ⁺
	1342	$\frac{\mathbf{V} (V)}{\mathbf{V} (V)}$	V (<i>V</i>)	[3:4 -4H +NO ₃] ⁺
Pb-HArg	381	M (<i>L</i>)	M (<i>M</i>)	[1:1 -H] ⁺
	555	H (<i>H</i>)	M (<i>H</i>)	[1:2 -H] ⁺
	824	V (<i>V</i>)	V (<i>V</i>)	[2:2 -2H +NO ₃] ⁺
	935	V (<i>V</i>)	V (<i>V</i>)	[2:3 -3H] ⁺

*The relative intensity ranges, as percentages of the base peak in each spectra are:
H >75%, M 35-75%, L 5-35%, V <5%.

2.6 CONCLUSIONS

Five new lead-amino acid complexes have been isolated from acidic aqueous lead-amino acid solutions and have been comprehensively characterized in the solid state, the solution state and the gas phase. In the solid state, complexes containing neutral amino acids (Val, Ile, and Phe) contain one lead(II) centre coordinated by two amino acids, while the lead and cationic arginine complex is a cluster containing two lead centres and three arginine molecules. The R-group packing within the crystal structures are similar in all of the presented complexes. The hemidirected and holodirected geometries of the lead centre are evident with increasing bonding radii. Lead-207 NMR isotropic shifts in the solid and solution states are affected by the number of amino acids interacting with the lead centre, where an increase in ligand interaction shifts the lead signal downfield. The solution state hydrogen-1, carbon-13 and lead-207 chemical shifts are strongly affected by the pD of the solution. The lead to amino acid stoichiometric ratios observed in the solid state, are also observed in the gas phase using ESI-MS. These structures compliment the six currently known lead-amino acid structures, with the first structures of two new subgroups being presented: a lead-cationic amino acid complex (Pb-HArg) and a heteroleptic lead-amino acid complex (Pb-Val-Ile).

CHAPTER 3 MERCURY-ALANINE COMPLEXES

3.1 INTRODUCTION

Two enantiomeric forms of a mercury-alanine complex have been isolated from reaction mixtures of mercurous nitrate dihydrate and alanine (L and D enantiomers, Figure 3.1).⁴⁴ The solid state structures contain mercury(I) and mercury(II) associated by alanine ligands in a polymeric array. The disproportionation of mercury(I) to mercury(II) and mercury(0) was facilitated by alanine and is evidenced by the appearance of mercury(0) in reactions of mercury(I) with the 20 common amino acids. This complex is the first mercury(I)-amino acid complex characterized in the solid state and is a unique example of an amino acid complex containing both mercury(I) and mercury(II) metal centres, enabling a direct structural and spectroscopic comparison of both coordination environments. The compounds have been comprehensively characterized using X-ray crystallography, solid state and solution state NMR spectroscopy, vibrational spectroscopies, and electrospray ionization mass-spectrometry (ESI-MS).

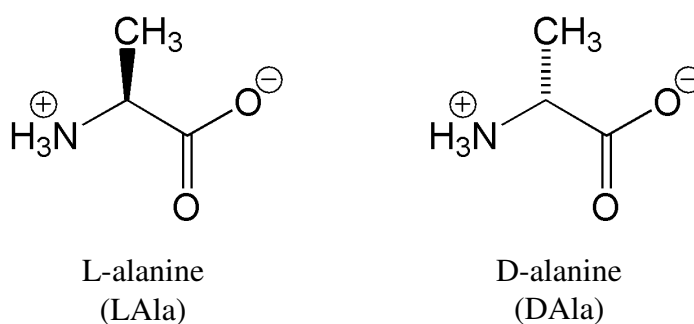


Figure 3.1: Amino acids of interest in Chapter 3.

3.2 RESULTS AND DISCUSSION: SOLID STATE CHARACTERIZATION

Appropriate conditions have been established for the crystallization of an enantiomeric pair of mercury-alanine complexes. Heated (90 °C) mixtures of L-alanine or D-alanine with mercurous nitrate in distilled water precipitate elemental mercury. Slow cooling and evaporation of these solutions gave yellow crystals that have been characterized as $[\text{Hg}_{12}(\text{Ala})_8(\text{NO}_3)_8] \cdot 2\text{H}_2\text{O}$ (denoted Hg-Ala). It has not been possible to isolate complexes using similar procedures for mixtures of mercurous nitrate with the other twenty common amino acids. However, precipitation of elemental mercury is observed in reactions with nine amino acids (alanine, arginine, asparagine, glutamic acid, glutamine, glycine, proline, serine, and threonine).

3.2.1 Single Crystal X-Ray Diffraction

The formula of the feature compound contains both mercury(I) centres and mercury(II) centres resulting from a disproportionation of mercurous ions to mercury(0) and mercury(II), consistent with the established effect of Lewis bases on mercury(I) (as discussed in Section 1.4.1 and Section 1.5.2).^{96;101} In the solid state, the asymmetric unit is composed of $[\text{Hg}_{12}(\text{Ala})_8(\text{NO}_3)_8] \cdot 2\text{H}_2\text{O}$, where each alanine can be considered as an anion. The asymmetric unit associates into a polymeric chain of alternating mercury(I) pair-alanine and mercury(II)-alanine units, so that the monomeric unit consists of $[\text{Hg}^{\text{I}}_2\text{Hg}^{\text{II}}(\text{Ala})_2(\text{NO}_3)_2]$, as shown in Figure 3.2.

Pairs of mercury(I) centres interact with the oxygen atoms in the carboxylate groups as well as in four nitrate counter ions. The eight mercury(I) atoms have coordination numbers of three (1), four (3), five (3) and six (1) (number of mercury atoms with a specific coordination number is in brackets). Mercury(I) dimers are coordinated by oxygen atoms from alanine carboxylate groups and nitrate counter ions. Hg-Hg-O (carboxylate) bond angles range from 158.4° to 174.1°. This near-linearity of the Hg-Hg-O moiety is present in the few other reported mercury(I)-carboxylate structures (166.6° to 177.9°) (Table 3.1).^{37-40;102;103} A close contact (3.0552(9) Å) between two mercury(I) atoms is responsible for the association of adjacent mercury(I) dimers

(between Hg1 and Hg5 in Figure 3.2, *cf.* sum of the covalent radii,²¹ 2.54 Å; sum of the van der Waals radii,¹⁰⁴ 4.1 Å). Mercury is known to form both neutral and ionic clusters, where Hg-Hg bond distances vary between 2.66 Å and 3.85 Å.¹⁰⁵⁻¹⁰⁸ In the featured compound, four Hg···Hg interdimer distances fall within this range.

All four mercury(II) centres are eight coordinate, involving interactions with the amino and carboxylate moieties of two alanine ligands and the oxygen atoms of two nitrate counter ions. Within the inner coordination sphere, nitrogen atoms of the alanine ligands adopt a *trans* configuration about the mercury(II) centres (N-Hg-N 168.4° to 175.1°). Carboxylate oxygen atoms are in a *cis* configuration about the mercury(II) centres with O-Hg-O angles between 62.6° and 71.0°. The mercury(II) atoms are chelated in a κ^2 fashion by each of two alanine molecules through Hg-N and Hg-O interactions, with typical Hg-N distances and slightly longer than expected Hg-O distances (Table 3.1). The N-Hg-O bond angle for each alanine ligand ranges between 62.4° and 66.2°. The near linear N-Hg-N bond angles and shorter Hg-N bond distances than Hg-O bond distances emphasize the bonding preference of mercury(II) for nitrogen donors over oxygen donors.⁴¹

The mercury(II) coordination environment (ii) can be compared to the previously reported structure of methylmercury-alanine.^{42;43} In this structure a mercury(II) centre is chelated by one alanine ligand (i) with an almost linear N-Hg-C bond angle (173(1)°), a N-Hg bond distance of 2.10(3) Å and a N-Hg-O bond angle of 58.6(7)°. In contrast, the mercury(II) centres in [Hg₁₂(Ala)₈(NO₃)₈] \cdot 2H₂O each accommodate two chelating alanine ligands (ii) with near linear N-Hg-N bond angles, yet the Hg-N bond lengths are similar between the two structures.

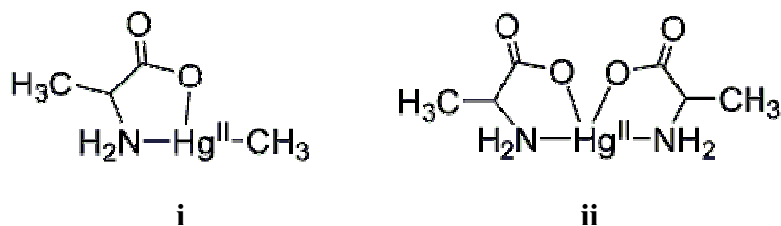


Table 3.1: Interatomic distance ranges in $[\text{Hg}_{12}(\text{Ala})_8(\text{NO}_3)_8]\cdot 2\text{H}_2\text{O}$

Bond	Hg-LAla [Å]	Hg-DAla [Å]	Typical Ranges (Ref.)
$\text{Hg}^{\text{I}}-\text{Hg}^{\text{I}}$	2.5033(9)-2.5233(9); 3.0552(9) [†]	2.5045(5)-2.5233(5) 3.0558(6) [†]	2.50-2.52 (37-40)
$\text{Hg}^{\text{I}}-\text{O}$ (Ala)	2.122(9)-2.225(11)	2.145(6)-2.216(6)	2.09-2.15 (37-40)
$\text{Hg}^{\text{I}}-\text{O}$ (nitrate)	2.430(10) - 3.060(14)	2.433(7)-3.030(9)	2.46-2.96 (109)
$\text{Hg}^{\text{II}}-\text{N}$	2.085(12)-2.125(12)	2.093(8)-2.115(8)	2.07-2.29 (42;43;55;110;111)
$\text{Hg}^{\text{II}}-\text{O}$ (alanine)	2.760(11) - 2.865(9)	2.765(7)-2.862(6)	2.62-2.72 (42;43;55)
$\text{Hg}^{\text{II}}-\text{O}$ (nitrate)	2.645(10) - 2.921(12)	2.653(6)-2.909(8)	2.59-2.77 (112)

[†] Closest contact between independent Hg_2^{2+} units.

The coordination spheres of the mercury(I) and mercury(II) atoms are completed by the nitrate counter ions, in which the Hg-O bond lengths are within the typical ranges (Table 3.1).^{42;43;55;109-112} Each of the two water molecules present in the asymmetric unit is hydrogen bonded with the amine moiety of one alanine molecule (1.82-1.87 Å) and with the oxygen atoms of two nitrate counter ions from the neighbouring asymmetric unit (1.81-2.52 Å), Figure 3.3.

At distances of 3.0552(9) Å for Hg-LAla and 3.0558(6) Å for Hg-DAla, there is, within each structure, a close contact between two mercury(I) atoms of adjacent dimeric clusters (between Hg1 and Hg5 in Figure 3.2) which is beyond the sum of the covalent radii (2.54 Å). For Hg-LAla, bond angles at the joining mercury atoms are 92.67° (Hg2-Hg1-Hg5) and 99.33° (Hg6-Hg5-Hg1), and the torsion angle is -58.96° (Hg2-Hg1-Hg5-Hg6). For Hg-DAla, bond angles at the joining mercury atoms are 92.64° (Hg2-Hg1-Hg5) and 99.33° (Hg6-Hg5-Hg1), and the torsion angle is 58.96° (Hg5-Hg6-Hg3-Hg4).

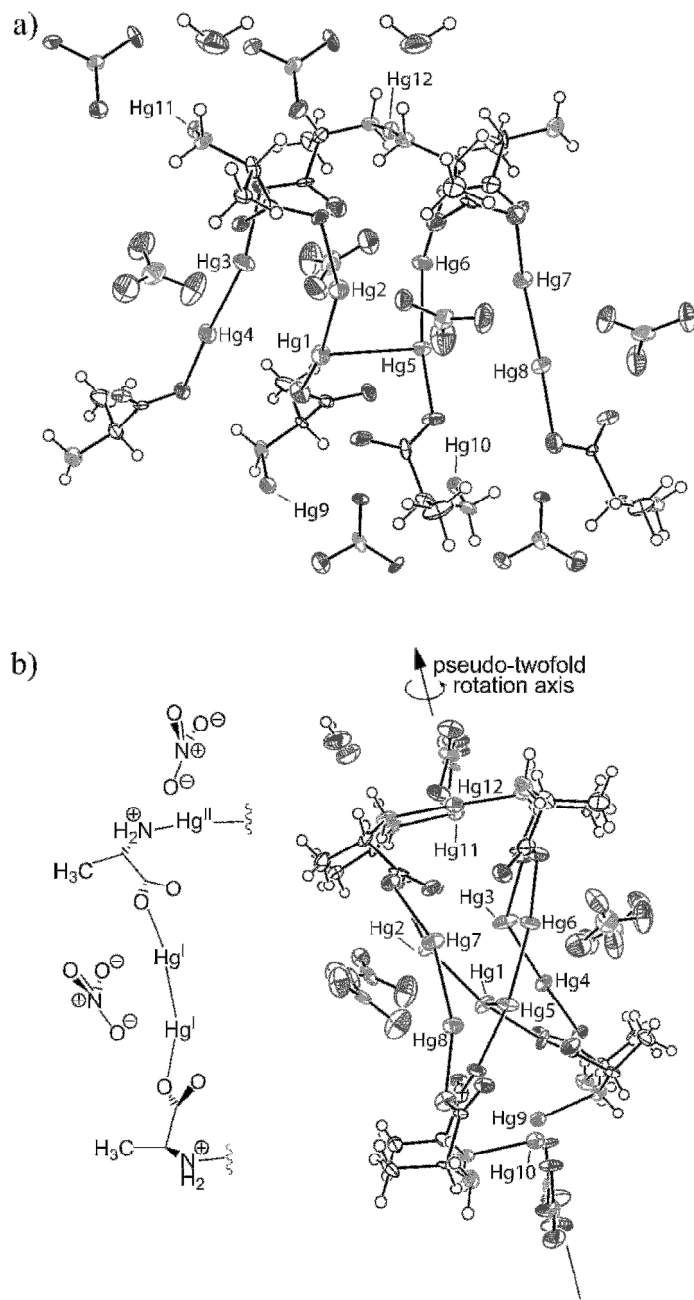


Figure 3.2: Asymmetric unit of Hg-LAla with calculated positions for hydrogen atoms, a) viewed along the crystal *b* axis and b) viewed along the crystal *a* axis – for clarity, only the shortest covalent bonds are indicated.⁴⁴ The diagram on the left in b) shows the connectivity of the monomeric unit. Thermal ellipsoids are shown at 50% probability except for the hydrogen atoms which are shown as small spheres of arbitrary size.

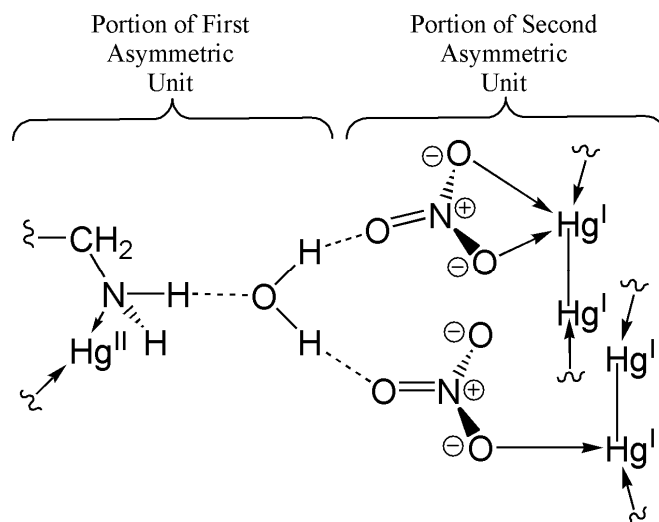


Figure 3.3: Hydrogen bonding of one water molecule between two Hg-Ala asymmetric units.⁴⁴

Extended views of the asymmetric unit (Figure 3.4) show another interesting feature: the twisted ladder arrangement of the mercury(I) dimers. From the front view (Figure 3.4a), a ladder type arrangement of the mercury(I) clusters is observed. Additionally, the side view (Figure 3.4b) shows the positioning of the mercury(I) clusters which result in a W-shape. The torsion angles between the points in the W-shape from the nearest atoms to the furthest atoms (Figure 3.4b) are -32.46° (Hg8-Hg7-Hg2-Hg1), -58.96° (Hg6-Hg5-Hg1-Hg2), and -48.98° (Hg1-Hg5-Hg3-Hg4), respectively. Comparing the two enantiomers, the negative torsion angles in Hg-LAla are expected to be equal in magnitude but opposite sign to those of Hg-DAla, 32.45° (Hg8-Hg7-Hg2-Hg1), 58.96° (Hg6-Hg5-Hg1-Hg2), and 48.96° (Hg5-Hg6-Hg3-Hg4).

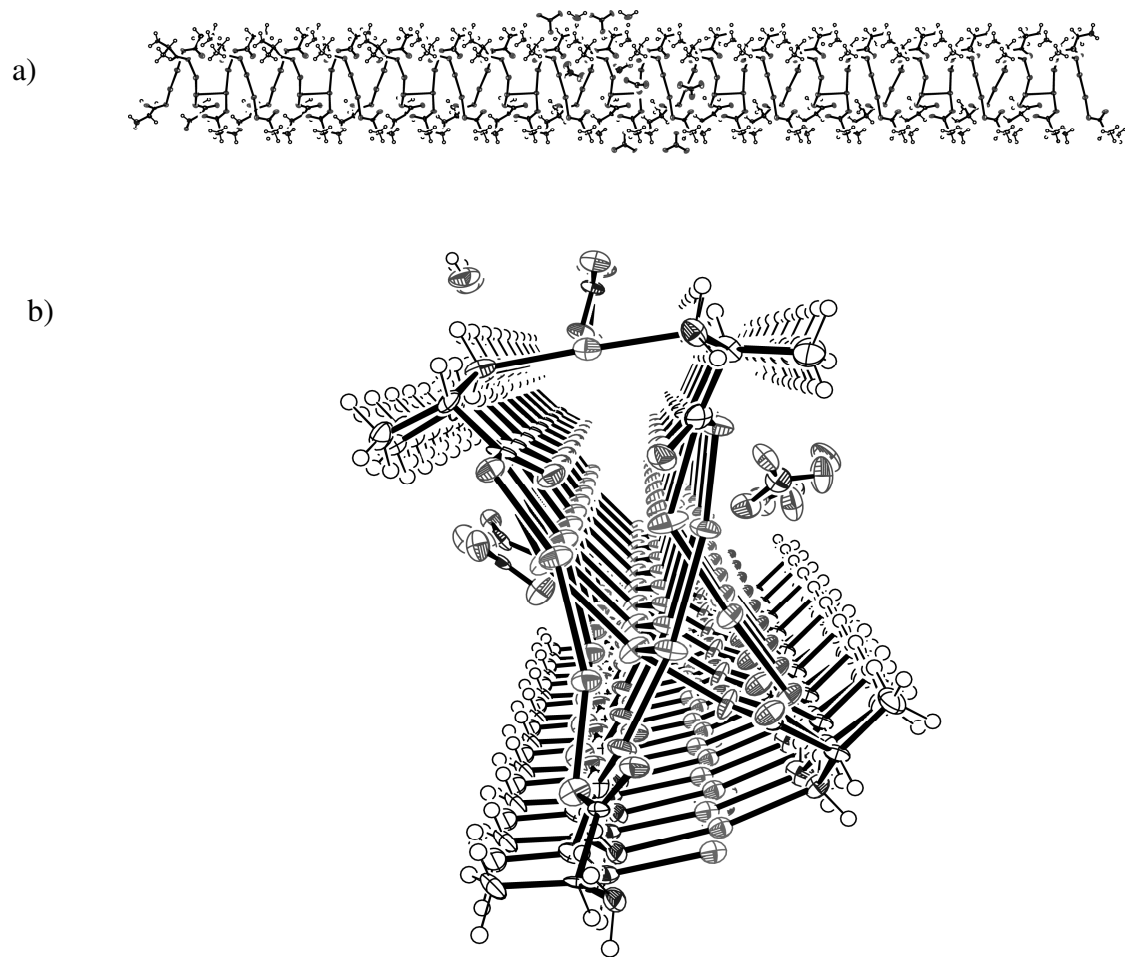


Figure 3.4: Extended view of the Hg-LAla asymmetric unit, a) viewed parallel to the crystal *b* axis and b) viewed parallel to the crystal *a* axis.

3.2.2 Solid State NMR Spectroscopy

Solid state ^{13}C CP-MAS NMR spectra for crystalline samples of Hg-LAla and Hg-DAla are shown in Figure 3.5 and detailed in Table 3.2. In all cases, the spectroscopic data are reproducible for crystalline samples, are consistent for both isomers, and are distinct from those of the alanine crystals. The presence of water molecules perturbs the two-fold (C_2) symmetry in the asymmetric unit of Hg-Ala, (shown in Figure 3.2b). This results in four different pairs of ‘equivalent’ alanine ligands corresponding to four signals observed in the solid state ^{13}C NMR spectra (Figure 3.5). Poor resolution of the signals corresponding to the amine carbon centre (C2) is due to ^{14}N quadrupolar broadening, however, the asymmetry of the peak indicates distinct broadened resonances. Due to the dangers involved with using the methylmercury standard, mercury-199 ssNMR analysis was not performed.

Table 3.2: Solid state carbon-13 NMR chemical shifts (ppm) for crystals of Hg-LAla, Hg-DAla, and L-alanine.⁴⁴

Hg-LAla	Hg-DAla	L-alanine	Assignment
181.3	181.2		
180.3	180.2	177.5	C(O)
179.2	179.2		
178.6	178.6		
57.0 (broad)	57.0 (broad)	50.6	C(N)
23.2	23.1		
22.0	22.0	20.1	CH ₃
21.5	21.3		
21.0	21.0		

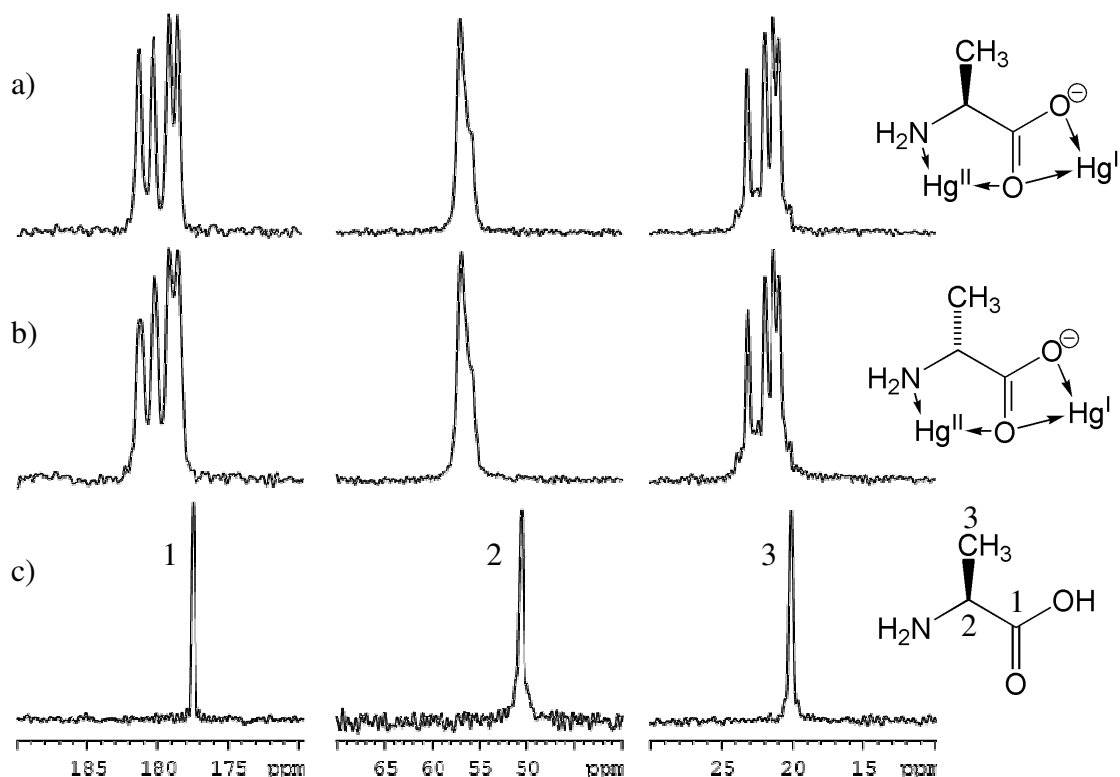


Figure 3.5: Carbon-13 ssNMR signals for a) Hg-LAla, b) Hg-DAla, and c) L-alanine crystals.⁴⁴

3.2.3 IR Spectroscopy and Raman Spectroscopy

The IR and Raman spectra for crystals of Hg-LAla and Hg-DAla are consistent with those reported for the methylmercury-alanine complex (see Appendix A Table A.1).⁴³ Mercury-nitrogen IR stretching modes were assigned to the peaks at 525 cm^{-1} and 553 cm^{-1} (Hg-LAla) or 526 cm^{-1} and 557 cm^{-1} (Hg-DAla). The strong Raman mercury-mercury stretch of 160 cm^{-1} (Hg-LAla) or 159 cm^{-1} (Hg-DAla) were consistent with those previously reported for solvated mercury(I) ions (160 cm^{-1} to 172 cm^{-1}).⁹⁶

3.3 RESULTS AND DISCUSSION: SOLUTION STATE CHARACTERIZATION

3.3.1 Solution Characterization

Solutions of the reaction mixtures and the dissolved crystals can potentially be analysed using hydrogen-1, carbon-13, and mercury-199 NMR spectroscopy. Ideally, mercury-199 NMR analysis would be used to show a mercury-alanine interaction in the solution state. Unfortunately, we were not able to detect a mercury-199 signal for mercury(I) or for mercury(II). This was most likely due to the large chemical shift range of the mercury-199 nucleus and the expected broad signal of the mercury(I) centre.⁸³

Instead, carbon-13 and hydrogen-1 were used to assess the mercury-amino acid interaction in solution, Figure 3.6. Coordination through the carboxylate oxygen should be detected through the two bond coupling of the carboxylate carbon to mercury (${}^2J_{\text{CHg}}$), rather than the four bond coupling from the methine proton to mercury (${}^4J_{\text{HHg}}$). Similarly, coordination through the nitrogen should be detected through three bond coupling of the methine hydrogen to mercury (${}^3J_{\text{HHg}}$). The chemical shift of the methine carbon would potentially be affected by both mercury-amine (${}^2J_{\text{CHg}}$) and mercury-carboxylate (${}^3J_{\text{CHg}}$) interactions.

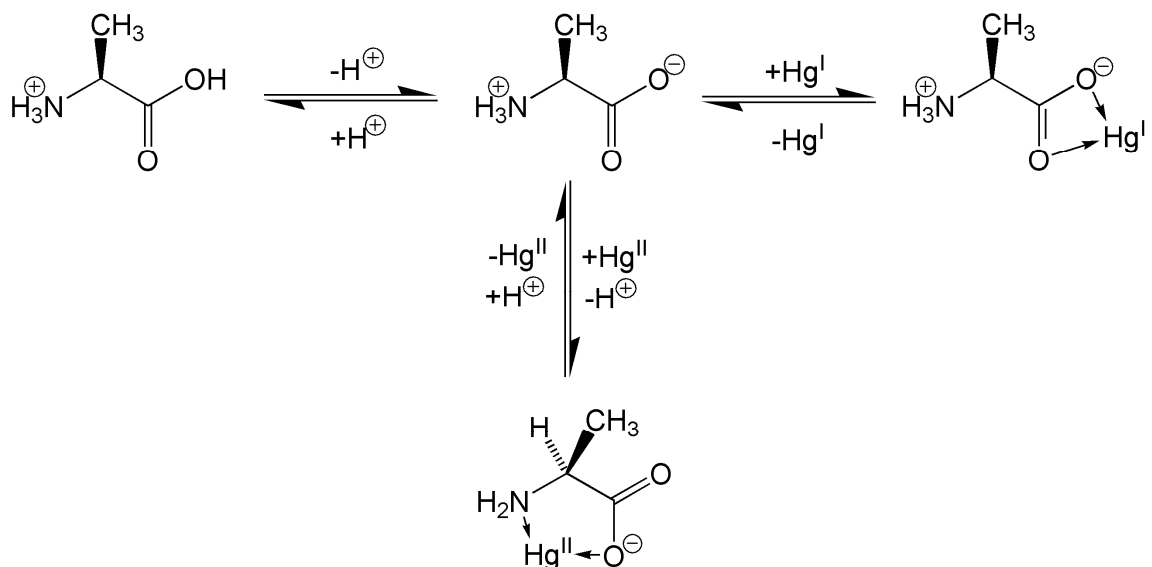


Figure 3.6: Competition equilibria between protons, mercury(I) and mercury(II) for alanine, with mercury coordination based on solid state structure coordination.

3.3.2 Hydrogen-1 Solution NMR Spectroscopy

Hydrogen-1 NMR spectra for deuterium oxide solutions of crystals of Hg-LAla or Hg-DAla and for reaction mixtures (at four concentrations) that give Hg-DAla crystals (Hg^I+DAla) are presented in Figure 3.7 and Figure 3.8, respectively.

In both sample types (dissolved crystals and reaction mixtures), four signals are seen for the methine protons (Figure 3.8 inset). These four signals either represent four distinct alanine environments or two methine environments corresponding to alanine interactions with mercury(I) and mercury(II), where the mercury(II) affected signal has mercury-199 satellites.

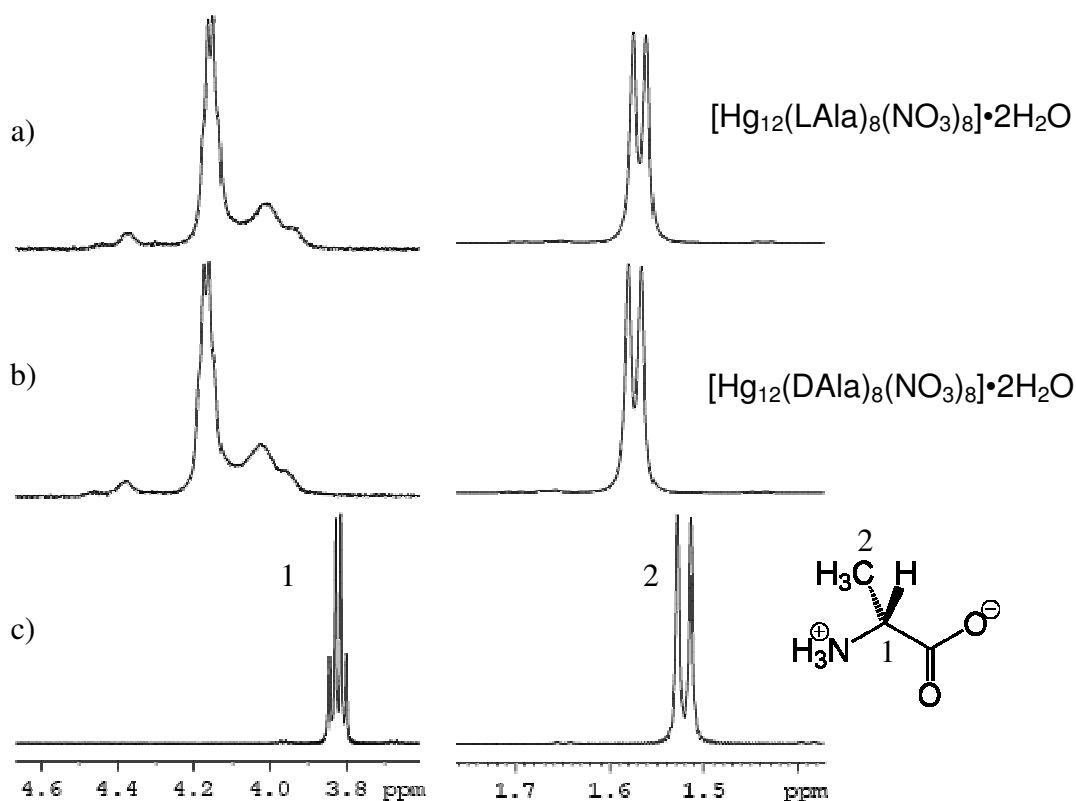


Figure 3.7: Solution state hydrogen-1 NMR of a) Hg-LAla crystals (<0.0026 M), b) Hg-DAla crystals (<0.0026 M) and c) D-alanine (pD *ca.* 7) dissolved in deuterium oxide. The methyl and methine peaks are not normalized.⁴⁴

In every experimental spectrum, the two smaller signals (indicated by S in Figure 3.8 inset) are symmetric about the second most deshielded signal and have a consistent inter-peak distance of 210 to 220 Hz. A ³J_{HHg} coupling constant *ca.* 215 Hz is slightly larger than that of β hydrogen atoms of alkyl-mercury compounds,¹¹³ but we feel is reasonable for coupling through a heteroatom. In addition, it was found that in all cases the relative peak integration ratio of the most deshielded signal to the second most deshielded signal is about 7 % to 10 %, which is half the abundance of mercury-199 (16.9 % abundant).

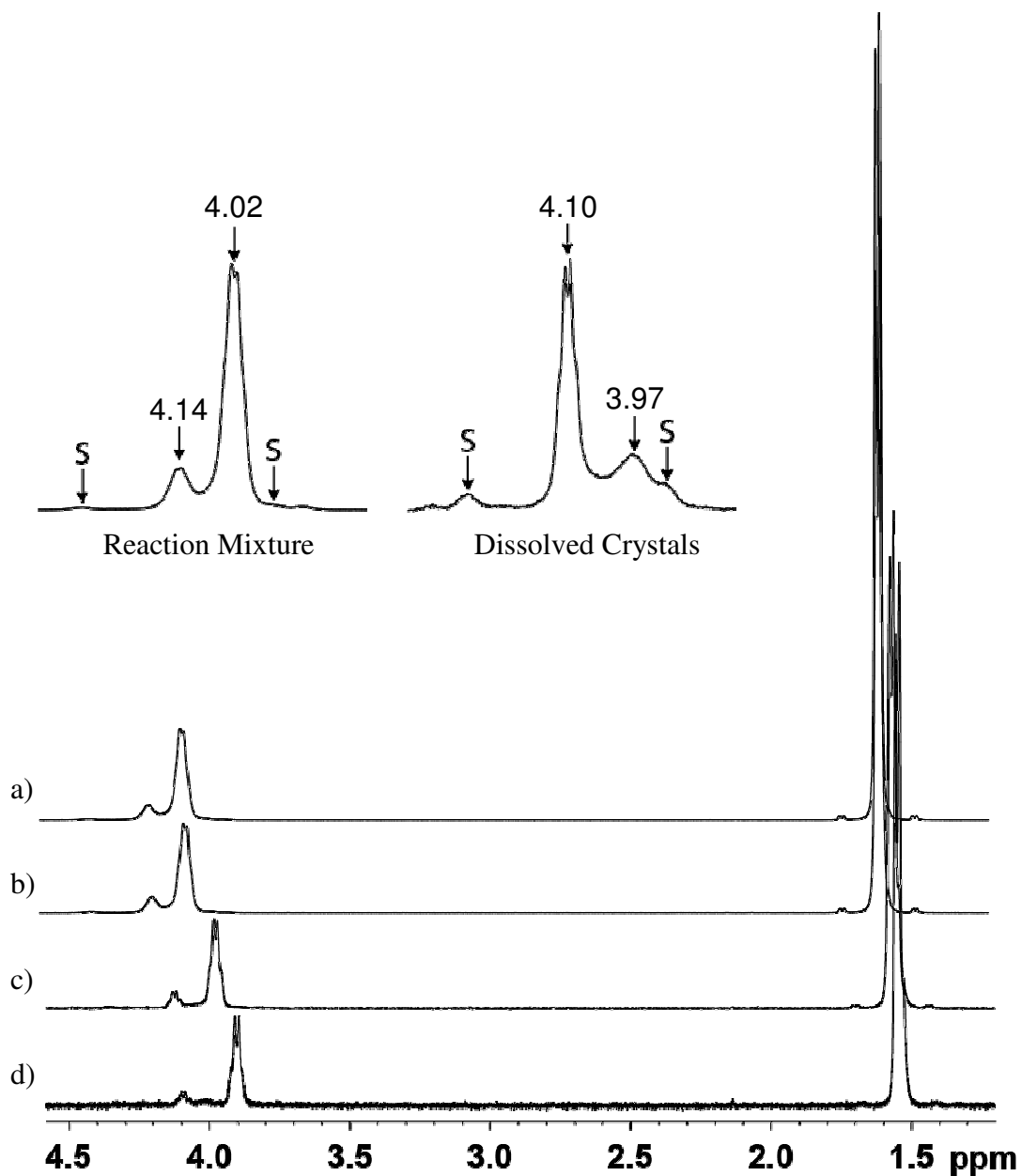


Figure 3.8: Solution state hydrogen-1 NMR spectra of the $\text{Hg}^{\text{I}}+\text{DAIa}$ reaction mixtures at various concentrations a) 0.125 M, b) 0.080 M, c) 0.010 M, and d) 0.003 M. Inset: Comparison of methine signal for the reaction mixture (0.0125 M) and dissolved crystals (< 0.0026 M), methine peaks (ppm) and potential mercury satellites (S) are labelled.⁴⁴

A number of experiments that could definitively distinguish between the two possibilities of methine environments have been carried out. These include two dimensional ^1H - ^{199}Hg experiments, in which mercury-199 signals could not be detected, and variable temperature NMR experiments, in which more accurate integration values could be obtained. At higher temperatures exchange would occur more quickly and at lower temperatures exchange would slow. In both cases, the peaks may become more defined and more accurate integration values would be obtained. Unfortunately, the use of deuterium oxide as a solvent limited the usefulness of temperature variation experiments.

Hydrogen-1 NMR analysis of the reaction mixture shows a concentration dependence of the chemical shifts, which become more shielded at lower concentrations, while the shapes of the methine peaks do not change, as shown in Figure 3.8.

Alanine coordination to the mercury(II) atoms is expected through the primary amine functional group of the amino acid, while coordination to the mercury(I) atoms is expected through the carboxylate functional group.¹¹⁴ In an attempt to view this interaction in the solution state, methine proton chemical shifts for solutions of mercury(II) nitrate with LAla ($\text{Hg}^{\text{II}} + \text{LAla}$); mercury(I) nitrate with LAla ($\text{Hg}^{\text{I}} + \text{LAla}$); LAla; and mercury(I) nitrate with *N*-methyl-L-alanine ($\text{Hg}^{\text{I}} + \text{NAla}$) (a secondary amino acid) are compared in Figure 3.9. The methine peak patterns are similar between the spectra of $\text{Hg}^{\text{II}} + \text{LAla}$ (Figure 3.9a) and $\text{Hg}^{\text{I}} + \text{LAla}$ (Figure 3.9b), and between the spectra of $\text{Hg}^{\text{II}} + \text{NAla}$ (Figure 3.9d) and LAla (Figure 3.9c). Since mercury(II) is expected in both of the mercury(I) solutions—mercury(0) precipitated from each solution during preparation—the difference in mercury(II) interaction is evident when comparing the spectra of the primary amine of LAla to that of the secondary amine NAla.

The chemical shift of the second most shielded methine signal (4.09 ppm) in the reaction mixture of mercury(I) with LAla is the same as that of L-alanine at the same pD (comparing Figure 3.9b and c). In this alanine environment, the alanine is most likely undergoing a fast (less than 10^{-4} s)⁶⁴ dynamic interaction with mercury through the carboxylate oxygen atoms. This is indicated by the broadness of this signal in the mercury(I) solution when compared to that of the alanine solution.

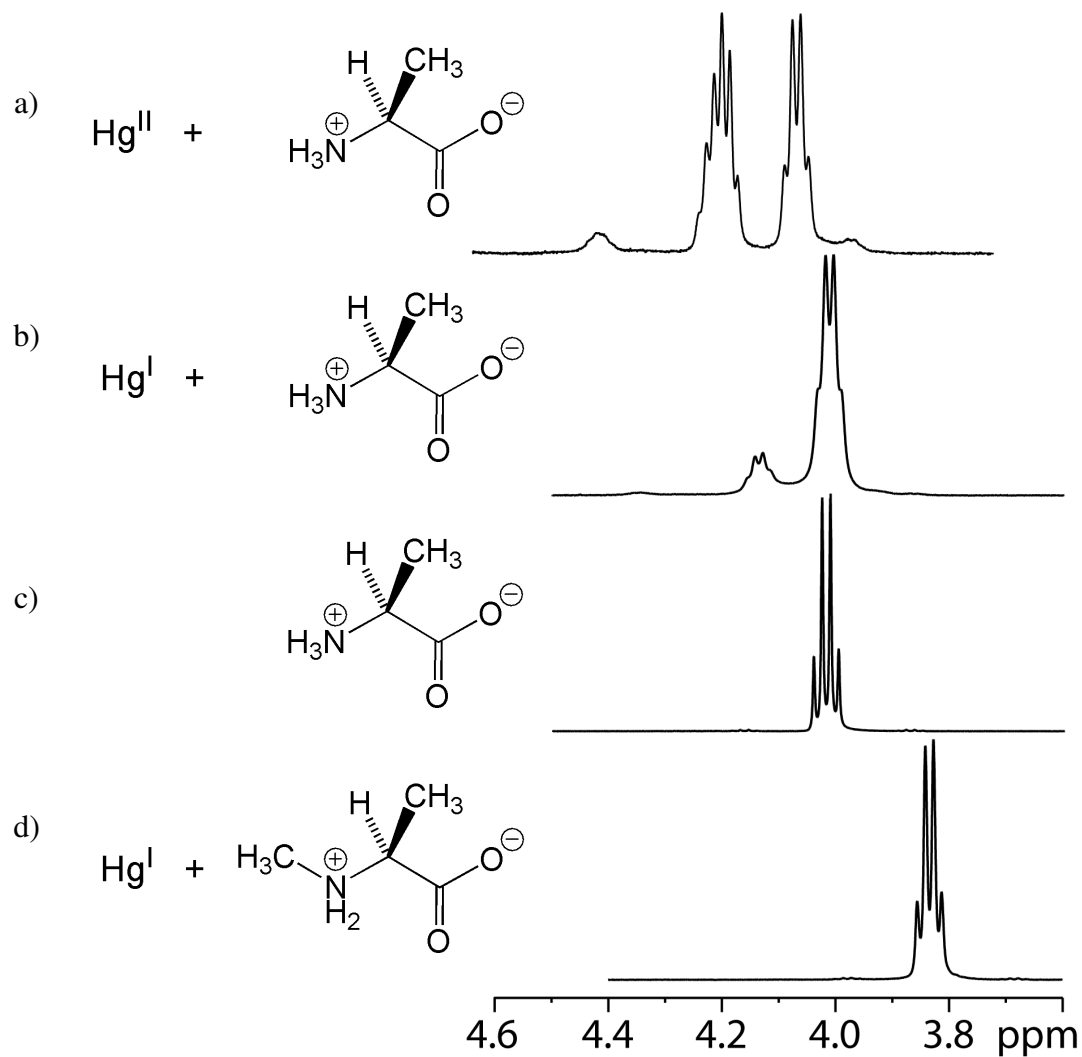


Figure 3.9: Hydrogen-1 chemical shift for the methine hydrogen atom for deuterium oxide solutions of a) Hg^{II} + LAla (at pD 2.31), b) Hg^{I} + LAla (at pD 2.38), c) LAla (at pD 2.38), and d) Hg^{I} + NAla (at pD 2.77); in 1:1 ratios of metal to amino acid and concentrations of 0.125M.

3.3.3 Carbon-13 Solution NMR Spectroscopy

Two dominant alanine environments are evident in the carbon-13 spectra, where two methine carbon signals are present in all spectra of mercury(I) containing solutions (summarized in Table 3.3). One carboxyl carbon chemical shift is seen for L-alanine by itself and the reaction mixture of L-alanine with mercurous nitrate, while two carboxyl carbon-13 signals are seen for the dissolved crystals and for the mercuric nitrate reaction mixture.

The multiplet pattern of the methine hydrogen-1 signal at 4.20 ppm in the mercury(II) with L-alanine spectrum is an overlap of two quartets. In this case, three alanine environments are present as evidenced by the three methine carbon signals in the carbon-13 spectra.

Table 3.3: Carboxyl and methine carbon-13 NMR signals for deuterium oxide solutions of LAla, Hg^I + LAla, Hg^I-LAla, Hg^I-DAla, and Hg^{II} + LAla.

Reaction Mixture or Dissolved Crystals	Solution pD	¹³ C NMR Chemical Shift (ppm)		Hg:Ala Ratio	Sample Conc. [M]
		Carboxyl Carbon	Methine Carbon		
LAla	2.38	176.4	52.0	0:1	0.125
Hg ^I + LAla	2.38	177.2	55.3 53.1	1:1	0.125
Hg-LAla	3.5	180.8 177.3	56.4 55.1	2Hg ^I :1Hg ^{II} :2	<0.0026
Hg-DAla	3.8	180.3 175.9	55.9 55.7	2Hg ^I :1Hg ^{II} :2	<0.0026
Hg ^{II} + LAla	2.31	180.6 176.8	54.9 54.8 52.7	1:1	0.125

As discussed in the lead-amino acid chapter (Chapter 2), metal-amino acid interactions through the carboxylate group are pD dependent and may not show a large chemical shift difference between metal-amino acid and amino acid solutions at more acidic pD values. With this in mind, the chemical shift differences for the carboxyl carbon of alanine molecules in solution, when compared with those in reaction mixtures of alanine with mercury(I) or with mercury(II) at similar pD values, are between 0.6 and 1.2 ppm. The smaller downfield chemical shift differences (at values less than 1 ppm) were not deemed significant enough to be definitive evidence of mercury-alanine interaction.

3.4 RESULTS AND DISCUSSION: GAS PHASE CHARACTERIZATION

3.4.1 ESI-MS

ESI-MS data obtained for reaction mixtures of mercurous nitrate with LAla, DAla or DLAla (Table 3.4 and Figure 3.10a) and for solutions of crystals of Hg-LAla or Hg-DAla dissolved in distilled water or 50% methanol/water (v/v) show peaks at m/z 308, m/z 863, and m/z 1151. The peaks correspond to complex cations containing mercury and are observed independent of the flow solvent (distilled water and 50% methanol/water (v/v)). The assignments of m/z 308 as $[\text{Hg}^{\text{II}}(\text{Ala})\cdot\text{H}_2\text{O} - \text{H}]^+$, m/z 863 as $[\text{Hg}^{\text{I}}_2(\text{Ala})_5\cdot\text{H}_2\text{O} - \text{H}]^+$ and m/z 1151 as $[\text{Hg}^{\text{I}}_2\text{Hg}^{\text{II}}(\text{Ala})_6\cdot\text{H}_2\text{O} - 3\text{H}]^+$ have been confirmed by comparison of experimental and calculated isotope peak patterns, as well as tandem mass spectra for m/z 308 (Figure 3.10b). Alanine can hold a positive, neutral or negative charge depending on the number of protons it possesses. The complex cation formulae observed in the ESI-MS are considered to contain neutral alanine ligands with a loss of -xH from the complex. Peaks corresponding to complexes with either (and both) mercury oxidation states are present in the ESI mass spectra indicating that at least two alanine environments exist in the gas phase, consistent with observations from the solution hydrogen-1 and carbon-13 NMR data.

Electrospray ionization mass spectrometric analysis of 50% ethanol/water (v/v) solutions of trace metals and the 20 common amino acids (as well as homocysteine) were

previously performed.⁶⁸ Analysis of mercury(I)-alanine and mercury(II)-alanine solutions resulted in no detectable mercury(I)-alanine complex cations and five mercury(II) alanine complex cations of 1:1, 1:2, 2:2, 2:3, and 3:3 metal to ligand ratios.

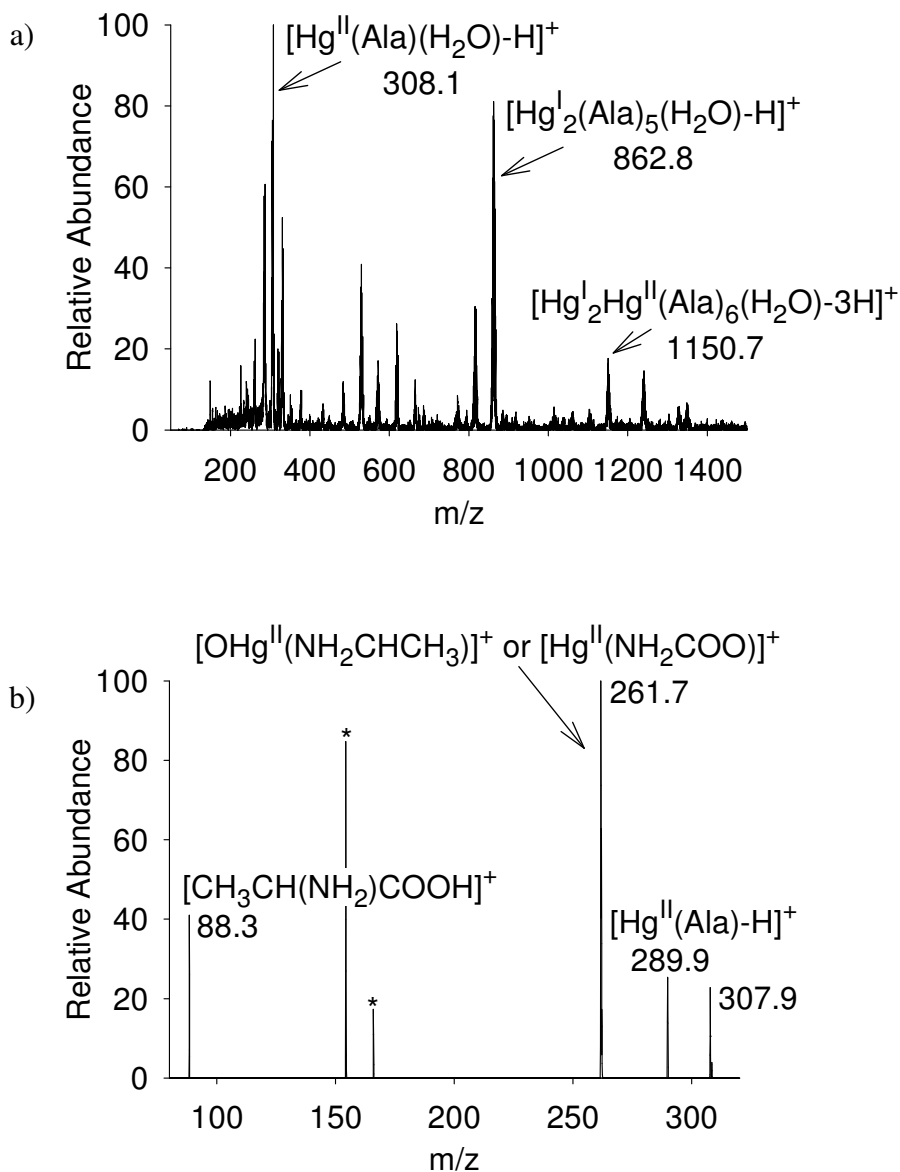


Figure 3.10: a) Positive ion ESI mass spectrum of $\text{Hg}^{\text{I}}+\text{LAla}$ in 50:50 methanol:water (v/v). b) Tandem mass spectrum of m/z 308 at 20 % collision energy, peaks indicated with an asterisk are not fragments of a mercury containing complex cation

Table 3.4: ESI-MS data for the reaction mixtures and dissolved crystals of the feature complexes, with distilled water and 50 % methanol (*italics*) as flow solvents.

m/z	Relative Abundance*					Assignment [Hg ^I :Hg ^{II} :Ala] ⁺
	Hg + LAla	Hg-LAla	Hg + DAla	Hg-DAla	Hg + DLAla	
308	H (<i>L</i>)	H (<i>H</i>)	H (<i>H</i>)	H (<i>H</i>)	H (<i>L</i>)	[0:1:1-1H+H ₂ O] ⁺
863	M (<i>M</i>)	V (<i>L</i>)	M (<i>H</i>)	V (<i>L</i>)	M (<i>H</i>)	[2:0:5-1H+H ₂ O] ⁺
1151	L (<i>L</i>)	- (<i>V</i>)	L (<i>L</i>)	- (<i>V</i>)	L (<i>L</i>)	[2:1:6-3H+H ₂ O] ⁺

*H = 75-100%; M = 35-75%; L = 5-35%; V = 2-5%, relative abundance values replicated within the given range for each flow solvent: distilled water (50% methanol).

The discrepancy between the ethanolic solution results and those presented in this work is most likely due to the sample preparation method and the amount of mercury(I) and mercury(II) in solution. The reaction mixture samples in the current work were prepared in water and heated to *ca.* 95°C. Upon heating the aqueous solution, all mercury(I) dissolved and some disproportionated to mercury(II) and mercury(0). This clear solution was then further prepared for mass spectrometric analysis. Low mercury(II) concentrations and the presence of mercury(I) in solution resulted in the presence of few mercury(II)-alanine containing complex cations in the gas phase.

The ethanolic solution samples were prepared and mixed overnight in 50% ethanol/water. The resulting cloudy solutions were suction filtered and then analysed by use of ESI-MS. The insolubility of mercury(I) (and potentially alanine) in the ethanolic solution resulted in a low metal ion concentration and a lack of mercury(I) containing complex cation peaks in the mass spectra.

3.5 CONCLUSION

An enantiomeric pair of new mercury-alanine complexes has been isolated from mixtures of mercurous nitrate and L- or D-alanine and comprehensively characterized as $[\text{Hg}_{12}(\text{Ala})_8(\text{NO}_3)_8] \cdot 2\text{H}_2\text{O}$. Both mercury(I) and mercury(II) are present in the structure. Mercury(II) results from a disproportionation process, consistent with the deposition of mercury(0), which is generally observed in reactions of mercurous with amino acids, and indicating that mercury(I) is a ready source of mercury(0) and mercury(II) in a biological environment.

Solid state, solution state and gas phase data for $[\text{Hg}_{12}(\text{Ala})_8(\text{NO}_3)_8] \cdot 2\text{H}_2\text{O}$ are interpreted in terms of two environments for alanine assigned as an interaction with mercury(I) and an interaction with mercury(II).

The data represent a comprehensive characterization of the first example of a mercury-amino acid complex involving both mercury(I) and mercury(II) within the crystal structure.

CHAPTER 4 MERCURY-SECONDARY AMINO ACID COMPLEXES

4.1 INTRODUCTION

With the exception of the mercury-alanine structure described in Chapter 3, complexes of mercury(I) with amino acids have not been reported. Mercury(I)-alanine interactions were observed to occur through the carboxylate oxygen atoms, while mercury(II) coordination was through the primary amine and carboxylate moieties. The presence of mercury(II) in the mercury-alanine crystal structure may be due the strength of the N-Hg^{II} interaction.

A secondary amine is a stronger donor and Brønsted base than a primary amine, but is a slightly larger ligand. These differences in amine bonding characteristics might reveal a preference for amino acid coordination to mercury(I) rather than to mercury(II). To this effect, aqueous reaction mixtures of mercury(I) with secondary amino acids were examined and two complexes were isolated in the solid state from solutions of mercurous nitrate dihydrate with L-proline or *N*-methyl-L-alanine (Figure 4.1).

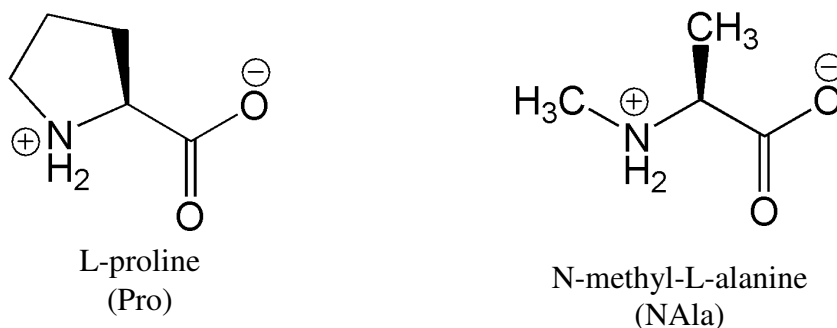


Figure 4.1: Amino acids of interest in Chapter 4.

The solid state structures contain mercury(I) associated by the amino acids, through the carboxylate oxygen atoms, in a linear polymeric array. Disproportionation of mercury(I) did occur, as mercury(0) was evident in the reaction mixture, yet mercury(II) was not present in the crystal structure.

This report includes the first solid state characterization of mercury(I)-amino acid complexes that contain only mercury(I). The compounds have been characterized using X-ray crystallography, vibrational spectroscopy, solution state NMR spectroscopy and electrospray ionization mass-spectrometry.

4.2 RESULTS AND DISCUSSION: SOLID STATE CHARACTERIZATION

Appropriate conditions have been established for the crystallization of two mercury(I)-secondary amino acid complexes. Heated (90 °C) mixtures of L-proline (Pro) or *N*-methyl-L-alanine (NAla) with mercurous nitrate in distilled water precipitated elemental mercury. By slow cooling and evaporation, followed by nucleation of the concentrated sample, colourless crystals were afforded that have been characterized as Hg₂(L-proline)₂(NO₃)₂ and [Hg₂(*N*-methyl-L-alanine)₂(NO₃)₂]₂•2H₂O, respectively. Hg₂(L-proline)₂(NO₃)₂ is extremely hygroscopic.

4.2.1 Single Crystal X-Ray Diffraction: Mercury-L-Proline

With two mercury(I) atoms, two zwitterionic L-proline molecules, and two nitrate anions, the formula for the asymmetric unit is Hg₂(L-proline)₂(NO₃)₂, (Hg-Pro) Figure 4.2. Each mercury(I) is part of a dimeric pair and is six coordinate, with oxygen interactions from a close proline molecule, a nitrate counter anion, and a more distant proline molecule from an adjacent asymmetric unit (Hg1-O3' 3.069(4) Å and Hg2-O1" 2.610(3) Å). The extended structure results from alternating mercury(I) dimers and proline carboxylate oxygen atoms, Figure 4.3.

The Hg^I-Hg^I bond distance (2.5231(4) Å) is within the ranges from the mercury-alanine structures described in Chapter 3. The Hg-O bond distances and nearly linear Hg-Hg-O

bond angles of the closest oxygen atom to each mercury(I) (Hg1-O1 2.158(3) Å and Hg2-Hg1-O1 165.79(9) °; and Hg2-O3 2.179(3) Å and Hg1-Hg2-O2 164.18(10) °) are similar to those of the mercury-alanine structure, Table 4.1. Three hydrogen bonds in the structure (N-H···O interactions) are from the amine hydrogen atoms to nitrate oxygen atoms and to a carboxylate oxygen atom.

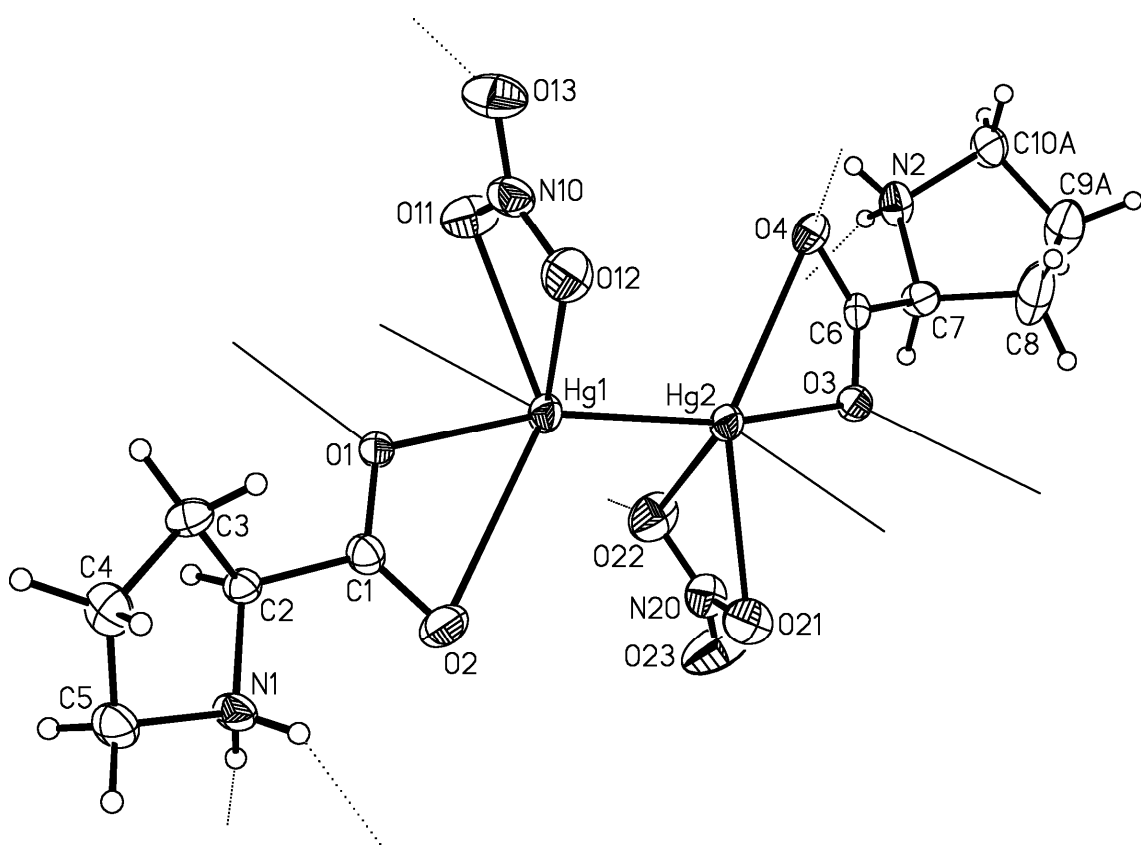


Figure 4.2: Perspective view of the contents of the asymmetric unit of Hg-Pro showing the atom labelling scheme (only one part of the disordered proline ligand (carbon atoms C9A and C10A) is shown). Non-hydrogen atoms are represented by Gaussian ellipsoids at the 50% probability level. Hydrogen atoms are shown with arbitrarily small thermal parameters. The thin lines represent the Hg–O bonds between adjacent Hg-Pro fragments; likewise, the dotted lines represent hydrogen-bonded interactions.

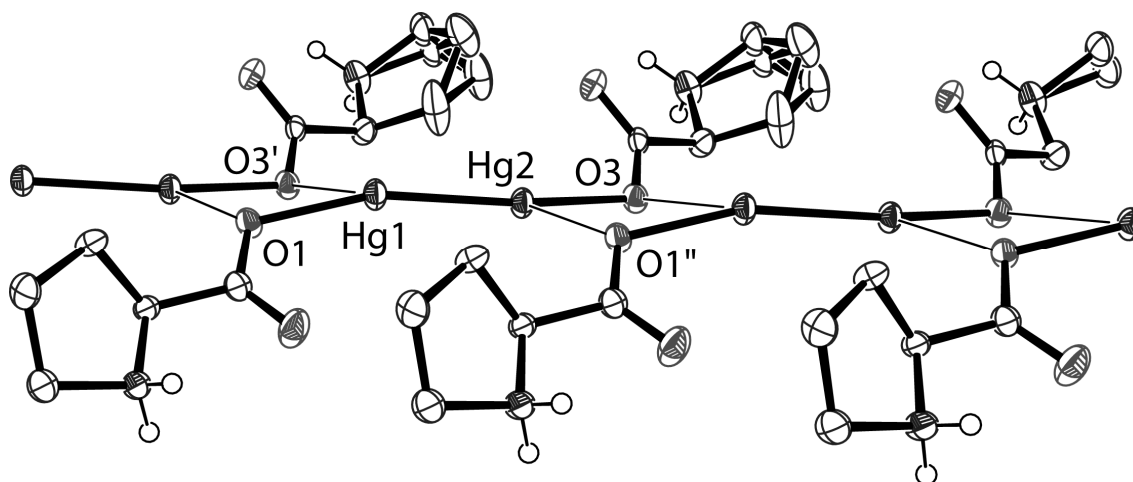


Figure 4.3: Alternating pattern of mercury dimeric pairs and proline molecules to form the extended structure of Hg-Pro. Nitrate ions and some hydrogen atoms removed for clarity.

4.2.2 Single Crystal X-Ray Diffraction: Mercury-*N*-Methyl-L-Alanine

In contrast to Hg-Pro, the mercury(I)-*N*-methyl-L-alanine structure contains two water molecules, in addition to two mercury(I) atoms, two zwitterionic secondary amino acids, two nitrate counter anions, giving the formula $[\text{Hg}_2(\text{N-methyl-L-alanine})_2(\text{NO}_3)_2] \cdot 2\text{H}_2\text{O}$, (Hg-NAla) Figure 4.4. Each mercury(I) is six coordinate with a mercury(I)-mercury(I) bond length of 2.5108(6) Å and mercury-oxygen interactions to two *N*-methyl-L-alanine molecules, and either a nitrate counter anion or two water molecules. The shortest mercury-oxygen bonds (Hg1-O10 2.131(9) Å and Hg2-O20' 2.149(7) Å) are to oxygen atoms that are in line with the mercury(I) dimers (Hg2-Hg-1-O10 176.1(2) ° and Hg1-Hg2-O20' 169.2(2) °). These values are in the ranges of the mercury-alanine structures from Chapter 3 (Table 4.1).

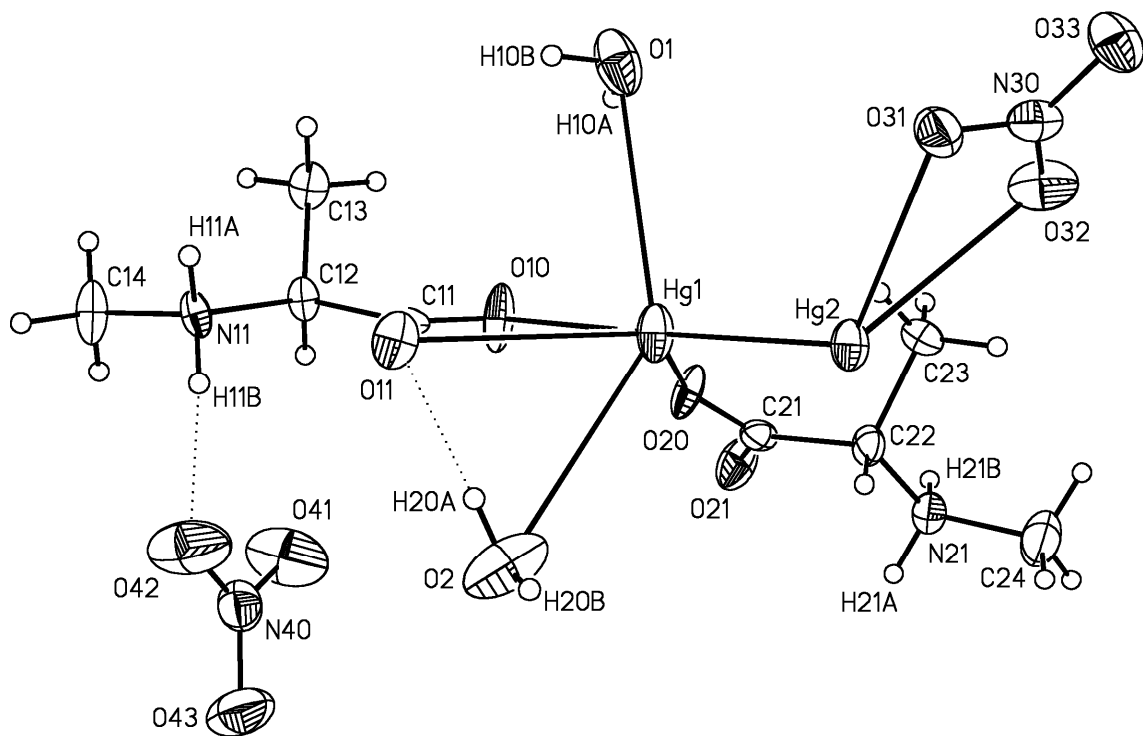


Figure 4.4: Perspective view of the asymmetric unit (unique atom set) of Hg-NAla showing the atom labelling scheme. Non-hydrogen atoms are represented by Gaussian ellipsoids at the 50% probability level. Hydrogen atoms are shown with arbitrarily small thermal parameters.

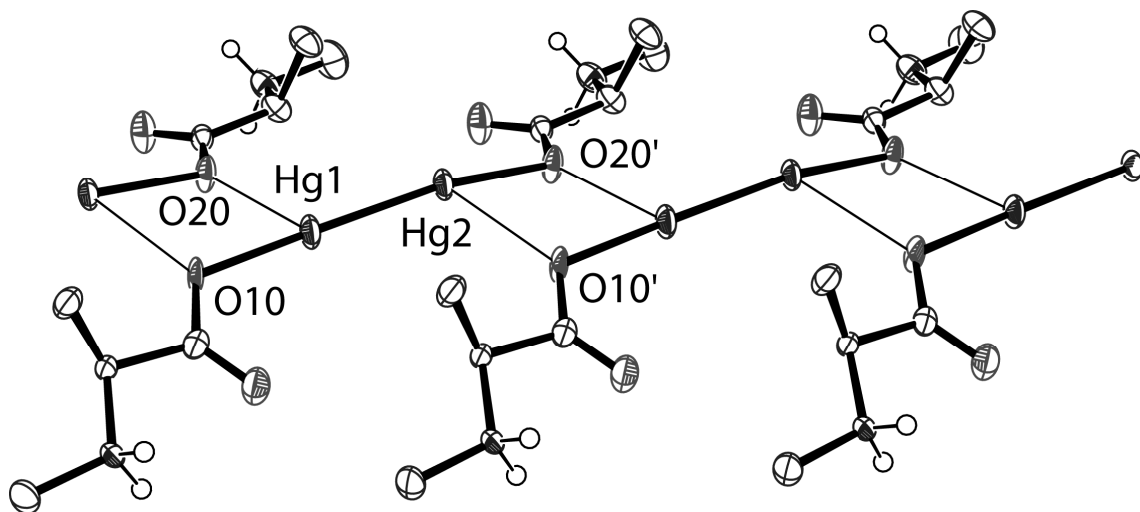


Figure 4.5: Alternating pattern of mercury dimeric pairs and *N*-methyl-L-alanine molecules to form the extended structure of Hg-NAla. Water molecules, nitrate ions and some hydrogen atoms removed for clarity.

The polymeric structure is similar to that of the extended mercury(I)-proline structure, where the adjacent asymmetric units are connected via alternating proline carboxylate functional groups and mercury(I) dimers (Hg1-O20 2.617(7) Å and Hg2-O10' 2.727(8) Å), Figure 4.5. Hydrogen bonds within the structure include N-H···O interactions from the amine hydrogen atoms to oxygen atoms from water molecules and nitrate counter ions and O-H···O interactions from water hydrogen atoms to a carboxylate oxygen atom and nitrate oxygen atoms.

Table 4.1: Interatomic distances and ranges in Hg-Pro, Hg-NAla, Hg-Ala.

Bond	Hg-Pro [Å]	Hg-NAla [Å]	Hg-Ala [Å]	Typical Ranges (<i>Ref.</i>)
Hg ^I -Hg ^I	2.5231(4)	2.5108(6)	2.5033(9)- 2.5233(5)	2.50-2.52 (37-40)
Hg ^I -O (amino acid)	2.158(3) 2.179(3) 2.610(3)-3.069(4)	2.131(8) 2.149(7) 2.617(7)-3.086(8)	2.122(9)- 2.225(11)	2.09-2.15 (37-40)
Hg ^I -O (nitrate) (<i>water</i>)	2.542(4)-2.847(4)	2.615(8)-2.991(9) 3.208(11)-3.325(13)	2.430(10)- 3.060(14)	2.46-2.96 (109)

4.2.3 Vibrational Spectroscopy

Raman stretches of the Hg^I-Hg^I pair are affected by the ligand attachment and are found at wavenumbers between 160 cm⁻¹ and 200 cm⁻¹.^{96;97} The broad Raman mercury-mercury stretches of 182 cm⁻¹ for Hg-Pro and 164 cm⁻¹ of Hg-NAla were consistent with the broad stretches of the mercury-alanine structures 160 cm⁻¹ (Hg-LAla) or 159 cm⁻¹ (Hg-DAla).⁹⁶ The sharp peak at 181 cm⁻¹ of the Hg-Hg stretch in mercurous nitrate was not present in the spectra, nor were Hg-O water (at 400 cm⁻¹) or Hg-O nitrate (at 280 cm⁻¹) stretches.

4.3 RESULTS AND DISCUSSION: SOLUTION STATE CHARACTERIZATION

4.3.1 Solution NMR Characterization

As discussed in the previous chapter (Chapter 3), solution NMR experiments to detect mercury-199 signals were not successful. Coordination modes of the amino acid and mercury(I) in solution will dictate the nuclei that should be studied using solution state NMR spectroscopy. When comparing a solution of an amino acid against a solution of the amino acid with mercury(I), at the same pD values, coordination through the amine will affect the chemical shift of the methine proton on the amino acid backbone, while coordination through the carboxylate carbon will effect a change in the carboxylate carbon signal.

4.3.2 Hydrogen-1 NMR Spectroscopy

Comparisons of the hydrogen-1 NMR signals for reaction mixtures, dissolved crystals, and secondary amino acids are presented in Figure 4.6 for Hg-Pro and Figure 4.7 for Hg-NAla. In both sets of spectra (Hg-Pro and Hg-NAla) the methine signal is a single quartet. This is dissimilar to the methine signals in the Hg^I-Ala and the Hg^{II}-Ala spectra discussed in Chapter 3. Mercury(II) is present in both the Hg^I-Pro and the Hg^I-NAla reaction mixtures (mercury(0) precipitated out of the reaction mixture) and dissolved crystals, but unlike the mercury-alanine spectra, the methine signal (and its proposed satellites) associated with mercury(II) in solution is not apparent in the mercury(I)-secondary amino acid solutions.

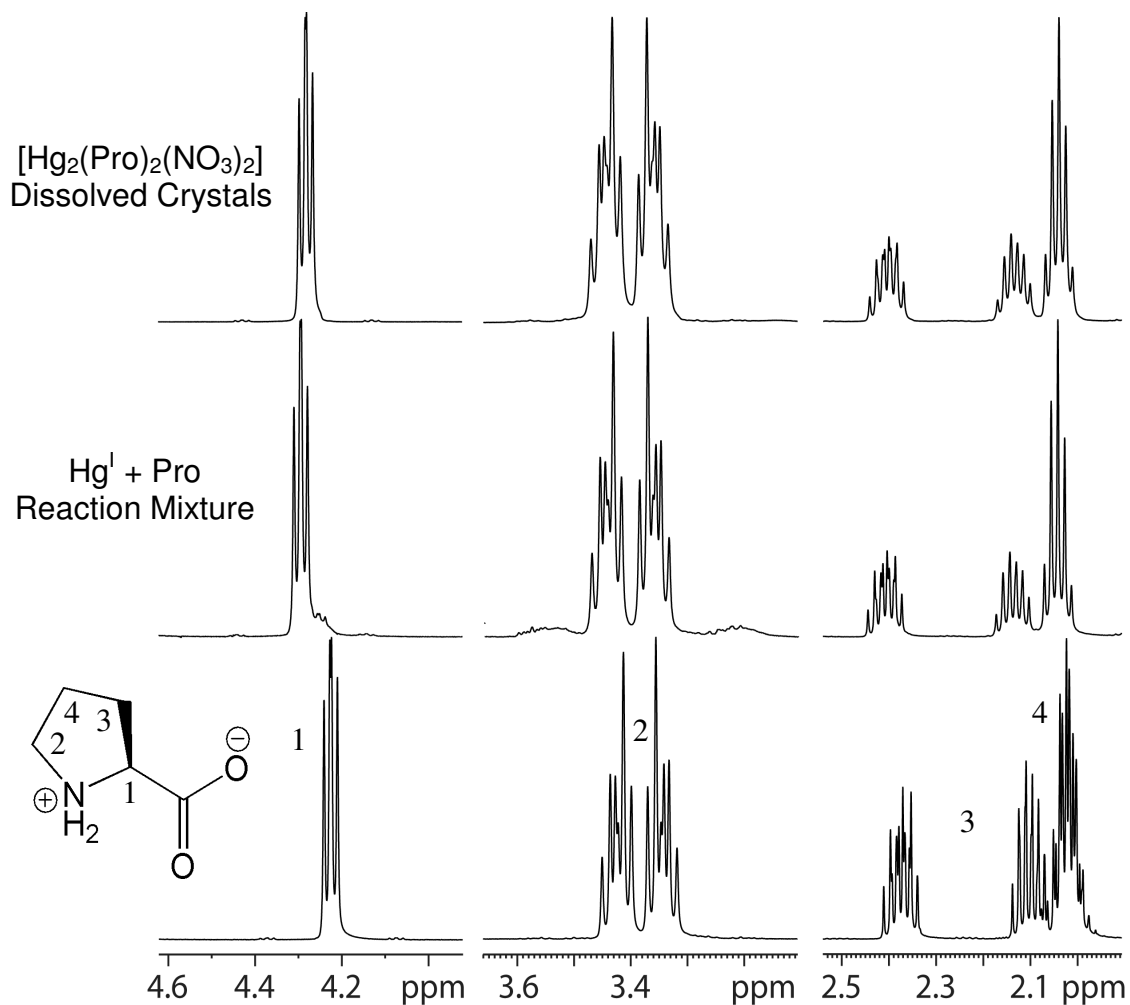


Figure 4.6: Hydrogen-1 chemical shifts of L-proline solution (*bottom*), mercury(I) nitrate with L-proline reaction mixture (*middle*) and Hg-Pro in deuterium oxide (*top*), with pD values of 2.61, 2.49, and 2.9, respectively.

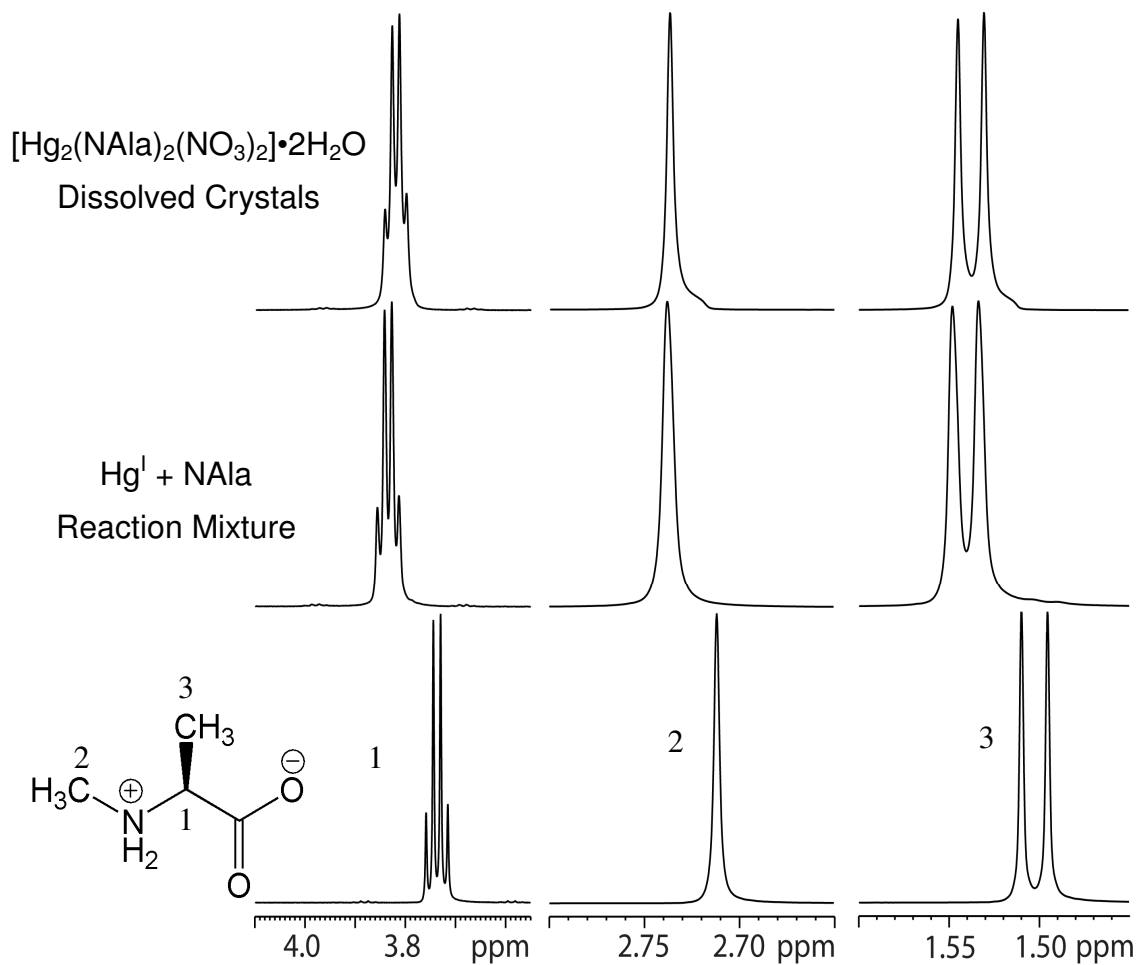


Figure 4.7: Hydrogen-1 signals of *N*-methyl-L-alanine solution (*bottom*), mercury(I) nitrate with NAla reaction mixture (*middle*) and Hg-NAla in deuterium oxide (*top*), with pD values of 2.79, 2.77, and 3.2, respectively.

4.3.3 Carbon-13 NMR Spectroscopy

Neither the carboxyl carbon chemical shifts nor the methine carbon chemical shifts are significantly different when comparing the amino acid solution to the mercury(I) with amino acid reaction mixture or to the dissolved crystal sample (Table 4.2). Only one chemical shift is evident for each carbon nucleus indicating only one dominant environment for the two secondary amino acids (Pro and NAla) in solution.

Table 4.2: Carboxyl and methine carbon-13 solution NMR chemical shifts of mercury(I) with secondary amino acid solutions

Sample	Solution pD	¹³ C NMR Chemical Shift (ppm)	
		Carboxyl Carbon	Methine Carbon
Pro + DNO ₃	2.61	176.4	63.4
Hg ^I + Pro	2.49	176.6	64.2
<i>Hg-Pro</i>	2.9	176.3	63.9
NAla + DNO ₃	2.79	176.8	60.9
Hg ^I + NAla	2.77	176.9	61.6
<i>Hg-NAla</i>	3.2	176.0	60.7

In both reaction mixture and dissolved crystal spectra of the carbon-13 and hydrogen-1 nuclei, two DSS reference peaks are seen for the methyl groups on the silicon, where the most upfield peak was chosen as the zero ppm reference point in all cases. This pattern is similar to that seen in the Hg^I-Ala spectra and the Hg^{II}-LAla spectra discussed in the Chapter 3. The downfield signal is, most likely, a result of an interaction in solution between DSS and mercury(II), as mercury(II) was present in all mercury containing solutions.

4.4 RESULTS AND DISCUSSION: GAS PHASE CHARACTERIZATION

4.4.1 ESI-MS

ESI-MS data obtained for reaction mixtures of mercurous nitrate with L-proline or *N*-methyl-L-alanine and for solutions of Hg-Pro and Hg-NAla dissolved in distilled water or 50% methanol/water (*v/v*) show a number of mercury containing peaks. Most peaks corresponding to complex cations containing mercury are observed independent of the flow solvent (distilled water and 50% methanol/water (*v/v*)). An amino acid can hold a positive, neutral or negative charge depending on the number of protons it possesses. The complex cation formulae observed in the ESI-MS are considered to contain neutral alanine ligands with a loss of -xH from the complex.

Table 4.3: ESI-MS data for the reaction mixtures of mercurous nitrate dihydrate and L-proline (Hg + Pro) or *N*-methyl-L-alanine (Hg + NAla) and for aqueous solutions of Hg-Pro and Hg-NAla with distilled water and 50% methanol (*italicized*) as flow solvents.

Assignment [Hg ^I :Hg ^{II} :amino acid]	Relative Abundance*					
	<i>m/z</i>	Hg + Pro	Hg- Pro	<i>m/z</i>	Hg + NAla	Hg- NAla
[0:1:1-1H+H ₂ O] ⁺	334	L (<i>H</i>)	L (<i>H</i>)	322	H (<i>H</i>)	M (<i>H</i>)
[0:1:1-1H+MeOH] ⁺	348	- (<i>L</i>)	- (<i>L</i>)	336	- (<i>L</i>)	- (<i>L</i>)
[0:2:1-1H+Na+NO ₃ +2OH] ⁺	637	M (<i>M</i>)	M (<i>L</i>)			

*H = 75-100%; M = 35-75%; L = 5-35%; V = 2-5%, relative abundance values replicated within the given range for each flow solvent: distilled water (50% methanol).

No mercury(I) complex cations were detected in the gas phase, while 1:1 mercury(II) to amino acid complex cations were detected in the reaction mixture and dissolved crystal analyses for both the Hg-Pro and Hg-NAla solutions. A 2:1 mercury(II) complex cation was detected in all L-proline solutions (Table 4.3).

Referring to the same metal-amino acid ESI-MS study as discussed in Section 3.4.1,⁶⁸ analysis of mercury(I)-proline solutions gave two complex cations that were detected in the gas phase with metal to ligand ratios of 1:1 and 2:3. In the current study, the ESI-MS analysis of Hg^I+Pro or Hg^I-Pro solutions only gave peaks that correspond to 1:1 and 2:1 (mercury(II) to Pro) complex cations. There were additional complex cations containing mercury dimers or clusters (assessed by the spectral patterns) that gave peaks in the ESI mass spectra but these cations are currently not identified. Mercury containing complex anions were not evident in the gas phase.

Mercury(0) did not precipitate from solution during ESI-MS sample preparation, indicating that mercury(I) was present in solution. In the case of these mercury(I)-secondary amino acid solutions, ESI-MS could not be used to detect mercury(I) containing cationic or anionic complexes or clusters.

4.5 CONCLUSIONS

Two mercury-secondary amino acid complexes have been isolated from mixtures of mercurous nitrate and L-proline or *N*-methyl-L-alanine and characterized as [Hg₂(Pro)₂(NO₃)₂] and [Hg₂(NAla)₂(NO₃)₂]•2H₂O, respectively. In each structure, the amino acids were zwitterionic with positively charged amine functional groups and coordinating anionic carboxylate groups. Mercury(I) was the only metal centre present in both structures, as characterized by the vibrational spectra. It was not possible to obtain supporting evidence for mercury(I)-amino acid complexes in the gas phase.

Disproportionation of mercury(I) dimer to mercury(II) and mercury(0) was evidenced by the disposition of mercury(0) in the reaction mixtures. Mercury(II)-secondary amino acid complexes were observed in the gas phase using ESI-MS; however, mercury(II)-secondary amino acid interactions were not evident in the hydrogen-1 and carbon-13 solution state NMR analyses. Raman Hg-Hg stretches are affected by ligand coordination,⁹⁷ and may be useful in determining mercury(I)-amino acid interactions in solution.

CHAPTER 5 CONCLUSION

5.1 SUMMARY

Toxic, trace metals are used for a variety of commercial and industrial purposes. For example, lead is used in the production of car storage batteries and in solder,^{3;13} and mercury is found in fluorescent lights, and in the gas emissions of Portland Cement production.¹¹⁵ Improper disposal of metal containing products or discharge of metal containing industrial waste has previously resulted, and continues to result, in the release of toxic metals into the environment.

Lead and mercury have the potential to be toxic to exposed individuals, both as large acute doses and as accumulated low doses.^{2;3} They can replace metal cations essential to enzyme performance or bond with biological molecules such as proteins and DNA causing, among other effects, histological and biochemical abnormalities of the central and peripheral nervous systems, abnormal fetal development, and, in the case of lead, abnormal red blood cell production.^{116;117} Although the effects of toxic metal exposure have been well studied, the exact nature of the metal-biological molecule interactions is not known or well understood.

Currently, treatments for metal exposure and intoxication are not metal specific and will redistribute toxic metals throughout the body.¹⁵ In order to improve the treatments for metal exposure and poisoning, new metal chelators must be designed and synthesized.

The goal of the research presented in this work was to study the coordination chemistry of two toxic metals, lead and mercury, and their interactions with simple biologically relevant molecules, amino acids. Our focus was on isolation and extensive characterization of complexes formed between toxic metals and biological, or structurally similar, molecules that contain oxygen, nitrogen and sulfur atoms, which can bind to the target metal. As this is an underdeveloped field, isolation methods of the metal-amino acid complexes needed to be established and methods for the definitive characterization of these complexes in the solid state, the solution state and the gas phase were assessed.

5.1.1 Lead-Amino Acid Complexes

To date six lead-amino acid complexes have been published.³⁰⁻³⁵ In this work, five additional complexes have been isolated from acidic aqueous lead-amino acid solutions, with the formulae $[\text{Pb}(\text{OH}_2)(\text{Ile})_2][\text{NO}_3]_2 \cdot \text{H}_2\text{O}$, $[\text{Pb}(\text{OH}_2)_2(\text{Val})(\text{Ile})(\text{NO}_3)][\text{NO}_3]$, $[\text{Pb}(\text{OH}_2)_2(\text{Phe})_2(\text{NO}_3)][\text{NO}_3]$ (a dihydrate), $[\text{Pb}(\text{OH}_2)(\text{Phe})_2][\text{NO}_3]_2 \cdot 2\text{H}_2\text{O}$ (a trihydrate), and $\text{Pb}_2(\text{HArg})_3(\text{H}_2\text{O})(\text{NO}_3)_7 \cdot 3\text{H}_2\text{O}$. In all of these newly isolated complexes, the amines are protonated and coordination to the lead centres occurs through the carboxylate oxygen atoms of the amino acids. All structures contained a 1:2 lead to amino acid stoichiometric ratio. A 1:1 lead to amino acid complex was also present in the lead-cationic arginine structure, resulting in two distinctly different lead-207 isotropic shifts in the solid state NMR spectrum of the lead-arginine system.

As a borderline Lewis acid, lead can form interactions with both hard and soft Lewis basic atoms, and the hardness or softness of the ligand can affect the geometry of the coordination environment of the lead centre. In the lead-amino acid examples presented in this work, lead interactions are solely observed with hard oxygen atoms and, at shorter bond lengths, a hemidirected coordination environment is evident in all cases.

5.1.2 Mercury-Amino Acid Complexes

Four new mercury-amino acid complexes have been isolated from mixtures of mercurous nitrate and primary or secondary amino acids giving complexes with formulae $[\text{Hg}_{12}(\text{L-alanine})_8(\text{NO}_3)_8] \cdot 2\text{H}_2\text{O}$, $[\text{Hg}_{12}(\text{D-alanine})_8(\text{NO}_3)_8] \cdot 2\text{H}_2\text{O}$, $[\text{Hg}_2(\text{Pro})_2(\text{NO}_3)_2]$ and $[\text{Hg}_2(\text{NAla})_2(\text{NO}_3)_2] \cdot 2\text{H}_2\text{O}$. Because L- and D- enantiomers of alanine were used separately as ligands, the crystal structures of the mercury-alanine complexes were mirror images of each other.

In all mercury-amino acid reactions, disproportionation of mercury(I) dimers occurred producing mercury(II) and mercury(0). Mercury(II) was incorporated into the mercury-primary amino acid complexes allowing the differences in coordination environment of mercury(I) and of mercury(II) to be seen within the structure. Mercury(I) was

coordinated exclusively by oxygen atoms while mercury(II) was coordinated by nitrogen atoms (of the primary amines) and also by oxygen atoms.

Conversely, mercury(II) was not incorporated into the mercury-secondary amino acid complexes and the amine was fully protonated. The mercury(I) dimers were coordinated by oxygen atoms of the amino acid carboxylate groups and by nitrate counter ions.

5.1.3 Characterization Techniques

Characterization of the lead-amino acid and mercury-amino acid complexes was performed in the solid state, the solution state and the gas phase. Solid state structures were determined using X-ray crystallography, while the bulk of the solid state samples were analysed using carbon-13 (and lead-207) solid state NMR spectroscopy and vibrational spectroscopies. In most cases, the crystal structure was found to be representative of the bulk sample.

Deuterium oxide solutions of the reaction mixtures and of the dissolved crystals were analysed using hydrogen-1, carbon-13 and, where applicable, lead-207 NMR spectroscopy. The metal chemical shift was the most useful in assessing the metal-amino acid interactions in solution. The pD of each solution affected the metal-amino acid interactions, where at more acidic pD values deuterons competed with metal cations for the Lewis basic atoms on the amino acid. The lead to amino acid ratio also affected the lead-207 chemical shift, where the lower the ratio, the more downfield the chemical shift. This lead to amino acid ratio trend was also seen in the solid state isotropic shifts with the number and the type of oxygen (such as carboxylate or water) in the lead-oxygen interactions affecting the isotropic shift.

Electrospray ionization mass spectrometric analysis of aqueous solutions (distilled water and 50% methanol/water) of dissolved crystals and reaction mixtures provided the gas phase characterization method. For the lead-amino acid and mercury-alanine complexes, the metal to amino acid ratios present in the solid state were also present in complex cations in the gas phase. Although mercury(I) was expected in the mercury-secondary

amino acid (L-proline and *N*-methyl-L-alanine) solutions, mercury(I) containing complex ions were not present the gas phase.

5.2 FUTURE WORK

The fundamental bioinorganic coordination chemistry of lead and mercury with biological molecule ligands is an underdeveloped field. Application of the isolation and characterization methods described in this thesis to other trace metals and biomolecules will enhance the known bioinorganic chemistry of lead and mercury.

5.2.1 Lead-Amino Acid Complexes

Additional lead-amino acid complexes should be isolable by using additional amino acids and following the procedure described in this work; however, small adjustments to the procedure may be required. For example, by increasing the pH of the reaction mixtures new complexes could be isolated from basic solutions. Deprotonation of the amine should occur at higher pH values and result in lead-amino acid interactions through both the amine nitrogen atom and the carboxylate oxygen atom(s). These interactions could then be observed in the solid state structures and solution state analyses.

Reisolation of the lead-phenylalanine trihydrate and determination of the lead-207 isotropic shift in the lead-valine-isoleucine complex using ssNMR are two important pieces of this study that have yet to be accomplished.

The lead-phenylalanine trihydrate was isolated once while the dihydrate was isolated multiple times. Adjustments to the isolation procedure should make the trihydrate reisolable.

Solid state NMR analysis of the lead-valine-isoleucine complex gave wide peaks for the carbon-13 chemical shifts, while the lead-207 isotropic shift was not determined. The isolation of this complex must be improved in order to get a purer sample which should give better solid state NMR data.

The lead-valine-isoleucine was the first isolated heteroleptic lead-amino acid complex and additional examples of this family of complexes should be easily isolable.

The lead-arginine complex was the first isolated lead-cationic amino acid complex, isolation of additional examples of this family of complexes, such as lead-lysine or heteroleptic lead-arginine-lysine, should be attempted.

5.2.2 Mercury-Amino Acid Complexes

Use of other amino acids, and adjustment of the solution pH, the metal to ligand ratios, and the rate of evaporation of the reaction mixtures, should allow additional mercury-primary amino acid and mercury-secondary amino acid complexes to be accessed; these include homoleptic as well as heteroleptic complexes.

From the NMR data, the metal centre provided the most definitive evidence of metal-amino acid interactions in the lead-amino acid solutions and, as such, the mercury-199 chemical shift could provide evidence of mercury-amino acid interactions in solution. Additional NMR experiments must be completed in order to locate the mercury-199 chemical shift.

Mercury(0) does not precipitate from solution during ESI-MS sample preparation of mercury(I) containing solutions, which means that mercury(I) must be present in these solutions. In the cases of the mercury-secondary amino acids, attempts to use ESI-MS to detect mercury(I) containing cationic or anionic clusters were unsuccessful. It was also not possible to obtain solution state NMR data for mercury(I)-amino acid interactions in solution. The mercury-mercury Raman stretch is affected by ligand coordination⁹⁷ and solution state Raman spectroscopy could be used to assess the solution mercury-amino acid interactions.

The mercury(I)-proline complex requires a long crystallization time of *ca.* five months and was found to be extremely hygroscopic. Improvements to the complex isolation methods can be made; these include adjusting the crystallization solvent and the rate of solvent evaporation.

5.2.3 Metal-Biological Molecule Complexes

With the development of this general isolation method, additional metal-biological molecule complexes may be isolable. Metals such as thallium, antimony, tin, indium and cadmium could be used. Specifically, small dipeptides and tripeptides would most likely chelate the metal centre and the peptide bond would offer an additional functional group for metal coordination.

The heaviest stable element, bismuth (α -decay $t_{1/2} = (1.9 \pm 0.2) \times 10^{19}$ yr),¹¹⁸ is in the same region of the periodic table as the toxic metals lead and mercury; however, bismuth is not toxic and is used in a number of pharmaceutical agents.¹¹⁹ Because of the opposing toxicity of mercury and lead with bismuth, a study of the coordination environment of bismuth would be an excellent contrast to that of lead or mercury. The isolation and characterization of bismuth-amino acid complexes, using the methods established in this thesis, would lead to a better understanding of the inherent non-toxic nature of bismuth compounds and to the development of the therapeutic uses of bismuth.

APPENDIX A EXPERIMENTAL PROCEDURES

A.1 SAFETY

CAUTION: Compounds of mercury and lead are highly toxic. Care must be taken when handling samples, and appropriate disposal procedures are necessary.

Metal containing samples and starting materials were handled with double-gloves (latex under nitrile) and the metals containing solids were weighed while wearing a half-face respirator with N95 particulate-chemical cartridges. Metal containing waste was disposed of according to Dalhousie University and government regulations.

A.2 GENERAL

L-Alanine, D-alanine, L-arginine, L-isoleucine, L-phenylalanine, L-proline, L-valine, sodium 2,2-dimethyl-2-silapentane-5-sulfonate (DSS), deuterium chloride (99 atom % D, 37 wt % solution in D₂O), deuterated nitric acid (99+ atom % D, 65 wt % solution in D₂O), sodium deuteroxide 99+ atom % D, 40 wt % solution in D₂O), sodium nitrate, mercury(I) nitrate dihydrate, mercury(II) nitrate hydrate were used as received from Aldrich. Potassium chloride was used as received from ACP Chemicals, Inc. *N*-methyl-L-alanine was used as received from Fluka. Lead nitrate was used as received from BDH. Nitric acid was used as received from Caledon. Deuterium oxide was used as received from Cambridge Isotopes Laboratories (99.9 atom % D) and Aldrich (99.9 atom % D). Deionized water was used in all reactions and crystallization procedures and all procedures were carried out in air, unless otherwise indicated.

A.3 METAL-AMINO ACID COMPLEX PREPARATION AND ISOLATION

Isolation of Pb(Val)₂(H₂O)₂(NO₃)₂: A stirred solution (10 minutes) of L-valine (5.00 mmol, 0.586 g) in water (10 mL, pH 6.38) was added to a solution of Pb(NO₃)₂ (5.00 mmol, 1.656 g) in water (30 mL, stirred 10 minutes, pH 3.73) resulting in a clear,

colourless solution with a pH of 4.30. The mixture was heated at 95-100 °C for 60 minutes and slowly cooled to room temperature in the filtration flask. Colourless needle-like crystals of $\text{Pb(L-valine)}_2(\text{H}_2\text{O})_2(\text{NO}_3)_2$ formed over 4 days at room temperature; yield: 0.684 g; 45.5 %; m.p. 88-92 °C. Solid ^{13}C NMR δ (ppm): 175.9, 175.3, 63.8, 62.6, 30.0, 20.4, 19.8; ^{207}Pb NMR δ : -1707 ± 5 ppm. IR data (cm^{-1}): 3475 vsb, 2900 sb, 1615 sb, 1514 m, 1153 w, 1117 m, 1057 m, 1043 w, 1025 m, 944 m, 932 m, 894 m, 821 m, 753 m, 718 m, 587 w, 558 w, 448 wb, 382 mb, 317 m. Raman data (cm^{-1}): 2973 mb, 2898 mb, 1328 vw. Solution ^{13}C NMR δ_{DSS} (ppm; D_2O ; pD = 5.0; 0.125M Val): 177.4, 63.6, 31.7, 20.6, 19.3; ^{207}Pb NMR (D_2O ; pD = 4.9; 0.125 M Pb) δ : -2525 ppm. (Abbreviations for the vibrational data: w = weak, m = medium, s = strong, b = broad, v = very.)

Isolation of $\text{Pb(Ile)}_2(\text{H}_2\text{O})_2(\text{NO}_3)_2$: A stirred mixture (10 minutes) of L-isoleucine (5.01 mmol, 0.657 g) in water (10 mL pH 6.23) was added to a solution of $\text{Pb}(\text{NO}_3)_2$ (5.00 mmol, 1.657 g) in water (30 mL, stirred 10 minutes, pH 3.73) resulting in a clear, colourless solution with a pH of 4.30. The solution was heated at 95-100 °C for 60 minutes. On slow cooling to room temperature in the filtration flask colourless needle-like crystals of $\text{Pb(L-isoleucine)}_2(\text{H}_2\text{O})_2(\text{NO}_3)_2$ formed from the filtrate over 14 days at room temperature; yield: 0.617 g; 39.1 %; m.p. 82-83 °C. Solid ^{13}C NMR δ (ppm): 175.9, 62.1, 61.6, 37.2, 35.4, 24.9, 23.6, 16.1, 15.2, 12.6, 10.6; ^{207}Pb NMR δ : -1766 ± 4 ppm. IR data (cm^{-1}): 3457 sb, 2900 sb, 1584 sb, 1505 m, 1120 m, 1067 w, 1044 w, 1031 w, 1003 m, 928 m, 881 m, 821 m, 718 w, 662 w, 587 w, 566 w, 499 m, 372 m, 315 w. Raman data (cm^{-1}): 2964 mb, 2938 mb, 2897 mb, 1445 w. Solution ^{13}C NMR δ_{DSS} (ppm D_2O ; pD = 4.9; 0.125M Ile): 177.3, 62.7, 38.5, 27.2, 17.7, 13.8; ^{207}Pb NMR (D_2O ; pD = 4.9; 0.125 M Pb) δ : -2471 ppm.

Isolation of $\text{Pb(Val)(Ile)}(\text{H}_2\text{O})_2(\text{NO}_3)_2$: A stirred mixture (10 minutes) of L-valine (5.00×10^{-3} mmol, 0.586 g) and L-isoleucine (5.02×10^{-3} mmol, 0.658 g) in water (20 mL, pH 6.21) was added to a solution of $\text{Pb}(\text{NO}_3)_2$ (5.00×10^{-3} mmol, 1.656 g) in water (20 mL stirred 10 minutes, pH 3.73) resulting in a clear, colourless solution with a pH of 4.34. The solution was heated at 95-100 °C for 60 minutes. On slow cooling to room

temperature in the filtration flask, colourless needle-like crystals of $\text{Pb(L-valine)(L-isoleucine)(H}_2\text{O)}_2(\text{NO}_3)_2$ formed from the filtrate over 13 days at room temperature; yield: 0.768 g; 25.0 %; m.p. 82-83 °C. Solid ^{13}C NMR δ (ppm): 178.8, 76.5, 63.4, 61.7, 36.9, 29.7, 25.2, 23.3, 19.5, 16.4, 15.1, 12.5. IR data (cm^{-1}): 3573 w, 3460 mb, 2900 sb, 2448 w, 2352 w, 2240 w, 1924 m, 1774 wb, 1754m, 1614m, 1575 m, 1506 m, 1260 w, 1119 w, 1058 w, 1044 w, 1001 w, 962 w, 929 m, 893 m, 821 m, 717 m, 666 m, 585 wb, 555 w, 498 m, 428 w. Raman data (cm^{-1}): 2980 mb, 2900 mb, 112 w. Solution ^{13}C NMR δ_{DSS} (ppm; D_2O ; pD = 4.9; 0.125 M Val and Ile): 177.5, 177.4, 63.8, 62.9, 38.6, 31.8, 27.2, 20.6, 19.4, 17.3, 13.8; ^{207}Pb NMR (D_2O ; pD = 4.9; 0.125 M Pb) δ : -2471 ppm.

Isolation of $\text{Pb(Phe)}_2(\text{H}_2\text{O})(\text{NO}_3)_2 \cdot \text{H}_2\text{O}$: A stirred (10 minutes) cloudy white mixture of L-phenylalanine (4.99 mmol, 0.825 g) in distilled water (10 mL pH 5.64) was added to a solution of $\text{Pb}(\text{NO}_3)_2$ (5.00 mmol, 1.657 g) in water (30 mL stirred 10 minutes, pH 3.73) resulting in a clear, colourless solution with a pH of 4.02, that was heated at 95-100 °C for 60 minutes. The colourless solution became very slightly cloudy. The hot solution was slowly cooled to room temperature in the filtration flask and colourless needle-like crystals of $\text{Pb(L-phenylalanine)}_2(\text{H}_2\text{O})(\text{NO}_3)_2 \cdot \text{H}_2\text{O}$ formed in 4 days at room temperature; yield: 1.112 g; 63.9 %; m.p. 107-110 °C. Solid ^{13}C NMR δ (ppm): 235.7, 229.1, 227.6, 226.5, 176.1, 175.2, 136.3, 129.9, 128.1, 127.2, 136.3, 129.8, 128.1, 127.2, 59.7, 58.3, 38.8, 37.7, 30.4, 27.8; ^{207}Pb NMR δ : -1541 ± 5 ppm. IR data (cm^{-1}): 3500 mb, 2900 mb, 1626 m, 1566 m, 1506 m, 1243 w, 1135 w, 1073 vw, 1046 w, 964 w, 910 w, 868 w, 761 w, 745 w, 698 m, 555 m, 519 m, 486 m, 332 m Raman data (cm^{-1}): 3061 m, 2932 w, 1606 w, 1003 m, 119 wb. Solution ^{13}C NMR δ_{DSS} (ppm; D_2O ; pD = 5.0; 0.125 M Phe): 177.0, 137.7, 132.0, 131.8, 130.4, 59.1, 38.9; ^{207}Pb NMR (D_2O ; pD = 4.7; 0.125 M Pb) δ : -2536 ppm.

Isolation of $\text{Pb(Phe)}_2(\text{H}_2\text{O})(\text{NO}_3)_2 \cdot 2\text{H}_2\text{O}$: A stirred solution (10 minutes) of L-phenylalanine (5.01 mmol, 0.828 g) in distilled water (10 mL) was added to a solution of $\text{Pb}(\text{NO}_3)_2$ (5.00 mmol, 1.657 g) in 30 mL of distilled water (stirred 10 minutes) resulting in a clear, colourless solution. The mixture was heated at 95-100 °C for 20 minutes and the solution remained clear and colourless. The hot solution was slowly cooled to room

temperature in the filtration flask and colourless needle-like crystals of $\text{Pb}(\text{L-phenylalanine})_2(\text{OH}_2)(\text{NO}_3)_2 \cdot 2\text{H}_2\text{O}$ formed from the filtrate in 11 days at room temperature; yield: 1.487 g; 41.6 %; m.p. 98-102 °C. Solid ^{13}C NMR δ (ppm): 235.9, 229.2, 227.5, 226.7, 176.3, 175.3, 136.4, 129.9, 128.3, 127.3, 136.4, 129.9, 128.3, 127.3, 59.9, 58.5, 38.9, 37.8, 30.5; ^{207}Pb NMR δ : -1541 ± 6 ppm. IR data (cm^{-1}): 3462 mb, 3022 sb, 1627 m, 1565 m, 1511 m, 1316 mb, 1244 w, 1199 w, 1147 w, 1135 m, 1073 w, 1046 w, 761 m, 698 m, 556 m, 519 m, 486 m, 332 mb. Raman data (cm^{-1}): 3060 mb, 1605 w, 1002 m, 122 wb. Solution ^{13}C NMR δ_{DSS} (ppm; D_2O ; pD = 4.9; 0.125 M Phe): 177.2, 137.8, 132.1, 131.9, 130.5 59.3, 39.0; ^{207}Pb NMR δ (D_2O ; pD = 4.7; 0.125 M Pb): -2610 ppm.

Isolation of $\text{Pb}_2(\text{HArg})_3(\text{H}_2\text{O})(\text{NO}_3)_7 \cdot 3\text{H}_2\text{O}$: A stirred solution (10 minutes) of L-arginine (5.03 mmol, 0.877 g) in 10 mL of distilled water (pH 11.43) was added to a solution of $\text{Pb}(\text{NO}_3)_2$ (5.00 mmol, 1.656 g) in 30 mL of distilled water (stirred 10 minutes) resulting in a cloudy white mixture with a pH of 6.31. This mixture was acidified with concentrated HNO_3 , with stirring, to pH 3.10 resulting in a clear, colourless solution. This solution was heated at 95-100 °C for 60 minutes and was subsequently slowly cooled to room temperature in the filtration flask. Colourless needle-like crystals of $\text{Pb}_2(\text{L-arginine})_3(\text{H}_2\text{O})(\text{NO}_3)_7 \cdot 3\text{H}_2\text{O}$ formed from the filtrate in 20 days at room temperature; yield: 0.687 g; 28.3 %; m.p. 92-95 °C. Solid ^{13}C NMR δ (ppm): 177.7, 176.6, 157.5, 59.4, 57.6, 56.8, 43.5, 42.7, 40.4, 31.4, 28.4, 24.8, 24.4, 23.3; ^{207}Pb NMR δ (ppm): -1285 ± 5 , -2511 ± 5 . IR data (cm^{-1}): 3189 mb, 1762 w, 1694 w, 1587 mb, 1538 w, 863 w, 825 m, 564 w, 441 w, 333 wb. Raman data (cm^{-1}): 2934 w, 122 w. Solution ^{13}C NMR δ_{DSS} (ppm; D_2O ; pD = 4.9; 0.125 M HArg): 177.5, 159.5, 57.5, 43.2, 30.2, 26.6; ^{207}Pb NMR (D_2O ; pD = 4.7; 0.125 M Pb) δ : -2675 ppm.

When the filtrate evaporated too rapidly a slightly yellow, viscous liquid formed. This liquid was redissolved in 5 mL of distilled water, transferred to a 4 dram vial with a loosely sealed cap and left to slowly evaporate, yielding crystals within 10 days.

Isolation of $[\text{Hg}_{12}(\text{Ala})_8(\text{NO}_3)_8]\cdot 2\text{H}_2\text{O}$: A stirred solution (10 minutes) of L-alanine (5.04×10^{-3} mol) in 10 mL of distilled water (pH 6.4) was added to a suspension of $\text{Hg}_2(\text{NO}_3)_2\cdot 2\text{H}_2\text{O}$ (2.51×10^{-3} mol) in 30 mL of distilled water (stirred 10 minutes) resulting in a white cloudy suspension with a pH of 1.8. The mixture was heated at 90°C for 20 minutes and the solution became clear and colourless with the precipitation of elemental mercury. The hot solution was suction filtered and slowly cooled to room temperature in the filtration flask. Yellow needle-like crystals of $[\text{Hg}_{12}(\text{L-alanine})_8(\text{NO}_3)_8]\cdot 2\text{H}_2\text{O}$ formed from the filtrate in 30 days at room temperature; yield: 0.201 g; 17.6 %; m.p. 150°C ; d.p. 160°C . Elemental analysis for $\text{C}_{24}\text{H}_{52}\text{Hg}_{12}\text{N}_{16}\text{O}_{42}$, $3643.90 \text{ g mol}^{-1}$: experimental (calculated) %C 8.83 (7.89), %H 1.70 (1.66), %N 6.62 (6.14). IR and Raman data are listed in Table A.1. Solution ^1H NMR (ppm; D_2O ; pD = 3.5; $<0.0026 \text{ M}$) δ_{DSS} : 4.33 (*broad*), 4.12 (*broad*), 3.98 (*broad*), 1.52 (*broad doublet*); ^{13}C NMR δ_{DSS} : 180.8, 177.2, 56.4, 55.1, 20.6, 18.1. This procedure was also altered to decrease the crystallization time. The hot filtered solution was evaporated at boiling point to approximately half of the original volume and then left open to air to cool slowly. Crystals formed after 13 days at room temperature, yield 30.2 %.

The procedure above was applied using D-alanine (5.04×10^{-3} mol) in 10 mL of distilled water (pH 6.4) and $\text{Hg}_2(\text{NO}_3)_2\cdot 2\text{H}_2\text{O}$ (2.51×10^{-3} mol) in distilled water (30.0 mL; pH 2.2, white cloudy suspension) and yielded yellow needle-like crystals of $[\text{Hg}_{12}(\text{D-alanine})_8(\text{NO}_3)_8]\cdot 2\text{H}_2\text{O}$ after three weeks of slow evaporation at room temperature; yield: 18.4 %; m.p. 152°C , d.p. 162°C . IR and Raman data are listed in Table A.1. Solution ^1H NMR (ppm; D_2O ; pD = 3.8; $<0.0026 \text{ M}$) δ_{DSS} : 4.33 (*broad*), 4.12 (*broad*), 3.98 (*broad*), 1.52 (*broad doublet*); ^{13}C NMR δ_{DSS} : 180.3, 175.9, 56.4, 55.1, 20.1, 17.6. Attempts to isolate solids from reaction mixtures of mercurous nitrate with an equimolar mixture of L- and D-alanine gave a slightly yellow, viscous oil.

Table A.1: Infrared and Raman frequencies and peak assignments for [Hg₁₂(LAla)₈(NO₃)₈]•2H₂O (Hg-LAla), [Hg₁₂(DAla)₈(NO₃)₈]•2H₂O (Hg-DAla) and MeHg(LAla)*

Hg-LAla		Hg-DAla		MeHg(LAla) (ref. 43)		Assignment
IR (cm ⁻¹)	Raman (cm ⁻¹)	IR (cm ⁻¹)	Raman (cm ⁻¹)	IR (cm ⁻¹)	Raman (cm ⁻¹)	
3423 wb		3442 wb				OH
3172 m		3174 m		~3200 mb		NH ₂
	3086 m			3075 mb	3078 wb	NH ₂
	2993 m		2988 m	2988 m	2990 m	CH ₃
	2934 w		2937 w		2936 w	CH ₃
1569 s		1574 s		1558 vs		NH ₂
	1467 vw		1468 vw	1459 m	1462 s	CH ₃
	1410 w		1416 w	1406 s	1409 m	CO ₂ ⁻
	1343 vw			1373 w	1372 w	CH ₃
				1353 s	1352 s	CH ₃
1319 m				1304 s	1299 w	CH
~1200 – 1280 m (multiple peaks)		~1200 – 1280 m (multiple peaks)		1297 w		NH ₂
				1253 w		
				1224 wb		
1106 m	1113 vw	1106 m		1115 m	1114 m	C-N
1023 m	1038 vs		1038 vs	1032 w	1031 m	CH ₃
	940 vw			932 w	932 w	C-CO ₂ ⁻
858 w	860 m	859 m	860 m	852 m	850 m	C-CH ₃
818 w		820 m		809 m		NH ₂
757 w		758 w		766 w		CO ₂ ⁻
645 vw				618 w	616 vw	CO ₂ ⁻
	575 m		577 m	573 w	567 vw	CO ₂ ⁻
553 m		557 m		537 s	546 vs	Hg-N
525 w		526 w				
	160 s		159 s		172 (ref. 96)	Hg-Hg

* Abbreviations: w = weak, m = medium, s = strong, b = broad, v = very.

Note: Peak assignments for the mercury-amino acid complexes are based on those proposed for methylmercury-L-alanine as well as other mercury-amino acid compounds^{43;45;95;120} and the mercury-mercury peak assignment was based upon a mercury(I) solvation study.⁹⁶

Isolation of [Hg₂(Pro)₂(NO₃)₂]: A cloudy, grey suspension of L-proline (2.49 x 10⁻³ mol, 0.287 g) and Hg₂(NO₃)₂•2H₂O (1.25 x 10⁻³ mol, 0.703 g) was prepared in distilled water (20.0 mL; pH 2.45). This suspension was heated at 90 °C for 40 minutes and the solution became clear and colourless with the precipitation of elemental mercury. The hot solution was suction filtered and slowly cooled to room temperature in the filtration flask. As the solution became more concentrated, it was transferred to a 4 dram vial with the lid loosely sealed to allow for slower evaporation. Hygroscopic, colourless, needle-like crystals of [Hg₂(L-proline)₂(NO₃)₂] formed from the filtrate in 5 months at room temperature; yield: 0.402 g; 42.7 %; m.p. 110-120 °C; d.p. 120 °C. IR data (cm⁻¹): 2352 m, 2314 w, 1715 m, 1642 s, 1610 w, 958 w, 769 s, 720 w, 666 m, 556 s, 485 w; Raman data (cm⁻¹): 3007, 2940, 543, 182. Solution ¹H NMR (D₂O; pD = 2.9; 0.125 M Pro) δ_{DSS}: 4.28 (*quartet*), 3.40 (*doublet of multiplets*), 2.26 (*doublet of multiplets*), 2.04 (*quintet*); ¹³C NMR δ_{DSS}: 176.3, 63.9, 48.7, 31.2, 26.1.

Isolation of [Hg₂(NAla)₂(NO₃)₂]•2H₂O: A cloudy, grey suspension of *N*-methyl-alanine (2.50 x 10⁻³ mol, 0.258 g) and Hg₂(NO₃)₂•2H₂O (1.25 x 10⁻³ mol, 0.699 g) was prepared in 20.0 mL of distilled water (pH 2.47). This suspension was heated at 90 °C for 40 minutes and the solution became clear and colourless with the precipitation of elemental mercury. The hot solution was suction filtered and slowly cooled to room temperature in the filtration flask. As the solution became more concentrated, it was transferred to a 4 dram vial with the lid loosely sealed to allow for slower evaporation. Colourless needle-like crystals of [Hg₂(*N*-methyl-L-alanine)₂(NO₃)₂]•2H₂O formed from the filtrate in 19 days at room temperature; yield: 0.184 g; 19.2 %; m.p. 108-110 °C. IR data (cm⁻¹): 3244 w, 2900 sb, 2492 m, 2064 w, 1756 m, 1644 vs, 1524 w, 1328 vw, 1256 vw, 1198 vw, 1099 w, 912 w, 887 m, 840 m, 822 s, 763 s, 718 w, 682 m, 662 m, 554 vs, 445 vs. Raman data (cm⁻¹): 3039 mb, 2997 m, 2954 m, 1400 wb, 845 m, 559 m, 164 m. Solution ¹H NMR (D₂O; pD = 3.2; 0.125 M *N*-methyl-L-alanine) δ_{DSS}: 3.81 (*quartet*), 2.74 (*singlet*), 1.54 (*doublet*); ¹³C NMR δ_{DSS}: 176.0, 60.7, 32.7, 16.1.

Other metal-amino acid isolation attempts and comments on the isolation method:

The metal-amino acid complex isolation method described in this work was also followed in attempted isolations of additional lead-amino acid and mercury(I)-amino acid complexes with the other protein forming L-amino acids, and also bismuth-amino acid and mercury(II)-amino acid complexes with all 20 protein forming L-amino acids. No additional lead-amino acid or mercury(I)-amino acid complexes were isolated, but the systems were not studied to a great extent.

The mercury(II)-amino acid and bismuth-amino acid solutions were found to be more acidic than the mercury(I)-amino acid or lead-amino acid solutions and the metal-amino acid complexes were not isolated from these solutions. In the case of bismuth with glycine, alanine, valine, leucine, isoleucine and phenylalanine, the protonated amino acid with a nitrate counter ion was isolated. From these observations, the appropriate pH range for the isolation of the metal-amino acid complexes from acidic solutions is estimated to be between 2 and 5. Below this range, the protonated amino acids will crystallize out of solution and above this range the metal oxides and hydroxides will precipitate out of solution. The pH range required for complex isolation is expected to differ between each system, however, and should be determined separately for each metal-amino acid combination.

Crystallizations of Pb-Val, Pb-Ile, Pb-Phe.2H₂O were performed with an initial 1:2 stoichiometric ratio of the metal to amino acid. The same crystal structures as the 1:1 stoichiometric ratio combinations were obtained, but an unidentified precipitate also formed during crystallization. The pH values of these acidic solutions (*ca.* pH 5) were higher than those of the 1:1 stoichiometric ratio solutions and this increase in pH was deemed to be the cause of the formation of precipitate.

Isolation of Hg-Lala was also attempted using a 2:1:2 mercury(I) to mercury(II) to L-alanine stoichiometric ratio. The resulting solution was found to be more acidic (*ca.* pH 1) than the Hg-Lala solution and did not yield crystals.

The use of other solvents and crystallization methods were also investigated for the isolation of lead-amino acid and mercury(I)-amino acid complexes, these included liquid-vapour diffusion and liquid-liquid diffusion with acetone, methanol or ethanol and an aqueous metal-amino acid solution. The other solvents were found to cause a precipitate to form in solution at even dilute metal-amino acid solution concentrations. No crystals were isolated from these reactions.

In some cases, crystallization of the characterized complexes was found to be dependent on the rate of solvent evaporation. If the solvent evaporated too quickly, an oil or a powder formed, instead of crystals. Factors that affected the rate of solvent evaporation and the formation of crystals included the size and shape of the crystallization vessel (use of a 125 mL filter flask versus a 50 mL Erlenmeyer flask versus a 4 dram vial), location of the vessel within the fume hood (close to the back or to the front, or surrounded by other crystallization vessels), and in the case of the mercury(I)-proline crystals the humidity within the laboratory.

Attempts to crystallize heteroleptic lead-amino acid complexes using phenylalanine with glycine, alanine, valine, leucine and isoleucine resulted in the formation of Pb-Phe.2H₂O crystals. This lead-phenylalanine complex takes less time to crystallize than do the other lead-amino acid complexes. This increased rate of crystallization, is thought to be responsible for the exclusive isolation of the homoleptic Pb-Phe.2H₂O complex.

A.4 X-RAY CRYSTALLOGRAPHY

Crystals of the metal-amino acid complexes were coated in Paratone-N oil then mounted on a thin glass fiber and cooled to 193(2) K under a cold N₂ stream. X-ray diffraction data were obtained using a Bruker PLATFORM diffractometer with a SMART 1000 CCD area detector using graphite-monochromated Mo K α radiation ($\lambda = 0.71073$ Å). Programs for diffractometer operation, unit cell indexing, data collection, data reduction and absorption correction were supplied by Bruker. The data were corrected for absorption through Gaussian integration from indexing of the crystal faces. Structures were solved using the Patterson search/structure expansion facilities within the *DIRDIF-99* program system.¹²¹ Refinements were completed using the program *SHELXL-97*.¹²² Hydrogen atoms were assigned positions based on the geometries of their attached carbon, nitrogen, or oxygen atoms, and were given thermal parameters 20% (for C-H or N-H) or 50% (for O-H) greater than those of their parent atoms. For both structures an idealized geometry was imposed on the water molecules by fixing the O-H bond distances at 1.00 Å and the intramolecular H \cdots H distances at 1.63 Å during refinement. These water hydrogen atoms were oriented towards nearby nitrate group oxygen atoms by constraining the four atoms of the O-H \cdots O-N hydrogen-bonded units to be coplanar (i.e. by setting these atoms to define a tetrahedron with a volume of no more than 0.001 Å³). See Table A.2, Table A.3 and Table A.4 for a summary of crystal parameters for each complex. The structures were prepared using Ortep 3v2 for Windows¹²³ and Adobe Illustrator CS2.

Abbreviations Used for Crystallographic Data in Table A.2, Table A.3 and Table A.4:

$[\text{Pb}(\text{OH}_2)_2(\text{L-valine})_2(\text{NO}_3)][\text{NO}_3]$	Pb-Val
$[\text{Pb}(\text{OH}_2)(\text{L-isoleucine})_2][\text{NO}_3]_2 \cdot \text{H}_2\text{O}$	Pb-Ile
$[\text{Pb}(\text{OH}_2)_2(\text{L-valine})(\text{L-isoleucine})(\text{NO}_3)_2]$	Pb-Val-Ile
$[\text{Pb}(\text{OH}_2)_2(\text{L-phenylalanine})_2(\text{NO}_3)][\text{NO}_3]$	Pb-Phe.2H ₂ O
$[\text{Pb}(\text{OH}_2)(\text{L-phenylalanine})_2][\text{NO}_3]_2 \cdot 2\text{H}_2\text{O}$	Pb-Phe.3H ₂ O
$[\text{Pb}_2(\text{OH}_2)(\text{L-arginine})_3(\text{N}_3\text{O})_7] \cdot 3\text{H}_2\text{O}$	Pb-HArg
$[\text{Hg}_{12}(\text{L-alanine})_8(\text{NO}_3)_8] \cdot 2\text{H}_2\text{O}$	Hg-LAla
$[\text{Hg}_{12}(\text{D-alanine})_8(\text{NO}_3)_8] \cdot 2\text{H}_2\text{O}$	Hg-DAla
$[\text{Hg}_2(\text{L-proline})_2(\text{NO}_3)_2]$	Hg-Pro
$[\text{Hg}_2(\text{N-methyl-L-alanine})_2(\text{NO}_3)_2] \cdot 2\text{H}_2\text{O}$	Hg-NAla

Table A.2: Crystallographic data for lead-amino acid complexes discussed in Chapter 2

	Pb-Val	Pb-Ile	Pb-Val-Ile
Empirical Formula	C ₁₀ H ₂₆ N ₄ O ₁₂ Pb	C ₁₂ H ₃₀ N ₄ O ₁₂ Pb	C ₁₁ H ₂₈ N ₄ O ₁₂ Pb
FW	601.54	629.59	615.56
Crystal Dimensions	0.52 x 0.51 x 0.20	0.76 x 0.38 x 0.03	0.44 x 0.35 x 0.16
Crystal System	Orthorhombic	Orthorhombic	Orthorhombic
Space Group	<i>P</i> 2 ₁ 2 ₁ 2 ₁ (No. 19)	<i>P</i> 2 ₁ 2 ₁ 2 ₁ (No. 19)	<i>P</i> 2 ₁ 2 ₁ 2 ₁ (No. 19)
<i>a</i> (Å)	5.4125 (6)	5.4331 (5)	5.4526 (4)
<i>b</i> (Å)	13.6907 (14)	13.5936 (13)	13.5911 (11)
<i>c</i> (Å)	26.708 (3)	30.120 (3)	28.742 (2)
<i>V</i> (Å ³)	1979.1 (4)	2224.5 (4)	2130.0 (3)
<i>Z</i>	4	4	4
ρ_{calcd} (g cm ⁻³)	2.019	1.880	1.920
μ (mm ⁻¹)	8.590	7.647	7.984
2 θ limit(deg)	54.96	55.00	57.20
Total number of data collected	16494	19329	18904
	$-7 \leq h \leq 7$	$-7 \leq h \leq 7$	$-7 \leq h \leq 7$
	$-17 \leq k \leq 17$	$-17 \leq k \leq 17$	$-17 \leq k \leq 17$
	$-34 \leq l \leq 34$	$-38 \leq l \leq 38$	$-37 \leq l \leq 37$
Number of independent reflections	4510	5050	5141
<i>R</i> _{int}	0.0246	0.0364	0.0302
Number of observed reflections	4061	4802	4941
Range of transmission factors	0.2784–0.0945	0.8031–0.0680	0.3615–0.1270
Number of data/restraints/params	4510/0/244	5050/10*/272	5141/0/253
Flack absolute structure parameter	0.001 (5)	0.007 (6)	0.043(7)
<i>R</i> ₁ [<i>F</i> _o ² ≥ 2σ(<i>F</i> _o ²)]	0.0181	0.0217	0.0253
w <i>R</i> ₂ [<i>F</i> _o ² ≥ 3σ(<i>F</i> _o ²)]	0.0406	0.0513	0.0589
GOF	1.047	1.096	1.150
Additional Comments		**Refined with an SOF of 0.5	

*Distances involving the hydrogen atoms of the water molecules were given fixed values: d(O1–H1OA) = d(O1–H1OB) = d(O2–H2OA) = d(O2–H2OB) = 0.86 Å;

d(H1OA···H1OB) = d(H2OA···H2OB) = 1.40 Å.

**Bond distances involving the disordered L-isoleucine carbon atoms were constrained to be equal (within 0.01 Å) during refinement: d(C22–C24A) = d(C22–C24B); d(C24A–C25A) = d(C24B–C25B).

Table continued on next page...

(Table A.2 continued.)

	Pb-Phe.2H ₂ O	Pb-Phe.3H ₂ O	Pb-HArg
Empirical Formula	C ₁₈ H ₂₆ N ₄ O ₁₂ Pb	C ₁₈ H ₂₈ N ₄ O ₁₃ Pb	C ₁₈ H ₅₃ N ₁₉ O ₃₁ Pb ₂
FW	697.62	715.63	1446.17
Crystal Dimensions	0.63 x 0.16 x 0.12	0.37 x 0.10 x 0.08	0.63 x 0.23 x 0.11
Crystal System	Orthorhombic	Orthorhombic	Monoclinic
Space Group	<i>P</i> 2 ₁ 2 ₁ 2 ₁ (No. 19)	<i>P</i> 2 ₁ 2 ₁ 2 ₁ (No. 19)	<i>P</i> 2 ₁ (No. 4)
<i>a</i> (Å)	5.3525 (4)	5.6093 (5)	7.4258 (7)
<i>b</i> (Å)	13.4886 (10)	13.7434 (13)	28.522 (3)
<i>c</i> (Å)	33.906 (3)	32.965 (3)	10.8529 (10)
β (deg)	—	—	100.6104 (13)
<i>V</i> (Å ³)	2447.9 (3)	2541.3 (4)	2259.4 (4)
<i>Z</i>	4	4	2
ρ_{calcd} (g cm ⁻³)	1.893	1.870	2.126
μ (mm ⁻¹)	6.960	6.709	7.561
2 θ (deg)	54.94	54.96	55.02
Total number of data collected	51445	22242	19964
	-6 ≤ <i>h</i> ≤ 6	-7 ≤ <i>h</i> ≤ 7	-9 ≤ <i>h</i> ≤ 9
	-17 ≤ <i>k</i> ≤ 17	-17 ≤ <i>k</i> ≤ 17	-37 ≤ <i>k</i> ≤ 36
	-43 ≤ <i>l</i> ≤ 44	-42 ≤ <i>l</i> ≤ 42	-14 ≤ <i>l</i> ≤ 14
Number of independent reflections	5571	5810	10295
<i>R</i> _{int}	0.0243	0.0499	0.0210
Number of observed reflections	5463	5372	9931
Range of transmission factors	0.4889–0.0967	0.6159–0.1904	0.4901–0.0872
Number of data/restraints/params	5571/0/316	5810/10*/338	10295/0/634
Flack absolute structure parameter	0.010 (7)	0.025 (13)	0.002 (3)
<i>R</i> ₁ [<i>F</i> _o ² ≥ 2σ(<i>F</i> _o ²)]	0.0254	0.0479	0.0218
w <i>R</i> ₂ [<i>F</i> _o ² ≥ 3σ(<i>F</i> _o ²)]	0.0588	0.1125	0.0470
GOF	1.140	1.289	0.968

*Distances involving two hydrogen atoms of the water molecules were given fixed values: d(O2–H2OA) = d(O2–H2OB) = d(O3–H3OA) = d(O3–H3OB) = 0.86 Å; d(H2OA···H2OB) = d(H3OA···H3OB) = 1.40 Å. Idealized hydrogen-bonded geometries for these water molecules were achieved by constraining the hydrogen atoms to lie in the same plane as the oxygen atoms to which they are bonded and hydrogen-bonded, i.e. by constraining the five-atom units ([a] O32···H2OA–O2–H2OB···O3[at 1+x, y, z]; [b] O21···H3OA–O3–H3OB···O31[at 1–x, -½+y, ½–z]) to define a polyhedron with a volume of no more than 0.05 Å³.

Table A.3: Crystallographic data for mercury-alanine complexes discussed in Chapter 3

	Hg-LAla	Hg-DAla
Empirical Formula	C ₂₄ H ₅₂ Hg ₁₂ N ₁₆ O ₄₂	C ₂₄ H ₅₂ Hg ₁₂ N ₁₆ O ₄₂
FW	3643.90	3643.90
Crystal Dimensions	0.36 x 0.22 x 0.06	0.43 x 0.09 x 0.05
Crystal System	Monoclinic	Monoclinic
Space Group	P2 ₁ (No. 4)	P2 ₁ (No. 4)
<i>a</i> (Å)	10.6210(11)	10.6255(6)
<i>b</i> (Å)	19.7259(19)	19.7285(11)
<i>c</i> (Å)	15.3150(15)	15.3184(9)
β (deg)	91.5646(14)	91.5655(8)
<i>V</i> (Å ³)	3207.4(6)	3209.9(3)
<i>Z</i>	2	2
ρ_{calcd} (g cm ⁻³)	3.773	3.770
μ (mm ⁻¹)	28.708	28.685
2θ (deg)	52.80	54.54
Total number of data collected	22560	28120
	-13 ≤ <i>h</i> ≤ 13	-13 ≤ <i>h</i> ≤ 13
	-24 ≤ <i>k</i> ≤ 24	-25 ≤ <i>k</i> ≤ 25
	-19 ≤ <i>l</i> ≤ 19	-19 ≤ <i>l</i> ≤ 19
Number of independent reflections	12859	14518
<i>R</i> _{int}	0.0367	0.0308
Number of observed reflections	11021	13213
Range of transmission factors	0.2777–0.0344	0.3281–0.0285
Number of data/restraints/params	12859/11/859	14518/11/859
Flack absolute structure parameter	-0.015(11)	-0.005(7)
<i>R</i> ₁ [<i>F</i> _o ² ≥ 2σ(<i>F</i> _o ²)]	0.0481	0.0280
w <i>R</i> ₂ [<i>F</i> _o ² ≥ 3σ(<i>F</i> _o ²)]	0.0844	0.0569
GOF	1.043	1.001

Table A.4: Crystallographic data for mercury-secondary amino acid complexes discussed in Chapter 4

	Hg-Pro	Hg-NAla
Empirical Formula	C ₁₀ H ₁₈ Hg ₂ N ₄ O ₁₀	C ₈ H ₂₂ Hg ₂ N ₄ O ₁₂
FW	755.46	767.48
Crystal Dimensions	0.53 x 0.35 x 0.17	0.32 x 0.27 x 0.17
Crystal System	Monoclinic	Monoclinic
Space Group	P2 ₁ (No. 4)	P2 ₁ (No. 4)
<i>a</i> (Å)	6.1494 (8)	6.0212 (6)
<i>b</i> (Å)	8.5210 (11)	11.5082 (12)
<i>c</i> (Å)	16.879 (2)	13.8511 (14)
β (deg)	95.710 (2)	90.5833 (12)
<i>V</i> (Å ³)	880.0 (2)	959.74 (17)
<i>Z</i>	2	2
ρ_{calcd} (g cm ⁻³)	2.851	2.656
μ (mm ⁻¹)	17.48	16.04
2θ (deg)	54.84	55.00
Total number of data collected	7601	5216
	$-7 \leq h \leq 7$	$-6 \leq h \leq 7$
	$-10 \leq k \leq 11$	$-14 \leq k \leq 14$
	$-21 \leq l \leq 21$	$-15 \leq l \leq 17$
Number of independent reflections	3954	4143
R_{int}	0.0247	0.0533
Number of observed reflections	3875	3868
Range of transmission factors	0.1550–0.0389	0.1713–0.0794
Number of data/restraints/params	3954/3*/ 248	4143/0/235
Flack absolute structure parameter	0.007 (8)	0.019 (15)
R_1 [$F_o^2 \geq 2\sigma(F_o^2)$]	0.0184	0.0413
wR_2 [$F_o^2 \geq 3\sigma(F_o^2)$]	0.0437	0.0964
GOF	0.975	0.977
Additional Comments	*Refined with an SOF of 0.50	

*The following pairs of atoms of the disordered proline ligand were restrained to have the same interatomic distances: N2–C10A and N2–C10B; C8–C9A and C8–C9B; C9A–C10A and C9B–C10B.

A.5 VIBRATIONAL SPECTROSCOPY

Samples for IR spectroscopy were prepared as Nujol mulls between CsI disks. Samples for Raman spectroscopy were ground into fine powders and packed into glass capillary tubes. Raman and IR data were collected on a Bruker RFS 100 FT-Raman Spectrometer (Nd:YAG laser, emission wavelength 1.06 μm , output power 80 mW), and a Bruker Vector 22 spectrometer (He:Ne laser, emission wavelength 633 nm, output power 1 mW) or a PerkinElmer precisely Spectrum 100 FT-IR spectrometer (source type: MIR; detector type: LiTaO₃), respectively.

A.6 SOLID STATE NMR SPECTROSCOPY

Samples for solid state ¹³C and ²⁰⁷Pb NMR spectroscopy were ground into a fine powder and packed into a 4 mm rotor. There was enough material to fill the rotor completely. All experiments were carried out on a Bruker Avance NMR spectrometer with a 9.4 T magnet (400 MHz proton Larmor frequency, 100.65 MHz ¹³C Larmor frequency, 83.6MHz ²⁰⁷Pb Larmor frequency) using a double resonance probe head for mercury containing samples and a triple resonance HXY probe head for lead containing samples for rotors of 4 mm diameter.

A.6.1 Carbon-13 ssNMR Analyses

Sample were spun at 8.0 kHz and 10.0 kHz to determine centre bands and to identify spinning sidebands. Relaxation times for the protons were determined by inversion recovery sequences. From these experiments a recycle delay of 10.00 s was determined and was employed for the ¹³C cross-polarization (CP)/magic angle spinning (MAS). The other parameters for the ¹³C CP/MAS experiments with two-pulse phase modulation (TPPM) proton decoupling were optimized on glycine, whose carbonyl resonance also served as external, secondary chemical shift standard at 175.06 ppm. For the ¹³C CP/MAS NMR spectra 16 scans were accumulated, using 2.6 ms CP contact times.

A.6.2 Lead-207 ssNMR Analyses

The sample was spun at various spinning speeds between 10 and 13 kHz to determine centre bands and to identify spinning sidebands. Relaxation times were not determined. Repetition times between 1 and 12 seconds were used. Between 2000 and 9000 transients were accumulated. In order to characterize the isotropic chemical shifts, it was necessary to vary the centre excitation frequencies to fully excite all spinning sidebands. Chemical shift referencing was done with solid $\text{Pb}(\text{NO}_3)_2$. Its temperature dependence has been well characterized.⁹⁸ Because of spinning induced sample heating, which is not known to sufficient precision, a static powder sample was used with the temperature read from a temperature sensor.

The obtained line shape was fitted using the `xedplot`,¹²⁴ the value of the isotropic shift given by Beckman *et al.*,⁹⁸ and the chemical shift was referenced. The value was consistent with that determined from $\text{Pb}(\text{NO}_3)_2$ spinning at 5 and 10 kHz, including spinning induced temperatures following the procedure described by Grimmer *et al.*¹²⁵ An uncertainty in the shift of 2 ppm was added to the results. No change in reference frequency was observed over the experimental time.

All NMR experiments for the Pb-Val-Ile crystals were carried out on a Bruker Avance NMR spectrometer with a 9.4 T magnet (400 MHz proton Larmor frequency, 83.6 MHz ²⁰⁷Pb Larmor frequency) using a triple resonance HXY probe head for rotors of 4 mm diameter. The sample was spun at various spinning speeds between 10 and 13 kHz to determine centre bands and to identify spinning sidebands. Relaxation times were not determined. Repetition times of 1 second were used. Between 40000 and 64000 transients were accumulated. Spectra were acquired with both Single Pulse Excitation (SPE) (with a pulse length of 90 degrees on resonance) and Hahn echoes. The Hahn echo pulse delay was chosen to be 20 μs . This turned out to be sufficient for whole echo acquisition. Consequently, the spectra can be shown in magnitude mode. The SPE spectra are also shown in magnitude mode, since no reliable phasing could be determined due to the broad spinning sidebands and the heavy baseline distortion due to pulse length and pulse breakthrough. The spectra were left-shifted up to 36 μs and linearly back-projected.

Chemical shift referencing was done with solid $\text{Pb}(\text{NO}_3)_2$ spinning at 5 and 10 kHz following the earlier procedure described. A 2 ppm uncertainty in the shift was added to the results.

A.7 pH MEASUREMENTS AND PROBE CALIBRATION FOR pD

pH and pD measurements for reaction mixtures were performed using a ROSS Sure-Flow combination pH electrode with a ThermoOrion model 230 pH meter. pD measurements for the smaller dissolved crystal samples were performed using ISFET Sensor Probe T2-387 PH 47-SS, I.Q. Scientific Instruments. For the pD measurements, the ROSS Sure-Flow electrode was soaked overnight in a 0.67 M KCl in deuterium oxide solution, while the ISFET Sensor Probe was initially soaked for 30 minutes in D_2O (to hydrate the probe) and then soaked for an additional 20 minutes in the 0.67 M KCl in deuterium oxide solution.

Calibrations of the ROSS Sure-Flow probe were performed twice, as probe maintenance and cleaning was required between the two calibrations. The first calibration applies to the procedures A.8.3 and A.8.5, while the second calibration applies to all other pD analyses.

Calibration #1 ROSS Sure-Flow probe: The probe was calibrated with six solutions of DCl in D_2O with concentrations of 9.99×10^{-2} M, 9.99×10^{-3} M, 7.94×10^{-3} M, 1.00×10^{-3} M, 3.16×10^{-5} M, and 8.0×10^{-7} M, and the electrode potential was measured in mV. The pD of each sample solution was calculated from the experimentally determined calibration curve: **Electrode Potential = -58.92 pD + 327.56; $R^2 = 0.9989$.**

Calibration #2 ROSS Sure-Flow probe: The probe was calibrated with five concentrations of DCl in D_2O (in triplicate) with concentrations of 9.99×10^{-2} M, 7.94×10^{-3} M, 2.48×10^{-3} M, 3.16×10^{-4} M, and 9.92×10^{-6} M, and the electrode potential was measured in mV. The pD of each sample solution was calculated from the experimentally determined calibration curve:

Electrode Potential = -59.71 pD + 456.72; $R^2 = 0.997$.

pD measurement using the ISFET Sensor Probe: A curve of pD vs electrode potential (in mV) was experimentally determined using three concentrations of DCl in D₂O (in triplicate) with concentrations of 9.99×10^{-2} M, 7.94×10^{-3} M, 2.48×10^{-3} M, and amino acid or metal-amino acid reaction mixtures in D₂O with the pDs measured using Calibration #2. These pD values are reported to one decimal place and are deemed to be estimates of the actual solution pD value.

Electrode Potential = -57.49 pD + 398.67; R² = 0.988.

A.8 SOLUTION STATE NMR SPECTROSCOPY

A.8.1 Room Temperature Solutions

All lead-amino acid NMR reaction mixtures were prepared at room temperature, in deuterium oxide, and under nitrogen gas. These solutions were prepared in 5.00 mL volumes at 0.125 M amino acid or lead(II) concentrations and were stirred until the solutions became clear (*ca.* 5 to 10 minutes). pD measurements were taken after the solutions cleared. DSS was added to a 1.00 mL aliquot of each sample to give a concentration of 1.0×10^{-2} M DSS.

All dissolved crystal NMR solutions were prepared at room temperature by dissolving (with stirring) crystals in 1.00 mL volumes of D₂O at 0.125 M concentrations of the amino acid or the lead(II). And the pD measurements were performed after the crystal dissolved. DSS was added to each solution to give a concentration of 1.0×10^{-2} M DSS.

A mercury(II) with L-alanine NMR solution was prepared in 5.00 mL of deuterium oxide to a concentration of 0.125 M of mercury(II) and of L-alanine. The solids were dissolved (with mixing) in D₂O and the pD was measured. Solution pD was adjusted to 2.31 using NaOD and DNO₃. DSS was dissolved in a 1.00 mL aliquot of this solution to a concentration of 1.0×10^{-2} M DSS.

A.8.2 Heated Solutions

The mercury(I)-amino acid deuterium oxide solutions required heating in a water bath in order to give a clear, colourless appearance and produce a metallic mercury precipitate. The same procedure described in Section A.3 for isolating Hg-Ala, Hg-Pro and Hg-NAla was followed in the preparation of corresponding NMR solutions; however, in these cases, 5.00 mL volumes were prepared at 0.125 M concentrations of 1:1 mercury(I) to amino acid ratios. The NMR solutions were heated under a flow of nitrogen gas at 95 °C in a water bath for *ca.* 30 minutes. pD measurements were taken after the solution was heated and had cooled for *ca.* 5 minutes.

A.8.3 Chemical Shift and pD Study for Lead-Valine, L-Valine, and Lead Nitrate Solutions

Room temperature deuterium oxide solutions of L-valine, lead nitrate, and 1:1 lead nitrate to L-valine were prepared in 5.00 mL volumes at 0.125 M concentrations of lead or L-valine, with DSS added to a concentration of 1.0×10^{-2} M. The pD of each solution was varied six times, between pD values of 1 and 6, using DNO₃ and NaOD. Hydrogen-1, carbon-13 and lead-207 NMR analysis was performed on each solution at each pD value. To determine the effect of DSS on the solution chemical shifts, additional L-valine and lead nitrate with L-valine solutions were prepared without DSS.

A.8.4 Lead-207 Chemical Shift and Lead to Amino Acid Ratio Study for Lead-Valine and Lead Nitrate Solutions

Aqueous lead(II) nitrate with L-valine solutions (10.0 mL, 0.125 M Pb) with varying lead to valine ratios (Pb:Val = 1:0, 1:0.5, 1:1, 1:1.5, 1:2, 1:3, 1:4, 1:5, and 1:6 ratio, the latter of which was saturated with valine) were prepared at room temperature. The pH of these solutions were adjusted near to that of the 1:1 lead to valine ratio (pH 4.35) using HNO₃ or NaOH.

A.8.5 Chemical Shift and Ionic Strength Study for Lead-Valine, L-Valine, and Lead Nitrate Solutions

Five room temperature deuterium oxide solutions of L-valine, of lead nitrate, and of 1:1 lead nitrate with L-valine were prepared (4.00 mL, 0.125 M Pb or Val) with DSS added to a concentration of 1.0×10^{-2} M. For each solution type, sodium nitrate was added to four of the solutions to give five different ionic strengths between 0.38 and 0.88. The pD of each solution was adjusted with DNO₃ and NaOD.

A.9 ELECTROSPRAY IONIZATION MASS SPECTROSCOPY

The hot filtrates described in Section A.3 were prepared for electrospray ionization mass spectrometric (ESI-MS) analysis by diluting aliquots in distilled water or in 50/50 (v/v) methanol/distilled water (final concentration 1.25×10^{-2} M) and centrifuging at 10^4 rpm for 2 minutes immediately prior to analysis. Positive and negative ion ESI-MS spectra were obtained using a Finnigan LCQTMDUO ion trap mass spectrometer. Two separate flow solvents were used, distilled water and 50/50 (v/v) methanol/distilled water.

Instrument parameters were set at: 1.2 mL/h for the flow solvent rate, 4.00 kV for the spray voltage, 200 °C for the capillary temperature, and the in-source fragmentation option was not activated. The relative abundance of each peak for each sample type was reproducible within the ranges high (H 75 % to 100 %), medium (M 35 % to 75 %), low (L 5 % to 35 %), or very low (V <5 %). To verify the ion identity for each spectral peak, the experimentally observed isotope peak patterns were compared to calculated isotope patterns using Isotope Pattern Calculator v 4.0.¹²⁶ In addition, tandem mass spectrometric analysis of the more abundant ions from each solution was also performed. All spectra were analysed and processed using: Qual Browser,¹²⁷ Microsoft®,¹²⁸ and Sigma Plot.¹²⁹

REFERENCE LIST

- (1) Fellenberg, G. *The Chemistry of Pollution*; John Wiley & Sons, Inc.: New York, 2000.
- (2) Berlin, M.; Zalups, R. L.; Fowler, B. A. *Mercury in Handbook on the Toxicology of Metals*; Nordberg, G. F., Fowler, B. A., Nordberg, M., Friberg, L., eds. Elsevier Inc.: Burlington, 2007; pp 675-729.
- (3) Skerfving, S.; Bergdahl, I. A. *Lead in Handbook on the Toxicology of Metals*; Nordberg, G. F., Fowler, B. A., Nordberg, M., Friberg, L., eds. Elsevier, Inc.: Burlington, 2007; pp 599-643.
- (4) Alloway, B. J.; Ayers, D. C. *Chemical Principles of Environmental Pollution*; Blackie Academic & Professional: Glasgow, 1993.
- (5) Girard, J. E. *Inorganic Metals in the Environment in Principles of Environmental Chemistry*; Jones and Bartlett Publishers, Inc.: Sudbury, 2005; pp 412-439.
- (6) Lippman, M.; Cohen, B. S.; Schlesinger, R. B. *Environmental Health Science: recognition, evaluation, and control of chemical and physical health hazards*; Oxford University Press, Ltd: New York, 2003.
- (7) Timbrell, H. *Introduction to Toxicology*; CRC Press: Boca Raton, 2002.
- (8) Drasch, G. A. *Mercury in Handbook on Metals in Clinical and Analytical Chemistry*; Seiler, H. G., Sigel, A., Sigel, H., eds. Marcel Dekker, Inc.: New York, 1994.
- (9) International Programme on Chemical Safety (IPCS) *Environmental Health Criteria 101: Methylmercury*; World Health Organization: Geneva, 1990.
- (10) International Programme on Chemical Safety (IPCS) *Environmental Health Criteria 118: Inorganic Mercury*; World Health Organization: Geneva, 1991.
- (11) Godwin, H. A. *Curr. Opin. Chem. Biol.* **2001**, 5, 223-227.
- (12) Payne, J. C.; ter Horst, M. A.; Godwin, H. A. *J. Am. Chem. Soc.* **1999**, 121, 6850-6851.
- (13) Philip, A. T.; Gerson, B. *Strat. Clin. Lab. Man.* **1994**, 14, 651-670.
- (14) Christensen, J. M.; Kristiansen, J. *Lead in Handbook on Metals in Clinical and Analytical Chemistry*; Seiler, H. G., Sigel, A., Sigel, H., eds. Marcel Dekker, Inc.: New York, 1994; pp 425-440.

- (15) Andersen, O. *Chem. Rev.* **2009**, *99*, 2683-2710.
- (16) Nelson, D. L.; Cox, M. M. *Lehninger Principles of Biochemistry*; Worth Publishers: New York, 2000.
- (17) Skoog, D. A.; West, D. M.; Holler, F. J. *Fundamentals of Analytical Chemistry*; Saunders College Publishing: 1996.
- (18) Stellwagen, E.; Prantner, J. D.; Stellwagen, N. C. *Anal. Biochem.* **2008**, *373*, 407-409.
- (19) Thayer, J. S. *J. Chem. Educ.* **2005**, *82(11)*, 1721-1727.
- (20) Porterfield, W. W. *Inorganic Chemistry: a unified approach*; Addison-Wesley Publishing Company, Inc.: Don Mills, 1984.
- (21) Emsley, J. *The Elements*; Oxford University Press, Inc.: New York, 1998.
- (22) *Hard and Soft Acids and Bases*; Dowden Hutchinson & Ross, Inc.: Stroudsburg, 1973.
- (23) Miessler, G. L.; Tarr, D. A. *Inorganic Chemistry*; Pearson Education, Inc.: Upper Saddle River, 2004; pp 183-187.
- (24) Cotton, F. A.; Wilkinson, G.; Murillo, C. A.; Bochmann, M. *Advanced Inorganic Chemistry*; Wiley Interscience: New York, 1999.
- (25) Shimoni-Livny, L.; Glusker, J. P.; Bock, C. W. *Inorg. Chem.* **1998**, *37*, 1853-1867.
- (26) Claudio, E. S.; Magyar, J. S.; Godwin, H. A. *Prog. Inorg. Chem.* **2003**, *51*, 1-144.
- (27) Housecroft, C. E.; Sharpe, A. G. *Inorganic Chemistry*; Pearson Education Ltd.: Upper Saddle River, 2001.
- (28) Payne, D. J.; Egdell, R. G.; Walsh, A.; Watson, G. W.; Guo, J.; Glans, P. A.; Learmonth, T.; Smith, K. E. *Phys. Rev. Lett.* **2006**, *96*, 157403(-1)-157403(-4).
- (29) Bondi, A. *J. Phys. Chem.* **1964**, *68*, 441-451.
- (30) Gasque, L.; Bernes, S.; Ferrari, R.; de Barbarin, C. R.; de Jesus Gutierrez, M.; Mendoza-Diaz, G. *Polyhedron* **2000**, *19*, 649-653.
- (31) Burford, N.; Eelman, M. D.; LeBlanc, W. G.; Cameron, T. S.; Robertson, K. N. *Chem. Commun.* **2004**, 332-333.
- (32) Marandi, F.; Shahbakhsh, N. Z. *Anorg. Allg. Chem.* **2007**, *633*, 1137-1139.

- (33) Marandi, F.; Shahbakhsh, N. *J. Coord. Chem.* **2007**, *60*, 2589-2595.
- (34) Freeman, H. C.; Stevens, G. N.; Taylor, I. F. *J. Chem. Soc. Chem. Commun.* **1974**, 366-367.
- (35) Ye., Q.; Li, Y.-H.; Wu, Q.; Song, Y.-M.; Wang, J.-X.; Zhao, H.; Xiong, R.-G.; Xue, Z. *Chem. Eur. J.* **2005**, *11*, 988-994.
- (36) Pervukhina, N. V.; Romanenko, G. V.; Vorisov, S. V.; Magarill, S. A.; Palchik, N. A. *J. Struct. Chem.* **1999**, *40*, 461-476.
- (37) Prior, T. J. *Acta Cryst.* **2005**, *E61*, m1523-m1524.
- (38) Sikirica, M.; Grdenic, D. *Acta Cryst.* **1974**, *B30*, 144-146.
- (39) Mak, T. C. W.; Yip, W. H.; Kennard, C. H. L.; Smith, G.; O'Reilly, E. J. *Aust. J. Chem.* **1988**, *41*, 683-691.
- (40) Lindh, B. *Acta Chem. Scand.* **1967**, *21(10)*, 2743-2752.
- (41) Meyer, G.; Nockemann, P. *Z. Anorg. Allg. Chem.* **2003**, *629*, 1447-1461.
- (42) Corbeil, M. C.; Beauchamp, A. L. *Can. J. Chem.* **1986**, *64*, 1876-1884.
- (43) Corbeil, M. C.; Beauchamp, A. L. *J. Cryst. Spec. Res.* **1989**, *19(1)*, 123-134.
- (44) Saunders, C.; Burford, N.; Werner-Zwanziger, U.; McDonald, R. *Inorg. Chem.* **2008**, *47*, 3693-3699.
- (45) Taylor, N. J.; Wong, Y. S.; Chieh, P. C.; Carty, A. J. *J. Chem. Soc. Dalton Trans.* **1975**, 438-442.
- (46) Taylor, N. J.; Carty, A. J. *J. Am. Chem. Soc.* **1977**, *99(18)*, 6143-6145.
- (47) Adams, M. J.; Hodgkin, D. C.; Raeburn, U. A. *J. Chem. Soc.(A)* **1970**, 2632-2635.
- (48) Wong, Y. S.; Taylor, N. J.; Chieh, P. C.; Carty, A. J. *J. Chem. Soc. Chem. Commun.* **1974**, 625-626.
- (49) Carty, A. J.; Taylor, N. J. *J. Chem. Soc. Chem. Commun.* **1976**, 214b-216b.
- (50) Wong, Y. S.; Carty, A. J.; Chieh, P. C. *J. Chem. Soc. Dalton Trans.* **1977**, 1157-1160.
- (51) Ehsan, M. Q.; Malik, K. M. A.; Haider, S. Z. *J. Bangladesh. Acad. Sci.* **1996**, *20*, 175-181.

- (52) Corbeil, M. C.; Beauchamp, A. L. *Can. J. Chem.* **1988**, *66*, 1379-1385.
- (53) Book, L.; Carty, A. J.; Chieh, C. *Can. J. Chem.* **1981**, *59(1)*, 138-143.
- (54) Corbeil, M. C.; Beauchamp, A. L. *Can. J. Chem.* **1988**, *66*, 2458-2464.
- (55) Alcock, N. W.; Lampe, P. A.; Moore, P. J. *Chem. Soc. Chem. Commun.* **1978**, 1324-1328.
- (56) Book, L.; Carty, A. J.; Chieh, C. *Can. J. Chem.* **1981**, *59(1)*, 144-150.
- (57) Wong, Y. S.; Chieh, P. C.; Carty, A. J. *Can. J. Chem.* **1973**, *51*, 2597-2599.
- (58) Wong, Y. S.; Carty, A. J.; Chieh, P. C. *J. Chem. Soc. Dalton Trans.* **1977**, 1801-1808.
- (59) Book, L.; Mak, T. C. W. *Inorg. Chim. Acta* **1984**, *92(4)*, 265-270.
- (60) Alex, S.; Savoie, R.; Corbeil, M. C.; Beauchamp, A. L. *Can. J. Chem.* **1986**, *64*, 148-157.
- (61) Miessler, G. L.; Tarr, D. A. *Inorganic Chemistry*; Prentice-Hall, Inc.: Upper Saddle River, 2004.
- (62) Jones, J. C.; Thornback, J. R. *Medicinal Applications of Coordination Chemistry*; The Royal Society of Chemistry: Dorset, 2007.
- (63) Ebsworth, E. A. V.; Ranking, D. W. H.; Cradock, S. *Structural Methods in Inorganic Chemistry*; CRC Press: Boca Raton, 1991.
- (64) Burgess, J. *Ions in Solution: basic principles of chemical interactions*; Ellis Horwood Ltd. New York, 1988.
- (65) Pourbaix, M. *Atlas of Electrochemical Equilibria in Aqueous Solutions*; Pergamon Press: Brussels, 1966.
- (66) Nakashima, T. T.; Rabenstein, D. L. *J. Mag. Res.* **1983**, *51*, 223-232.
- (67) Henderson, W.; McIndoe, J. S. *Mass Spectrometry of Inorganic and Organometallic Compounds*; John Wiley & Sons Ltd: Chichester, 2005.
- (68) Burford, N.; Eelman, M. D.; LeBlanc, W. G. *Can. J. Chem.* **2004**, *82*, 1254-1259.
- (69) Groom, K. A. *Identification of Complexes Containing Biologically Relevant Peptides with each of the Heavy Metals As(III), Sb(III), Bi(III), Cd(II), Hg(II), Tl(I) and Pb(II) by Electrospray Ionization Mass Spectrometry*; Department of Chemistry, Dalhousie University: M.Sc. Thesis, 2005.

- (70) Ladd, M. F. C.; Palmer, R. A. *Structure Determination by X-Ray Crystallography*; Kluwer Academic/Penum Publishers: New York, 2003.
- (71) Petrov, T. G.; Treivus, E. B. *Growing Crystals from Solution*; Consultants Bureau: New York, 1969.
- (72) Woolfson, M. M. *An Introduction to X-ray Crystallography*; Cambridge University Press: Cambridge, 1997.
- (73) Coppens, P. *X-Ray Charge Densities and Chemical Bonding*; Oxford Science Publications: New York, 1997.
- (74) Lambert, J. B.; McAuliffe, C. A. *Nuclear Magnetic Resonance Spectroscopy: an introduction to the principles, applications, and experimental methods*; Pearson Education, Inc.: Toronto, 2004.
- (75) Harris, R. K.; Becker, E. D.; Cabared de Menezes, S. M.; Goodfellow, R.; Granger, P. *Pure Appl. Chem.* **2001**, *73*, 1795-1818.
- (76) Lambert, J. B.; Shurvell, H. F.; Lightner, D. A.; Cooks, R. G. Mass Spectrometry; In *Organic Structural Spectroscopy*; Prentice-Hall, Inc.: Upper Saddle River, 1998; pp 345-385.
- (77) *CRC Handbook of Chemistry and Physics*; CRC Press: Boca Raton, 2008.
- (78) Glasoe, P. K.; Long, F. A. *J. Phys. Chem.* **1960**, *64*, 188-190.
- (79) Mikkelsen, K.; Nielsen, S. O. *J. Phys. Chem.* **1960**, *64*, 632-637.
- (80) Wrackmeyer, B. *Ann. Rep. NMR Spec.* **2002**, *2002*, 1-37.
- (81) Dechter, J. J. *Prog. Inorg. Chem.* **1985**, *33*, 393-507.
- (82) Bowmaker, G. A.; Harris, R. K.; Apperley, D. C. *Inorg. Chem.* **1999**, *38*, 4956-4962.
- (83) Peringer, P. *J. Chem. Research (S)* **1980**, 194.
- (84) Jalilehvand, F.; Leung, B. O. *Inorg. Chem.* **2006**, *45*, 66-73.
- (85) Kane-Maguire, L. A. P.; Riley, P. J. *J. Coord. Chem.* **1993**, *28*, 105-120.
- (86) Sudmeier, J. L.; Berg, R. R.; Perkins, T. G. *J. Mag. Res.* **1978**, *30*, 491-496.
- (87) Gross, J. H. *Mass Spectrometry: a textbook*; Springer-Verlag: Berlin, 2004.
- (88) *Finnigan LCQDUO Hardware Manual 97033-97033 Revision B*; Technical Publications, Thermo Electron Corporation: San Jose, 2003.

- (89) Downard, K. *Mass Spectrometry: a foundation course*; The Royal Society of Chemistry: Cambridge, 2004.
- (90) Lippard, S. J.; Berg, J. M. *Principles of Bioinorganic Chemistry*; University Science Books: Mill Valley, 1994.
- (91) Magyar, J. S.; Weng, T.-C.; Stem, C. M.; Dye, D. F.; Rous, B. W.; Payne, J. C.; Bridgewater, B. M.; Mijovilovich, A.; Parkin, G.; Zaleski, J. M.; Penner-Hahn, J. E.; Godwin, H. A. *J. Am. Chem. Soc.* **2005**, *127*, 9495-9505.
- (92) Leung, B. O.; Jalilehvand, F.; Mah, V. *Dalton Trans.* **2007**, 4666-4674.
- (93) Mah, V.; Jalilehvand, F. *J. Biol. Inorg. Chem.* **2008**, *13*, 541-553.
- (94) Shindo, H.; Brown, T. L. *J. Am. Chem. Soc.* **1965**, *87*, 1904-1909.
- (95) Tan, K. H.; Taylor, M. J. *Aust. J. Chem.* **1980**, *33*(8), 1753-1761.
- (96) Rosdahl, J.; Persson, I.; Kloo, L.; Ståhl, K. *Inorg. Chim. Acta* **2004**, *357*(9), 2624-2634.
- (97) Tan, K. H.; Taylor, M. J. *Aust. J. Chem.* **1978**, *31*, 2601-2608.
- (98) Beckmann, P. A.; Dybowski, C. *J. Mag. Res.* **2000**, *146*, 379-380.
- (99) Nowotny, H.; Heger, G. *Acta. Cryst.* **1986**, *C42*, 133-135.
- (100) Aslani, A.; Morsali, A.; Zeller, M. *Dalton Trans.* **2008**, 5177.
- (101) Bharara, M. S.; Bui, T. H.; Parkin, S.; Atwood, D. A. *Dalton Trans.* **2005**, 3874-3889.
- (102) Puff, H.; Skrabs, R. *Z. Krist.* **1965**, *122*, 156-158.
- (103) Dorm, E.; Lindh, B. *Acta Chem. Scand.* **1967**, *21*(6), 1661-1662.
- (104) Batsanov, S. S. *Inorg. Materials* **2001**, *37*, 1031-1046.
- (105) Borisov, S. V.; Magarill, S. A.; Pervukhina, N. V. *J. Struct. Chem.* **2003**, *44*(6), 1018-1025.
- (106) Borisov, S. V.; Magarill, S. A.; Pervukhina, N. V. *J. Struct. Chem.* **2003**, *44*(3), 441-447.
- (107) Borisov, S. V.; Kozlova, S. G.; Gabuda, S. P. *J. Struct. Chem.* **2004**, *45*(1), 156-159.

- (108) Cutforth, B. D.; Gillespie, R. J.; Ireland, P.; Sawyer, J. F.; Ummat, P. K. *Inorg. Chem.* **1983**, 22(9), 1344-1347.
- (109) Kamenar, B.; Matkovic-Calogovic, D.; Nagl, A. *Acta Cryst.* **1986**, C42, 385-389.
- (110) Bharara, M. S.; Parkin, S.; Atwood, D. A. *Inorg. Chem.* **2006**, 45(18), 7261-7268.
- (111) Nockemann, P.; Meyer, G. Z. *Anorg. Allg. Chem.* **2003**, 629, 123-128.
- (112) Nolte, M.; Pantenburg, I.; Meyer, G. Z. *Anorg. Allg. Chem.* **2006**, 632, 113.
- (113) Henneike, H. F. *J. Am. Chem. Soc.* **1972**, 94, 5945-5950.
- (114) Meyer, G.; Nockemann, P. *Z. Anorg. Allg. Chem.* **2003**, 629, 1447-1461.
- (115) Huber, K. *The Wisconsin Mercury SourceBook*; Wisconsin Department of Natural Resources: Madison, 1997.
- (116) Zhang, L.; Wong, M. H. *Environ. Internat.* **2007**, 33, 108-121.
- (117) Chávez, T.; Garza, A.; Soto, E.; Rosario, V. *Salud Mental* **2005**, 28, 48-58.
- (118) de Marcillac, P.; Coron, N.; Dambier, G.; Leblanc, J.; Moalic, J.-P. *Nature* **2003**, 422, 876-878.
- (119) Briand, G. G.; Burford, N. *Chem. Rev.* **1999**, 99, 2601-2657.
- (120) Deacon, G. B.; Felder, E. *Aust. J. Chem.* **1967**, 20(8), 1587-1594.
- (121) Beurskens, P. T., Beurskens, G., de Gelder, R., Garcia-Granda, S., Israel, R., Gould, R. O., and Smits, J. M. M. The *DIRDIF-99* program system. Crystallography Laboratory, University of Nijmegen, The Netherlands . 1999.
- (122) Sheldrick, G. M. *SHELXL-97*. University of Göttingen, Germany . 1997.
- (123) Farrugia, L. J. *Appl. Cryst.* **1997**, 30.
- (124) Bruker. *xedplot Program*.
- (125) Gimmer, A.-R.; Kretschmer, A.; Cajipe, V. B. *Magn. Reson. Chem.* **1997**, 35, 86-90.
- (126) Yan, J. *Isotope Pattern Calculator v4.0*; Available online at <http://www.geocities.com/junhuayan/pattern.htm>; Ohio State University: Columbus, Ohio, 2001.

- (127) Finnigan Corporation. *Qual Browser v1.2*. © 1998-2000 .
- (128) Microsoft Corporation. *Microsoft® Excel 2002*. © 1985-2001 .
- (129) Systat Software, Inc. *Sigma Plot v10.0*. © 2006 .